# LIQUID CRYSTALS OF NANOPLATES − KINETICS OF PHASE TRANSITION AND CONTROL BY EXTERNAL FIELDS

A Dissertation

by

ABHIJEET BHIMRAO SHINDE

Submitted to the Office of Graduate and Professional Studies of
Texas A&M University
in partial fulfillment of the requirements for the degree of

DOCTOR OF PHILOSOPHY

| | |
|---|---|
| Chair of Committee, | Zhengdong Cheng |
| Committee Members, | Micah Green |
| | Mustafa Akbulut |
| | Philip Hemmer |
| Head of Department, | M. Nazmul Karim |

May 2019

Major Subject: Chemical Engineering

# ABSTRACT

Einstein’s seminal work on Brownian motion and Perrin’s subsequent experiments showed that colloidal particles in colloidal dispersions obey the same statistical thermodynamics as atoms. The colloid-atom analogy has paved a way to understand the physics of atomic and molecular systems. Due to their larger size than molecules and relatively slower diffusion rates, colloids show slower kinetics that enables the understanding of the physics of atomic world, for example phase transitions, on convenient length and time scales. Suspensions of non-spherical colloids such as disk shaped colloids enable the formation of novel phases, having symmetries in between that of randomly ordered liquids and perfectly ordered solid crystals, known as liquid crystals (LCs). External field induced reorientation in nematic LC phase has been exploited in electronic liquid crystal displays (LCDs), which is a multibillion dollar industry today. The topological defects in liquid crystals represent physical realizations of purely mathematical homotopy theory that also applies to cosmological phenomena and fundamental materials including superconductors, nanomagnets etc. Colloidal disks can serve as models to study liquid crystals. In this dissertation, colloidal nanoplates of zirconium phosphate having thickness of about 3 nanometers and lateral size of several hundred nanometers are used to investigate the dynamics of phase transitions in colloidal disk suspensions, phase transition kinetics and control on LC phases using electric field, temperature gradient.

Experiments to study of the kinetics of liquid crystallization are conducted using polarized optical microscopy and nucleation and growth rates of the growing nematic LC phase were measured. Due to negative anisotropy of electric polarizability, a field stabilized biaxial nematic phase that was predicted in liquid crystals of platelets and a positive evidence for the same was found. Ability to control the orientations of nanoplates on microscopic level using external electric field is useful in design of functional materials. Furthermore, external temperature gradient field was proven to be effective in moving nanoplates to the hot and their increased concentration at the hot end led to isotropic to nematic phase transition. Such thermophoretic control on the growth of nematic phase can prove to be important for technological applications.

# DEDICATION

This work is dedicated to my parents – Bhimrao Shinde and Jayashree Surwase.

# ACKNOWLEDGEMENTS

I would like to thank my advisor Dr. Zhengdong Cheng him for introducing me to the fascinating physics of soft, condensed matter and for his continuous support, thorough guidance and critical discussions on the subject matter. I thank Dr. Micah Green, Dr. Mustafa Akbulut and Dr. Philip Hemmer for giving me important suggestions on the progress of my work during committee meeting and candidacy examination. I thank Dr Akbulut for giving access to the dynamic light scattering instrument from his laboratory. I also thank Dr. Hemmer for allowing me to use some of the components for electro-optical setup such as photodiode. I would not have been able to complete my studies without the help of my coworkers especially Carlos Mejia, Xuezhen Wang, Glenn Zeng and Dali Huang. I also want to thank undergraduate students Lindsey Nolte, Sasha George and Mariela Saldivar for their assistance in conducting experiments.

I thank Dr. Tin Padetha from NASA Glenn Research Center for help in troubleshooting experiments on electric field and temperature gradient, and for providing me with a high frequency voltage amplifier. I also thank Dr. Patrick Davidson and Dr. Ivan Dozov from University of Paris and Dr. Mo Segad from Lawrence Berkley National Laboratory, for providing help with synchrotron X-ray scattering experiments. Thanks also go to my friends, the department faculty and staff for making my time at Texas A&M University a great experience.

Finally, thanks to my family for the encouragement and love.

# CONTRIBUTORS AND FUNDING SOURCES

## Contributors

This work was supervised by a dissertation committee consisting of Professor Zhengdong Cheng, Professor Micah Green and Professor Mustafa Akbulut of the Department of Chemical Engineering and Professor Philip Hemmer of the Department Electrical and Computer Engineering, Texas A&M University.

The small angle X-ray scattering data presented in Chapter 2 was obtained with the help of Professor Patrick Davidson from University of Paris. The electro-optical data discussed in Chapter 4 was obtained in collaboration with my coworker Carlos Mejia. The density profile of platelets in equilibrium nematic sediment in Chapter 6 section 3 was obtained from magneto-optical experiment performed by Chong, Ye from Guangdong University of Technology, China and X-ray attenuation data to obtain volume fraction profile in Chapter 6 section 5 was obtained with help of Dr. Rodrigo from Harvard University.

All other work conducted for the dissertation was completed by the student independently.

## Funding Sources

The research presented in this dissertation was financially supported by the National Aeronautics and Space Administration (NASA) under the grant Liquid Crystals of Nanoplates – NNX13AQ60G.

# NOMENCLATURE

| | |
|---|---|
| $l_g$ | gravitational length (Perrin length) |
| $t$ | thickness of nanoplate |
| $a$ | diameter of nanoplate |
| $D$ | diffusion constant of nanoplate |
| $\xi$ | aspect ratio |
| $k_B$ | Boltzmann constant |
| $N_B$ | biaxial nematic |
| $g$ | acceleration due to gravity |
| $m^*$ | buoyant mass of particle in a solvent |
| $\phi_I$ | volume fraction of nanoplates at I to I-N coexistent phase transition |
| $\phi_N$ | volume fraction of nanoplates at I-N coexistent to N transition |
| $\mathbf{n}$ | nematic director |
| $\varsigma$ | liquid crystal domain length |
| $\omega$ | nematic liquid crystal droplet aspect ratio |
| LC | liquid crystal |
| N | nematic |
| I | isotropic |
| S | smectic |
| $\mathbf{E}$ | electric field |
| $\mathbf{B}$ | magnetic field |

| | |
|---|---|
| T | absolute temperature |
| ZrP | zirconium phosphate |
| DLS | dynamic light scattering |
| CD | circular dichroism |
| TEM | transmission electron microscopy |
| SEM | scanning electron microscopy |
| AFM | atomic force microscopy |
| POM | polarized optical microscopy |

# TABLE OF CONTENTS

Page

ABSTRACT ........ ii

DEDICATION ........ iv

ACKNOWLEDGEMENTS ........ v

CONTRIBUTORS AND FUNDING SOURCES ........ vi

NOMENCLATURE ........ vii

TABLE OF CONTENTS ........ ix

LIST OF FIGURES ........ xii

LIST OF TABLES ........ xix

CHAPTER I INTRODUCTION ........ 1

- 1.1 Colloids ........ 1
- 1.2 Liquid crystals ........ 2
  - 1.2.1 Two main classes of liquid crystals ........ 3
    - 1.2.1A Thermotropic liquid crystals ........ 3
    - 1.2.1B Lyotropic liquid crystals ........ 3
  - 1.2.2 Structure and symmetry of different liquid crystalline phases ........ 4
  - 1.2.3 Characteristics of liquid crystals ........ 5
    - 1.2.3A Order parameter ........ 5
    - 1.2.3B Topological defects ........ 6
    - 1.2.3C Anisotropy of optical properties ........ 8
    - 1.2.3D Response to external fields ........ 9
- 1.3 Applications of disk-shaped colloids ........ 10
  - 1.3.1 Informational displays ........ 10
  - 1.3.2 Tunable structure colors ........ 11
  - 1.3.3 Platelet based LC as anisotropic media ........ 11
  - 1.3.4 Thermo-selective transport of biomolecules ........ 11
  - 1.3.5 Drug delivery ........ 12
- 1.4 Zirconium-phosphate nanoplates as model platelet colloids ........ 12
  - 1.4.1 Phase diagram of platelet suspensions ........ 13
- 1.5 Organization ........ 13

CHAPTER II PHASE DIAGRAM OF NANOPLATES ............................................... 16

2.1 Abstract ........................................................................................................ 16
2.2 Introduction .................................................................................................. 16
2.3 Synthesis of monolayer ZrP and size characterization.......................................... 18
2.4 Results and discussion...................................................................................... 22
  2.4.1 Images between crossed polarizers as a function of volume fraction ............ 22
  2.4.2 Polarized optical micrographs of suspensions................................................ 23
  2.4.3 Small angle X-ray Scattering ......................................................................... 25
  2.4.4 Circular dichroism measurements .................................................................. 27
  2.4.5 Phase diagram................................................................................................ 29
  2.4.6 Gravity induced density gradient & phase coexistence.................................. 29
  2.4.7 Extremely large nematic monodomains in cylindrical confinements ............. 31
2.5 Conclusion...................................................................................................... 33

CHAPTER III KINETICS OF NUCLEATION AND GROWTH OF NEMATIC LIQUID CRYSTALS OF NANOPLATES ................................................................. 34

3.1 Abstract ........................................................................................................ 34
3.2 Introduction .................................................................................................. 35
  3.2.1 Adaptation of classical nucleation theory to platelet colloids ........................ 37
3.3 Experimental setup.......................................................................................... 40
3.4 Sample preparation.......................................................................................... 40
3.5 Results and discussion...................................................................................... 42
  3.5.1 Measurement of nucleation and growth speeds for a single sample .............. 42
  3.5.2 Effect of nanoplate concentration on the nucleation and growth kinetics ...... 48
  3.5.3 Effect of nanoplate size on I-N separation kinetics in gravity ....................... 49
3.6 Conclusion...................................................................................................... 54

CHAPTER IV ELECTRIC FIELD CONTROL ON LIQUID CRYSTAL PHASES OF NANOPLATES.................................................................................................. 55

4.1 Abstract ........................................................................................................ 55
4.2 Introduction .................................................................................................. 56
4.3 Results and discussion...................................................................................... 57
  4.3.1 Isotropic to antinematic phase transition induced by E-field .......................... 57
  4.3.2 Uniaxial nematic to biaxial nematic phase transition induced by E-field....... 58
  4.3.3 Dynamics of defect annihilation..................................................................... 63
4.4 Conclusion...................................................................................................... 66

CHAPTER V THERMOPHORETICALLY CONTROLLED FORMATION OF NEMATIC LIQUID CRYSTALS OF NANOPLATES ................................................. 67

5.1 Abstract ........................................................................................................ 67
5.2 Introduction .................................................................................................. 68

5.3 Experimental setup of temperature gradient ........................................................71
5.4 Sample preparation..................................................................................................74
5.5 Results and discussion............................................................................................76
5.6 Conclusion................................................................................................................87

CHAPTER VI EXPERIMENTAL MEASUREMENT OF THERMODYNAMIC EQUATION OF STATE NEMATIC PHASES.............................................................88

6.1 Abstract ....................................................................................................................88
6.2 Theoretical equations of isotropic and nematic states...........................................89
6.3 Experimental measurement of the equation of state .............................................91
6.4 Proposing a simpler EOS of nematic in the low aspect ratio limit and experimental validation........................................................................................94
6.5 Measurement of EOS of isotropic phase...............................................................98
6.6 Conclusion..............................................................................................................102

CHAPTER VII CONCLUSION AND FUTURE WORK............................................103

REFERENCES.............................................................................................................106

# LIST OF FIGURES

Page

Figure 1 Schematic of isotropic and nematic phases of platelets. Isotropic phase has random orientation of platelets and nematic phase has platelets aligned along a certain direction called nematic director $\boldsymbol{n}$. ..........................................6

Figure 2 Point defects in nematic liquid crystals adapted from reference [7] with permission. The solid lines are drawn along the nematic directors $\boldsymbol{n}$ (a) radial with (m=+1) hedgehog (b) hyperbolic (m= -1) hedgehog.......................7

Figure 3. (left) picture of cut sphere (right) phase diagram of cut spheres predicted from Monte-Carlo simulations adapted from reference [36] with permission.....13

Figure 4 (a) SEM image of pristine α-ZrP. Thickness is about 0.2μm indicating few hundred ZrP monolayers held together in single disk due to Van-der-Waal forces. Figure adapted from reference [42] with permission (b) TEM image of monolayer ZrP-TBA nanoplates with chemical formula $Zr(HPO4)_x( Bu_4N^+ PO_4^-)_{2-x}$ obtained via exfoliation of pristine α-ZrP disks shown in part a. Similar contrast of different nanoplates indicated monolayers were uniform in thickness (c) AFM image of a smaller ZrP nanoplate (monolayer) (d) Profile of the height of nanoplate along the solid line in part (c) shows the thickness is ~3.8nm. ..........................................................................21

Figure 5 Snapshot of suspensions of monolayer ZrP nanoplates at different volume fractions kept between crossed polarizers captured five days after homogenization..............................................................................................23

Figure 6 POM images of ZrP suspension at different volume fractions. (a) nematic islands showing hedgehogs with m=+1 defects at isotropic-nematic phase coexistence samples at ϕ = 0.82% (b) full nematic phase showing continuous, smooth texture of nematic phase called schlieren texture at ϕ = 2.06% (c) Stripe pattern formed at ϕ = 4.8% and (d) Periodic structure with submicron scale period observed in sample in smectic phase, ϕ = 10.3% . The sample cell was 200μm thick capillary and the observations were made. 25

Figure 7 Small Angle X-ray Scattering profiles, left column (2D) and right column (1D) of monolayer ZrP suspensions at (a) 0.41% (b) 0.82% (c) 2.06% (d) 4.8% and (e) 10.3% by vol. ..................................................................27

Figure 8 Circular dichroism spectra of nanoplate suspensions at different concentrations 1.61 %, 1.81%, 1.38%, 1.61% (repeated measurement), 2.3%, 2.54% and 2.77%..........................................................................28

Figure 9 Phase diagram of ZrP nanoplates of size 1µm ± 0.15 µm................................29

Figure 10 Effect of gravity on nanoplate phases. (a) Phase coexistence based on sedimentation equilibrium model for platelets which show isotropic, nematic and columnar phases. Adapted from reference [47] reproduced with permission. (b) Extension of sedimentation equilibrium model to the system of ZrP monolayers showing I-N-S phase transition and phase coexistence depending on height of the sample tube. (c) Phase coexistence observed in a sample with $\phi_o = 0.02$ after keeping vertical for 3 years. (aspect ratio, $\xi = 0.0025 \pm 0.0004$). Sample picture taken by keeping the sample between crossed polarizers.............................................................................31

Figure 11 Crossed polar images of a nematic suspension of smaller ZrP nanoplates (avg. size = 300nm) with $\phi$~7% kept in a cylindrical vial of diameter 8mm (a) one day after homogenization (b-f) 8 months after homogenization. Polarizer (P), Analyzer (A) and slow axis of full wave plate (C) directions are as shown with the arrow. ..........................................................................33

Figure 12 Chemical potential, nucleation and growth rate of the platelet system simulated for aspect ratio 0.0134 (a) Chemical potential in dotted line corresponds to the metastable isotropic phase that is higher than that for a isotropic-nematic coexistence phase for $\phi > \phi_i = 0.0405$ and hence the system tries to form nematic phase upon going through nucleation and growth of nematic phase. (b) Normalized nucleation (black solid curve) and growth rates (red solid curve) as a function of platelet concentration higher than $\phi_i$.........................................................................................................39

Figure 13 polarized optical microscopy setup with a modification that allows imaging of a vertically kept sample................................................................................40

Figure 14 Phase diagram of aqueous suspensions of ZrP nanoplates. (a) Image of sample tubes kept between crossed polarizers obtained after 10 hours from homogenization of samples. From left to right, the initial volume fraction of nanoplates in tubes increases as 0.0315, 0.0438, 0.0496, 0.0540, 0.073, 0.0876 and 0.1022. The bright part of the tube is nematic and dark is isotropic. Width of tubes is 8mm. (b) Ratio $f_N$ of height of nematic phase to total sample height in each sample tube plotted against the total volume fraction of nanoplates. The data points are fit with logistic function represented in red color ......................................................................41

Figure 15 Polarized optical micrographs (a) initial state shear melt nuclei. A few nematic nuclei known as tactoids observed as tiny bright islands, (b) t=20 s. Subsequently, more tactoids nucleate and grew larger (c) 45 s (d) 340 s (e) 600 s. Further growth of tactoids happened via coarsening observed at (f) 19 min 32s (g) 43 m 4s (h) 1hr16min12s (i) 1hr31min25s (j) 1hr 41min 40s (k) 1hr 53min 10s and (l) 2hr 46min 55s. Scalebar: 25µm ....................................44

Figure 16 Nucleation and growth kinetics for ϕ=0.042 (a) Number of nuclei (n) increase up to 400s in the nucleation regime during which the nuclei also grow. The fit in red line shows n α t which is qualitatively in agreement with the prediction classical nucleation theory. Starting from 400s, the number of nuclei remain constant until about 3300s, after which the number of nuclei decreased due to coarsening with one another. (b) Average size of nematic nuclei (L) increases continually first via a mechanism in which the platelets from isotropic phase become part of the nematic clusters thus increasing the cluster size and later via coarsening mechanism in which two or more nuclei stay together. ..............................................................................47

Figure 17 Comparison of nucleation and growth rates from classical nucleation theory and experiments (a) nucleation speed normalized with platelet size $a$ and diffusion coefficient Ds. The rate of nucleation predicted by theory is several orders of magnitude different than experimentally measured (b) speed of growth of tactoids normalized by diffusion coefficient, effective distance required to travel to become part of nematic cluster (nuclei) from isotropic phase, σ and α is a pre-factor close to unity. Measured growth rate is two-three order of magnitude smaller than that predicted by the theory. .....49

Figure 18 Snapshots of a group 1 nanoplate suspension (**ξ** = 0.0059) between crossed polarizers with a ZrP platelet volume fraction, ϕ = 1.75%, taken as a function of time. In the beginning, the suspension was in a metastable liquid state and then underwent the nucleation and growth of tactoids, followed by tactoid sedimentation, which was completed at time, t*, when a clear interface between isotropic and nematic phases had established. This figure was adapted from reference [42] with permission...............................................51

Figure 19 . (a) Transmittance profiles along vertical line in group 1 suspension with I/Io plotted at different times. Position of I-N interface is pointed with an arrow. The transmittance profile shows a sudden jump at 341 min, indicating the establishment of I-N interface. (b) Area under the transmittance curve in (a) for the .....................................................................53

Figure 20 External field effect on phases of negative dielectric anisotropy and (a) Nanoplate normal, n, aligns perpendicular to E due to negative Δα (b) Upon application of electric field, at low volume fraction of nanoplates, $\phi$, uniaxial anti-nematic phase ($A_U$) was predicted and had been experimentally proven[67,68] whereas at high concentration, biaxial nematic phase ($N_B$) is predicted[69] but has not yet been proven experimentally. Part (b) was adapted from reference [70] with permission.........................................56

Figure 21 (a) isotropic phase (left) turns birefringent upon application of E field. (b) Schematic of nanoplate orientations in isotropic phase (top) which in presence of external e-field becomes antinematic (bottom) phase. It is coined anti because the director n is perpendicular to the field. ....................... 58

Figure 22 POM images of ϕ~4% (nematic, ξ ~0.01) sample sandwiched between ITO glass plates with separation of 120µm without E-field (a) and with E-field (100V/mm, 500kHz) after 1 min (b), 4min (c), 40min (d), 68 min (e), 218 min (f); Images (g) 45 min and (h) 18h after turning off the E-field. The scale bar indicates 200µm. E-field points in the direction out of the image plane. ........................................................................................................ 60

Figure 23 (a) A nematic phase of nanoplates at ϕ=5.5% with hedgehogs of strength +1 were found at the center of nematic domains that formed via nucleation and growth and hedgehogs of strength -1 at the boundary of the two nematic domains (b) Sketch of nanoplates in the nematic domain outlined with white dotted square in part (a) as observed from the side (XZ) plane (c) Polscope image showing retardance of the sample on a scale of 0 to 240. Isotropic part of the sample, prepared separately, appears dark. The cores of defects are about 40µm in size. (d) POM of the quasi-planar structure formed upon applying E-field in Z direction. (e)nanoplate orientation in hybrid alignment: homeotropic at the walls and planar in bulk (f)Birefringence of the sample increased due to field induced alignment and nematic phase nucleated in dark isotropic regions; the core shrank to about 10µm. Scalebar shows 200µm. ............................................................................................ 62

Figure 24 Director field mapping using Polscope imaging of the nematic phase under e-field showing m = +1 defects split into m = +½ and m=-1 defects split into two -1/2s. (a) 0 min only integer defects are observed (b)1min after application of e-field the defect cores get smaller as nanoplates were aligned with by the field and only integer defects were still observed (c) 3min after a -1/ 2 defect was seen indicating the -1 defect had started to split but +1 defects remained (d) 5min after e-field application where only ± ½ defects are observed; pairwise annihilation subsequently shown in (e) 7min and (f) 9min. ........................................................................................................ 64

Figure 25 Time exponent 0.58 is close to 0.5 indicating diffusion limited kinetics of defect annihilation in which dipoles of oppositely charged half defects are formed ........................................................................................................ 66

Figure 26 Sapphire crystal kept in touch with Peltier thermoelectric devices to create a thermal gradient across the sapphire substrate (top) and the schematic of the same (bottom) ........................................................................................ 72

Figure 27 (a) Temperature gradient across the sapphire plate (substrate) captured using FLIR Camera. The sample capillary is mounted horizontally on the substrate. (b) Linear variation of temperature of sapphire substrate with the distance from the cool end, given by T(°C)=18.34+ 0.53 x(mm) ....................74

Figure 28 (a) TEM image of ZrP nanoplates (b) Size distribution of nanoplates obtained through DLS followed by conversion of hydrodynamic diameter to the platelet diameter (c) Images of aqueous suspensions of ZrP nanoplates kept between crossed polarizers. Volume fraction of nanoplates from left to right is 0.029, 0.044, 0.048, 0.054, 0.058, 0.073 and 0.087. The nematic liquid crystal appeared bright and had settled down due to gravity after 6 hours. The cylindrical vials were 8mm in diameter. (d) Phase diagram of isotropic-nematic phase transition in ZrP nanoplates showing the ratio of nematic phase to the sum of isotropic and nematic phases plotted against the volume fraction of nanoplates. The transition from isotropic to coexisting phase happened at $\phi_{ZrP}$ = 0.035±0.002 and from coexisting to full nematic phase at $\phi_{ZrP}$ = 0.075±0.002 at which the percentages of nematic phase in the sample were 1% and 99% respectively. Green dot represents the concentration of the isotropic sample used in this study. ................................75

Figure 29 Time dependent images of a 2mm high, 26mm long capillary containing isotropic sample. (a) Temperature gradient distribution along the length of capillary as measured by the infrared thermal imaging camera. (b-g) Polarized optical images of the sample capillary. At time, t=0, (b) the suspension appeared completely dark indicating the suspension was purely isotropic. With the passage of time, as nanoplates were thermophoretically diffused to the hot region, a small amount of nematic liquid crystalline phase formed as shown in (c) 80 min. Subsequent growth of the nematic liquid crystal can be observed at (d) 120 min, (e) 200 min, (f) 400 min, (g) 800 min, and reaches steady state at (h) 1200 min and the amount of birefringent nematic remains the same as shown in (i) 1400 min. ..................78

Figure 30 (a) Demonstration of growth process of nematic liquid crystal. thermophoretic flux ($j_{th}$) of nanoplates was towards hot end in horizontal direction while gravity sedimentation ($j_g$) vertically downwards. The net flux ($j_{net}$) was dominated by thermal flux as the LC nematic nuclei were formed at the meniscus at the hot end. Local evaporation was in negligible amount. Inscribed in squares underneath are nanoplates in isotropic phase having random orientations (left) and in the nematic phase (director, n) (b) Polarized optical microscope image of thermophoretically formed nematic phase. Red lines indicated the local nematic directors. The topological structure was dominated with semi integer (±1/2) type declination (c) Polarized optical micrograph of nematic phase formed spontaneously at higher volume fraction of nanoplates ($\phi$=7%) without the temperature gradient in which the majority of topological defects were of the integer (±1) type. The elastic splay deformation of director field was higher as compared to that in the thermophoretically formed nematic phase. Scalebar: 400μm. ....................................................................................................81

Figure 31 (a) Nematic height fraction in the capillary tube with distance along temperature gradient at different time. The fitting of each nematic height profile at each time is done with two lines, with the one near the hot end becoming flat due to meniscus effect. (b) The volume of nematic phase formed as a result of thermophoresis of nanoplate colloids as a function of time. Value at each time is obtained as area under the curves in part a. ..........84

Figure 32 (a) Image of sample kept in temperature gradient at steady state ~20 hours after the beginning of the process (b) Nematic fraction, $f_N$, showed linear increase with distance along direction of increasing temperature, x. (c) Nanoplate volume fraction at steady state as a function of x. (d) Magnitude of Soret coefficient plotted against nanoplate volume fraction fit to $S_T = a/(1+B\phi)$. Lower magnitude of $S_T$ at high concentrations indicated collective effects of nanoplate interactions on thermophoresis........................86

Figure 33 Measurement of the equation of state of nematic phase and comparison with theoretical EOS and with a simplified, algebraic form of EOS for $\xi \rightarrow 0$ (a) Nanoplate volume fraction ($\phi$) as a function of normalized sample height ($z/H$). Due to sedimentation, the volume fraction of nanoplates at the bottom of the sample slowly increases with time (blue arrow) and the I-N interface height decreases (green arrow). The kinetics to reach equilibrium sedimentation profile is very slow and can take much longer to achieve. (b) Normalized osmotic pressure in the nematic phase (green curve), EOS functional fit (red curve) as proposed, and theoretically predicted EOS for hard nanoplates with aspect ratio, $\langle\xi\rangle = 0.0105$, (black curve). A good match between the measured osmotic pressure values (green curve) with the theoretical EOS (black) was observed in the low volume fraction range ($0.04 < \phi < 0.065$). The higher values of osmotic pressure for $\phi > 0.065$ indicated that sample had not yet reached the equilibrium. (c) Contribution of various terms in the polynomial of the proposed equation of state evaluated at $\phi = 0.05$............................................................................97

Figure 34 Schematic of X-ray attenuation experiment. The sample shown here is top isotropic part of I-N coexisting phase that was sitting in gravity for about six months..........................................................................................98

Figure 35 Experimentally measured osmotic pressure (red curve) is equilibrium isotropic sediment and extrapolation (black curve).......................................100

Figure 36 (a) Few data points (shown in black solid squares) from the experimental osmotic pressure in equilibrium sediment that corresponded to EOS of platelets with different aspect ratio. (b) Average size of platelets obtained from corresponding aspect ratios at different heights....................................101

Figure 37 Average size of samples carefully collected from different heights of isotropic sample sedimented for 6 months measured using dynamic light scattering.........................................................................................101

Figure 38 Topological defects in nematic phase such as disclination loop (yellow box) and point defects (red circle). In presence of temperature gradient, defects move to hot end and disclination loops vanished along its way. From left to right, the temperature of the capillary decreases linearly. ..............................105

# LIST OF TABLES

Page

Table 1 Liquid crystal phases, their symmetry and structural features, adapted from reference[6] ....... 4

Table 2 Parameters of proposed EOS, having a polynomial over polynomial form for low aspect ratio limit, fit to the experimental and theoretical data of osmotic pressures ....... 95

## CHAPTER I

## INTRODUCTION

### 1.1 Colloids

Colloids are particles of size in the range of nm to µm dispersed in another medium. Colloidal suspensions are of great importance in applications such as paints, foods, surfactants, artificial rain, rubber plating. Colloidal particles possess Brownian motion due to their thermal energy which is given by $k_B T$. From fundamental standpoint, they played a very important role in development of statistical physics. Synthetic colloidal spheres were first made in the 19402 and in the last twenty years, many reasonably characterized model colloidal systems have been developed including with different shapes that have attracted interests of chemists, chemical engineers and physicists. Colloidal suspensions have extremely high interfacial area and for colloidal particles to maintain the interface, a stabilization is needed which is either due to charges on the colloids or the polymer chains that provide steric stability. Colloids are few hundred to few hundred thousand times larger than atoms and their relaxation time, which is defined as $\tau_R = \frac{a^2}{4D}$, where $a$ is the size of colloid (diameter), D is the self-diffusion coefficient and $\tau_R$ represents the amount of time colloidal particle takes to diffuse through a length equal to its size. Value of $\tau_R$ for colloids is ~ $10^{-2}$ s as compared to atomic systems for which it is ~ $10^{-11}$ s. Thus colloids show slower kinetics that makes them models to study physics of atomic and molecular systems on much convenient time scales.

## 1.2 Liquid crystals

Liquid crystals are a class of materials which have symmetries in between that of liquids and crystalline solids. Molecules in liquid phase have random orientations and can move around because of which they show flow-ability. Whereas in crystalline solids, atoms or molecules are perfectly positioned in three-dimensional lattice structures. However, there exist many other intermediate phases called liquid crystals which have the flow ability like liquids and long range orientational or positional order that make their optical properties somewhat like crystalline solids.

In 1888, Austrian botanist Friederich Reinitzer observed a strange phenomenon while studying the melting transitions in Cholesteryl Benzoate. He observed that when solid Cholesteryl Benzoate is heated, it first melts into a cloudy liquid at 145.5 °C unlike many other compounds that melt into clear liquids. When heated further, the cloudy liquid melts into a clear liquid at 178.5 °C and this phenomenon was reversible. The strange cloudy liquid phase was later studied by German physicist Otto Lehman under a polarized microscope and he reported observation of crystallites in the cloudy liquid phase. He named the phase as Liquid Crystals. The strange phase had three intriguing properties- existence of two melting points, ability to reflect circular polarized light and ability to change the polarization state of linearly polarized light.

### *1.2.1 Two main classes of liquid crystals*

There are two main classes of liquid crystals depending on the phase transition variable is temperature or the concentration:

#### **1.2.1A Thermotropic liquid crystals**

Liquid crystals that show phase transitions from solid to liquid crystal to clear liquid purely depending on the temperature are known as thermotropic liquid crystals. Typical organic molecules such as 4-Cyano-4'-pentylbiphenyl (known as 5 CB), Cholesteryl Benzoate, 4-N-Octyl-4-CyanoBiphenyl (known as 8 CB) are thermotropic liquid crystal materials.

#### **1.2.1B Lyotropic liquid crystals**

Guest molecules or colloidal particles of non-spherical shape such as rod or disk when suspended in suitable solvent can show transition from liquid to liquid crystalline phase upon increasing the concentration of guests and are known as lyotropic liquid crystals. Unlike the thermotropic liquid crystals that are pure form of materials, these liquid crystals are two or more components due to guest-host feature. When the guests are molecules then it is known as lyotropic chromonic liquid crystal. For example, Sunset Yellow FCF (SSY) [1], Disodium cromoglycate (DSCG) molecules form lyotropic chromonic liquid crystalline (LCLC) phases.

Many colloidal systems such as Vanadium Pentoxide ($V_2O_5$) rods[2], Tobacco Mosaic Virus (TMV)[3], Gibbsite ($Al(OH)_3$) platelets[4], Zirconium Phosphate[5] have been reported to form lyotropic liquid crystals.

### *1.2.2 Structure and symmetry of different liquid crystalline phases*

**Table 1 Liquid crystal phases, their symmetry and structural features, adapted from reference[6]**

| Phase | Symmetry | Structure |
|---|---|---|
| Isotropic (I) | $K_h$ x T(3) | Liquid phase with full rotational and translational symmetry i.e. no orientational of molecules and no positional order of centers of molecules |
| Nematic (N) | $D_{\infty h}$ x T(3) | Uniaxial nematic, long range orientational order of molecules along a certain direction called the nematic director $\vec{\boldsymbol{n}}$ but no positional order of centers of molecules |
| Biaxial Nematic ($N_B$) | $D_{2h}$ x T(3) | Biaxial nematic, long range orientational order of molecules along two mutually perpendicular directions called biaxial directors $\vec{\boldsymbol{n}}$ and $\vec{\boldsymbol{m}}$ but no positional order of centers of molecules |
| Chiral Nematic (N*) Or cholesteric phase | $D_{\infty h}$ x T(3) | The direction of orientation of molecules continually rotates about an axis, called chiral nematic director $\vec{\boldsymbol{n}}$ but no positional order of centers of molecules |

**Table 1 continued**

| Phase | Symmetry | Structure |
|---|---|---|
| Smectic A (SmA) | $D_{\infty h}$ x T(2) | Centers of molecules lie only planes and the planes are equidistant from one another thus the overall fluid phase shows one dimensional positional order as within a single plane there is no order of position of centers of molecules. Orientation of molecules is perpendicular to the smectic plane. |
| Smectic C (SmC) | $C_{2h}$ x T(2) | Centers of molecules show 1D positional order same as in SmA the difference is that the orientation of molecules is at an angle (non-orthogonal) to the smectic plane. |
| Columnar | $D_{6h}$ or $D_{2h}$ x T(1) | Molecules form columns and is typically formed by discotic liquid crystals. |

*1.2.3 Characteristics of liquid crystals*

### 1.2.3A Order parameter

The most basic form of liquid crystal has long range (a few hundred molecular lengths) orientational order of molecules but no long range positional order and the phase is known as nematic phase. A quantitative measurement of the orientational order is done using order parameter (OP). For uniaxial nematic phase, the scalar order parameter (S) is a weighted average of the molecular orientation angles $\theta_m$ between the long molecular axes and the nematic director ($\vec{\boldsymbol{n}}$)

$$S = \frac{1}{2} < 3cos^2\theta_m - 1 > = \frac{1}{2} \int (3cos^2\theta_m - 1) f(\theta_m) dV \qquad (1.1)$$

where < > denotes the statistical average and $f(\theta_m)$ is the statistical distribution function of the molecular angle $\theta_m$. For platelet geometry of colloids, the molecular angle $\theta_m$ is the direction of symmetry axis which is normal to the face of platelets. More precisely, order parameter (OP) is a traceless tensor, $Q_{ij} = S\left(n_i n_j - \frac{1}{3}\delta_{ij}\right)$ where $n_i$ represents a unit vector along symmetry axis of a molecule at position *i*. Note that the orientations ***n*** and **-*n*** are equivalent.

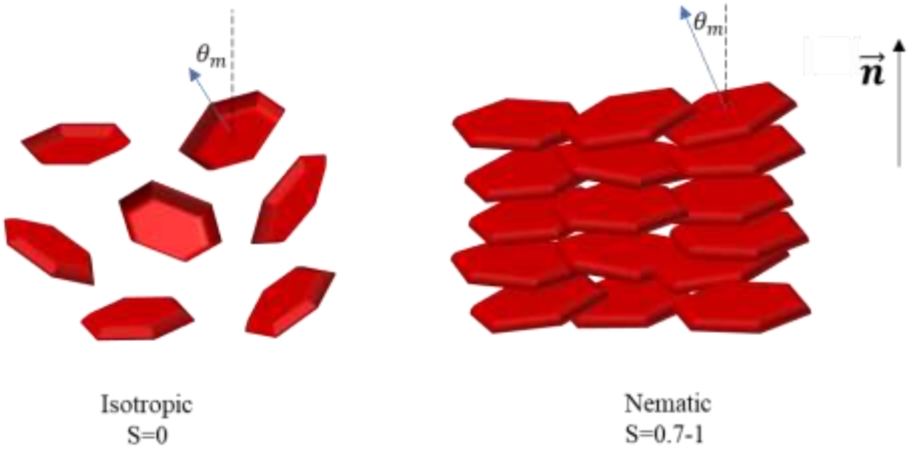

**Figure 1 Schematic of isotropic and nematic phases of platelets. Isotropic phase has random orientation of platelets and nematic phase has platelets aligned along a certain direction called nematic director $\vec{n}$.**

### 1.2.3B Topological defects

Nematic liquid crystals represent a well-defined soft matter system with a rich variety of supramolecular structures with characteristic topological defects [7]. Defects occur when there is a symmetry breaking phase transition or under an external field.

Sometimes, defects are necessary in the equilibrium state for boundary conditions imposed by bounding surface for example, in a large spherical drop of nematic LC (as will be shown later through experiments) having molecular axes (normal to the plane in case of plate-like colloids) perpendicular to the surface, a radial director field configuration leads to a point defect at the center, called a hedgehog, as shown in figure 2a. This point defect in the director configuration is completely different in nature as compared to point defects in solid crystals such as vacancy or interstitial. The topological charge (m) of the topological defect is decided parametrizing the director field in three dimensions as follows [8]

$$n(\theta, \phi) = [sin\theta \cos\left(m(\psi - \psi_0)\right), sin\theta \sin\left(m(\psi - \psi_0)\right), cos\theta]$$

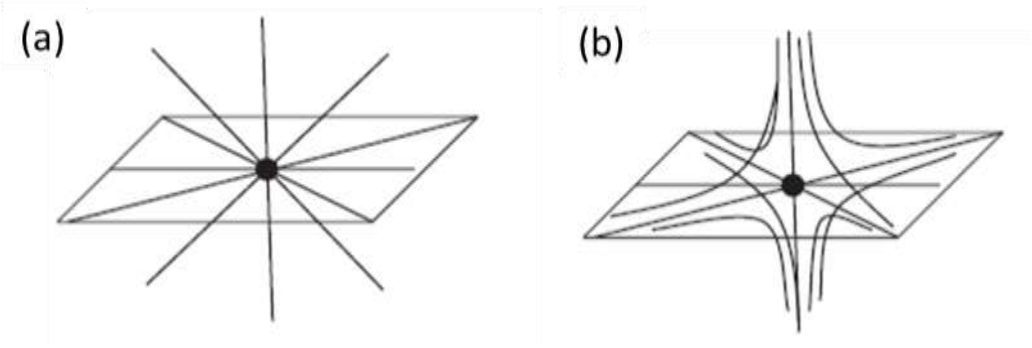

**Figure 2 Point defects in nematic liquid crystals adapted from reference [7] with permission. The solid lines are drawn along the nematic directors $\vec{n}$ (a) radial with (m=+1) hedgehog (b) hyperbolic (m= -1) hedgehog.**

Elastic deformations in director field $\vec{n}(r)$ are of three basic types: splay$(\vec{\nabla}.\vec{n} \neq 0)$, twist $\left(\vec{n}.\left(\vec{\nabla} \times \vec{n}\right) \neq 0\right)$ and bend $\left(\vec{n} \times \left(\vec{\nabla} \times \vec{n}\right) \neq 0\right)$. The equations in the brackets mathematically represent the deformations of corresponding type. The elastic energy associated with deformations is thus a sum of the three types as first proposed by Frank and Oseen[9] :

$$F_{frank} = \frac{1}{2}\int \left(k_{11}\left(\vec{\nabla}.\vec{n}\right)^2 + k_{22}\left(\vec{n}.\left(\vec{\nabla} \times \vec{n}\right)\right)^2 + k_{33}\left(\vec{n} \times \left(\vec{\nabla} \times \vec{n}\right)\right)^2\right) dV \qquad (1.2)$$

### 1.2.3C Anisotropy of optical properties

This section describes the beautiful colors that liquid crystals show between two linear polarizers kept perpendicular to each other. Liquids in isotropic state of random orientations of molecules possess a single refractive index such as water has refractive index of 1.33. However due to preferential orientation of mesogens (molecules or non-spherical colloids), liquid crystals have different refractive index along ($n_e$) and perpendicular ($n_o$) to the nematic director and the difference between the two is called optical birefringence $\Delta n$, given by ($\Delta n = n_e - n_o$) hence liquid crystals are optically anisotropic.

Nematic suspensions of platelets have two refractive indices due to orientation of platelets along a single direction. One is ordinary refractive index $n_o$; the other is the extraordinary refractive index $n_e$. For platelet nematic suspensions, the ordinary refractive index is in the direction parallel to platelet normals[10]. Linearly polarized light is divided into two components with vibrations parallel to the two refractive indices. The component vibrating parallel to $n_o$ is slower than that vibrating parallel to the $n_e$ direction. The two rays upon traveling a distance $d$ in the sample have a phase difference, $\delta$, given by [11]:

$$\delta = (2\pi/\lambda)\ (n_e - n_o)\ d \tag{1.3}$$

where $\lambda$ is the wavelength of the incident light. The two rays undergo interference after passing through the second polarizer oriented perpendicular to the first polarizer. The interference color depends on the path difference between the two components, also termed as retardation (R), which is product of the sample thickness and the birefringence ($\Delta n = n_e - n_o$) of the sample:

$$R = d\,(n_e - n_o) = d\Delta n \tag{1.4}$$

Since Δn is a function of platelet volume fraction, ϕ, one can control the birefringence color by tuning the concentration of platelets. The intensity after interference is given by[11]:

$$I = I_0\ sin^2\left(\frac{\delta}{2}\right)\ sin^2 2\theta \tag{1.5}$$

Here θ is the angle between incident polarization and the nanoplate normal in the plane perpendicular to the light propagation, and $I_0$ is the intensity of the light incident to the first polarizer. Note that a nematic domain can appear dark if $\theta$ is $0^o$ or $90^o$ i.e. when the platelets align with their normals in the direction parallel to any of the two polarizers or in the direction of propagation of light[10].

### 1.2.3D Response to external fields

The anisotropy of the liquid crystalline medium extends to the electric permittivity ($\varepsilon$) and magnetic susceptibility ($\chi$). These two properties are different along (||) and perpendicular (⊥) to the direction of orientation of mesogens and are given by the following relations:

$$\Delta\boldsymbol{\varepsilon} = \boldsymbol{\varepsilon}_{||} - \boldsymbol{\varepsilon}_{\perp} \tag{1.6}$$

$$\Delta\boldsymbol{\chi} = \boldsymbol{\chi}_{||} - \boldsymbol{\chi}_{\perp} \tag{1.7}$$

An applied external electric (or magnetic) field can thus reorient the director to minimize the free energy as per the following relationship [12]:

$$F_{field} = \frac{1}{2}\int\left(-\frac{\Delta\varepsilon}{4\pi}(\vec{n}.\vec{E})^2 - \frac{\Delta\chi}{4\pi}(\vec{n}.\vec{B})^2\right)dV \qquad (1.8)$$

## 1.3 Applications of disk-shaped colloids

### *1.3.1 Informational displays*

Liquid crystals due to their external electric field response are exploited in electronic informational displays which is a multibillion dollar industry[13]. Commercial LCD devices make use of a thermotropic LC with a nematic or twist bend nematic phase stable at room temperature. One of the drawbacks of conventional LC displays is that the range of temperature variation is narrow. For example, our cellphones when heated to over 55C, might form dead pixels. Dilute suspensions of colloidal platelets can be useful. Recently, graphene oxide based displays were shown to be promising due to extremely large sensitivity to external electric fields [14] . A big turndown for colloid based displays however is their slow response of on-off switching. Although switch on time is about 1ms, the switch off time is about 0.1s and it is the limiting step. With this limitation, places where relatively slow speed of information display is acceptable, such as display boards of prices of commodities in a supermarket, the colloidal platelet suspensions can be used. Among other challenges, colloidal stability and sedimentation are the challenges.

### *1.3.2 Tunable structure colors*

Smectic-like nanostructures of nanoplates distance between Smectic layers in the visible-wavelength range exhibit structural colors and the color can be tuned by modulating the nanostructure period using external stimuli such as magnetic fields[15].

### *1.3.3 Platelet based LC as anisotropic media*

Due to preferential alignment of colloidal platelet mesogens, the liquid crystal phases are fluid phase having anisotropy. The anisotropy can be exploited for materials processing such as spray-coated smectic-like films of zirconium phosphate have exceptional gas barrier properties due to tortuous path provided to the gas molecules through the layered arrangement of platelets[16]. Moreover, recent progress in using topological defects to concentrate swimming bacteria [17] and driving the bacterial traffic along the director deformations have opened pathways for the applications of liquid crystals beyond informational displays[18]. Biocompatible platelet suspensions in nematic phase in principle can prove to be more useful due to much larger size of the defect cores (up to 40-50μm) in platelet nematic than those in molecular nematic (up to 10μm).

### *1.3.4 Thermo-selective transport of biomolecules*

As will be shown later in this dissertation colloidal platelets show thermophoresis and can be moved to either the hot or the cold. Due to high surface to volume ratio, platelets have more efficacy than spheres. Biocompatible platelets[19,20] such as zirconium phosphate can prove to be better candidates for the same.

### *1.3.5 Drug delivery*

Exploiting the interlayer spacing between the stack of platelets, cancer treatment drugs can be loaded with up to impressive 35% uptake to deliver to the target cells. Drugs can also be encapsulated using platelets and thus protected during their transport to target cells that usually happens via acidic gastro-intestinal pathways in which bare drugs are vulnerable.

## 1.4 Zirconium-phosphate nanoplates as model platelet colloids

A lot of materials are made up of highly anisotropic platelets, such as clays,[21] asphaltenes,[22] graphite,[23,24] MXenes[25] and layered semiconductors.[26] That is why the understanding of the structures and properties of platelets is important. Simulations on cut spheres show a phase diagram that predicts isotropic-nematic-columnar phase transition[27,28]. To explore the phase behavior of concentrated suspensions of platelet colloids, zirconium phosphate nanoplates are used as a model system of platelet colloids as they provide uniform thickness[5,29], precise control on the lateral size and hence on the thickness over diameter ratio called aspect ratio ($\xi$) [30,31]. Moreover, the zirconium phosphate nanoplates are highly anisotropic shape i.e. very small aspect ratio($\xi$) [32,33] and have low shape and size polydispersity. Highly anisotropic nanoplates with $\xi<0.1$ are achievable via controlled growth of layered inorganic crystals[30]. The nanoplates obtained via exfoliation of the layered crystals have identical thickness of the order of 1 nm.

### *1.4.1 Phase diagram of platelet suspensions*

As can be followed from figure 3, the high anisotropy of disks ($\xi<0.23$) is required to form liquid crystal phases. The formation of nematic (*N*) phase requires an even higher degree of shape anisotropy: $\xi<0.15$, otherwise, a direct transition from the isotropic (*I*) phase to the columnar (*C*) phase. Historically, Langmuir's experimental work on the I-N transition of plate-like hectorite clay [34] was an important source of inspiration for Onsager in his theoretical treatment of the I-N phase transition in systems of anisotropic particles with purely repulsive interactions[35].

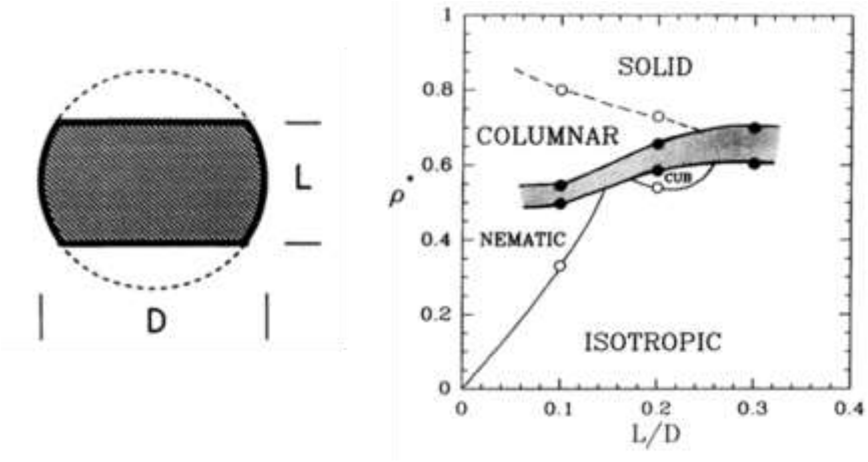

**Figure 3. (left) picture of cut sphere (right) phase diagram of cut spheres predicted from Monte-Carlo simulations adapted from reference [36] with permission**

## 1.5 Organization

This dissertation is organized as follows. The experimental investigations on the phase behavior of nanoplates is presented in Chapter 2. Highly anisotropic zirconium phosphate nanoplates with thickness to diameter ratio as low as 0.0025 are synthesized and the phases shown by their aqueous suspensions with increasing concentration of nanoplate colloids are studied. Phase sequence exhibited by single sample kept in a tall container for long in gravity is shown. The formation of large nematic domains in cylindrical confinement after prolonged annihilation in gravity is also presented and corresponding director distribution is sketched.

The kinetics of isotropic to nematic phase transition is discussed in Chapter 3. An extension of classical nucleation theory model adapted to plate-like colloids following that of spherical colloids is presented. Experimental measured nucleation and growth rate kinetics will be discussed for samples in I-N coexistence regime.

Chapter 4 concerns with the electric field control of nanoplates and the new phases stabilized by the field. A positive evidence for biaxial nematic phase stabilized by the electric field is shown. Kinetics of defects annihilation in presence of field is also studied.

External temperature gradient allows driving particles to one end of the gradient sample which essentially allows controlling local concentration of colloidal particles which eventually can help control their phases that are concentration dependent. Such thermophoretic control on the growth of nematic LC is discussed in Chapter 5.

The measurement of thermodynamic equation of state which relates osmotic pressure to the colloid volume fraction is presented in Chapter 6. Integration of volume fraction profile in equilibrium sediment gives osmotic pressure and hence the volume fraction profile measurement was critical. Nematic volume fraction profile is measured with help of optical imaging of long-time gravity sedimented sample kept in between crossed polarizers and aligned by external magnetic field to exhibit colors related to the concentration at a given height. Isotropic volume fraction profile was measured using X-ray attenuation technique.

# CHAPTER II

# PHASE DIAGRAM OF NANOPLATES

## 2.1 Abstract

Suspensions of highly anisotropic nanoplates of TBA exfoliated zirconium phosphate $Zr(HPO_4)(Bu_4NPO_4)$ are prepared with increasing volume fraction. With increase of volume fraction caused phase transition from isotropic to isotropic-nematic-lamellar phase transition. The lamellar phase is characterized by small angle X-ray scattering (SAXS). At much longer times, nematic sample kept in long cylindrical tubes showed following features- large nematic domains formed with the escape of nematic director perpendicular to the cylinder walls and then escaped along the axis of cylinder. Nematic-nematic separation was also observed due to fractionation of nanoplates with larger nanoplates towards the bottom.

## 2.2 Introduction

Nematic phase in platelet suspensions was reported for the first time in 1998[4]. At higher volume fraction, formation of columnar phase in nanoplates with a phase transition sequence isotropic (I) – nematic (N) – columnar (C) with the increase of nanoplate concentrations[37]. A decade later, Sun et. al.[38] reported formation of stable smectic phase in suspensions of charged nanoplateletes and argued that the smectic phase was stabilized by the size polydispersity. In their system, however, the columnar phase was not formed, and the phase sequence was isotropic (I) – nematic (N) – smectic

(S) was claimed with the increase in nanoplate concentrations. As stated before, the smectic phase has long range positional order of the mesogens and hence shows a sharp peak in the 1D x-ray scattering profiles; however, the peaks observed in the claimed smectic phase were indicative of positional order over the range of two-three layers of smectic which can be argued to be of relatively short-range order. More recently, other researchers have also reported formation of smectic phase of such as in gibbsite nanoplates suspended in dimethyl sulfoxide[39]. They argued the use of polar aprotic solvent, led to a long range of the electrostatic Coulomb repulsion between platelets. They further claimed the phase to be Smectic B ($Sm_B$) type through high resolution x-ray scattering experiments. In a more recent article, silica coated gibbsite platelets is aqueous suspensions have been reported to have formed smectic phase[40] which destabilized to nematic upon addition of salt which further strengthened the idea of Coulomb repulsion being responsible for the long range positional order. They also argued through simulations that the columnar phase is stable when the polydispersity of the platelets is low (as low as 17%) and in the hard platelet limit i.e. at high salinity conditions.

Chirality of the nematic phase of nanoplates is a very interesting topic as the platelets are achiral and the electrostatic interaction between the charged nanoplates can potentially lead to chiral phase formation. Gao et. al.[24] claimed that at 0.78% volume fraction of Graphene Oxide (GO) aqueous suspension, the circular dichroism spectra shows a peak at 420nm wavelength and that the peak had an ellipticity value 2200 mdeg which is quite strong indication of chirality which conventionally is considered present if the peak has a value greater than 40mdeg and if the peak position is between 200nm to 700nm. A counter argument can be given that even without a presence of strictly chiral nematic order, any two charged nanoplates can also show a peak in CD spectra. In graphene oxide liquid crystals the polarized optical microscopy did not reveal a promising fingerprint texture[24] as observed in a typical chiral nematic liquid crystal. The claimed fingerprint textures in graphene oxide that seem like textures formed due to hydrodynamical instability.

## 2.3 Synthesis of monolayer ZrP and size characterization

6g of zirconyl chloride octahydrate (ZrOCl2·H2O, 98+%, Acros Organics) and 60mL solution of 12M phosphoric acid (obtained using 15M, 85%, Fisher Scientific) were added to a round bottom flask and mixed well using stir bar. The mixture because viscous as the product amorphous zirconium phosphate was formed in few minutes due to the following reaction.

$$ZrOCl_2.8H_2O + 2H_3PO_4 \rightarrow Zr(HPO_4)_2.H_2O + 2HCl + 8H_2O$$

To obtain zirconium phosphate disks, a high temperature (200ºC) crystal growth using hydrothermal method was followed [41] in which the resulting mixture was poured into a 100 mL PTFE container and placed in an a well tightened, metal container called autoclave. The autoclave was kept in an oven at 200°C for 24 hours and then removed. The lateral size of pristine α-ZrP disks thus formed was a function of the duration of time for which the autoclave was kept in the oven and the initial concentration of phosphoric acid in the reaction mixture. It was systematically shown that higher the acid concentration and the higher the reaction time, the larger was the size of the disks[30]. After removing from the oven, the autoclave was left idle to cool down under ambient temperature conditions. After the autoclave cooled down, the PTFE container was removed from the autoclave and the liquid part of the product was collected in waste acid bottle. A thick white suspension that remained at the bottom had α-ZrP disks. The trace of acid that remained was washed away. The process for washing away the acid involved addition of 40mL fresh millipore water, vortex homogenizing of the suspension and centrifuging the suspension 2500 g for 10 min. The process of washing was repeated a total of three times to ensure that all the acid is washed away. After washing, the sample was then dried in an oven at 64°C for 12 hours. The dried sample was then ground with a mortar and pestle into fine powder and the pristine $Zr(HPO_4)_{2,}$ also known as α-ZrP, were stored in a container. The Scanning electron microscope (SEM) image of pristine α-ZrP is shown in figure 4(a).

Intercalation of pristine α-ZrP was done using tetra-(n)-butyl ammonium hydroxide ($Bu_4NOH$) was required to obtain monolayer ZrP. 1 g of α-ZrP was dispersed in 7.8 mL millipore water and the resultant suspension that formed looked milky. 2.2 ml of tetra-n-butyl ammonium hydroxide, TBAOH (40 wt. % Fischer Scientific) was added to it and vortexed for at least 40 sec and sonicated for 1-1.5hr at 60mW sonication bath. Sonication with higher power might rupture the nanoplates. Tetra butyl ammonium ions went in between the layers and broke interlayer hydrogen bonds and monolayer ZrP-TBA nanoplates were formed. Transmission Electron Microscope (TEM) image ZrP-

TBA nanoplates (henceforth referred to as ZrP nanoplates) is shown in figure 4(b). Thickness of monolayers thus obtained was uniform as visible from the uniform contrast of all nanoplates in TEM image. The value of thickness was about 3.8 nm (close to 2.68nm from atomic calculations[29]) as found using Atomic Force Microscopy (AFM) image shown in figure 4(c) and the corresponding profile hown in figure 4(d) which was the height of the sample along the white line drawn in figure 4(c). Lateral size of nanoplates was about one micron and thickness few hundred nanometers and was controllable by manipulating phosphoric acid concentration and hydrothermal reaction time. The polydispersity of these nanoplates was within 20% as analyzed by Dynamic Light Scattering (DLS).

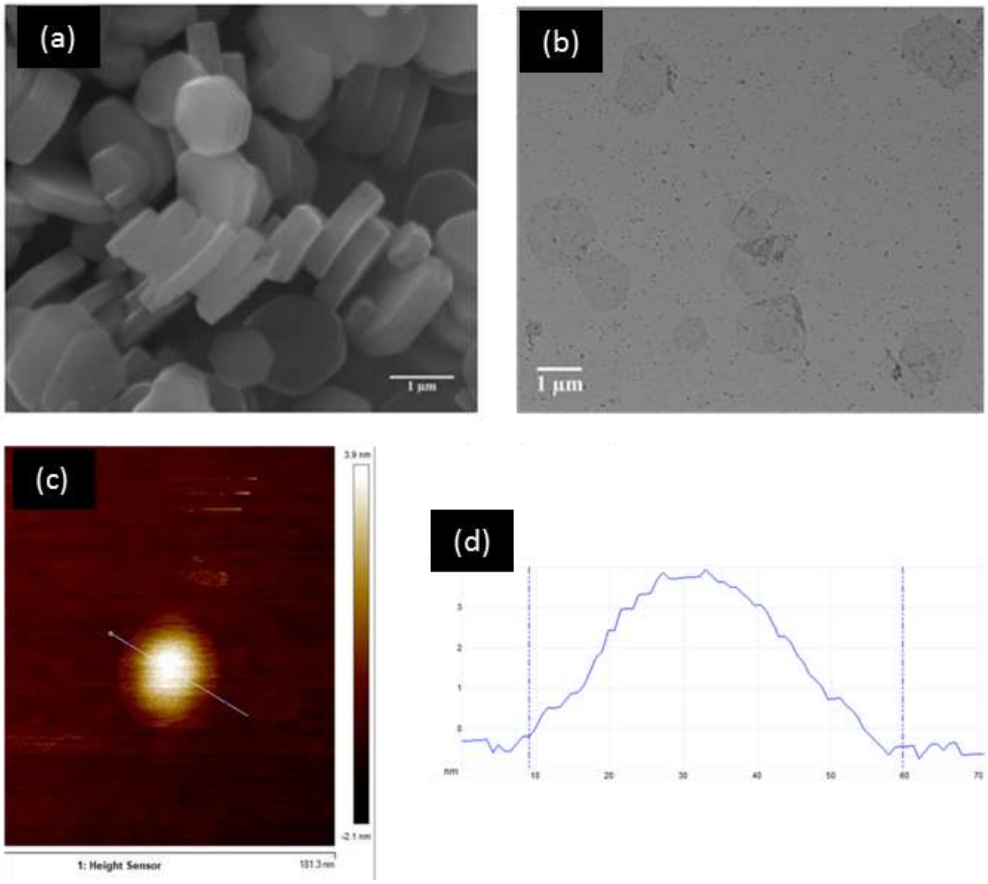

**Figure 4 (a) SEM image of pristine α-ZrP. Thickness is about 0.2μm indicating few hundred ZrP monolayers held together in single disk due to Van-der-Waal forces. Figure adapted from reference [42] with permission (b) TEM image of monolayer ZrP-TBA nanoplates with chemical formula $Zr(HPO4)_x( Bu_4N^+ PO_4^-)_{2-x}$ obtained via exfoliation of pristine α-ZrP disks shown in part a. Similar contrast of different nanoplates indicated monolayers were uniform in thickness (c) AFM image of a smaller ZrP nanoplate (monolayer) (d) Profile of the height of nanoplate along the solid line in part (c) shows the thickness is ~3.8nm.**

The nanoplates were characterized using a dynamic light scattering instrument Zetasizer Nano- ZS. The DLS gives diameter of sphere which is equivalent to the hydrodynamic diameter of platelet; to find out the actual lateral size of the platelet, the following model was used[43]

$$t = \frac{k_B T}{3\pi\mu D^*_{disk}} \frac{\arctan(\sqrt{\xi^{-2}-1})}{\sqrt{\xi^{-2}-1}} = 2R_{sphere} \frac{\arctan(\sqrt{\xi^{-2}-1})}{\sqrt{\xi^{-2}-1}} \qquad (2.1)$$

where $D^*{}_{disk}$ is the diffusion coefficient of the platelet measured by using DLS and $\xi$ is thickness to diameter ratio of disks and t is the thickness of the disk. Since the thickness of monolayer ZrP is known to be 2.68nm, the diameter can be found from equation 2.1.

## 2.4 Results and discussion

### *2.4.1 Images between crossed polarizers as a function of volume fraction*

Mother suspension with ZrP nanoplates with average size, 1.05µm and polydispersity, 19% at mother suspension concentration of 4.1% concentration is obtained by exfoliation of 1g pristine ZrP exfoliated with 2.2mL tetra (n) butyl ammonium hydroxide and subsequent removal of excess TBA ions via centrifugation of samples at low speed 2600g, twice each for 30 minutes and removal of top supernatant and leaving the suspension overnight. The mother suspension when filled in 8mm tube and kept between crossed polarizers looks like sample 8 in figure 5. Other samples with lower concentration are obtained via dilution of the mother suspension. Sample 9 (not shown in the figure but looked very similar to sample 8) is obtained by further concentrating the mother suspension via centrifugation and supernatant removal to a final concentration of 4.8% vol/vol. Samples 10, 11 and 12 are obtained via direct exfoliation of pristine alpha ZrP in relatively lower volumes of water and are observed directly with no further salt removal.

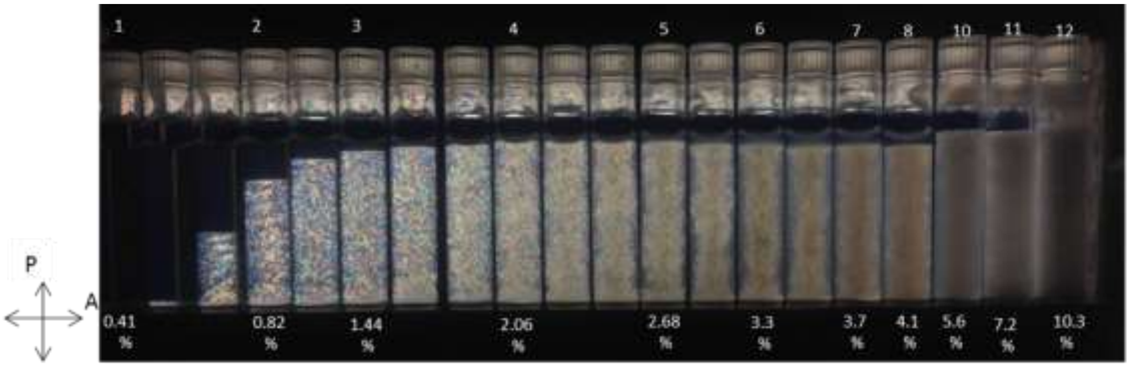

**Figure 5 Snapshot of suspensions of monolayer ZrP nanoplates at different volume fractions kept between crossed polarizers captured five days after homogenization.**

From the observation between crossed polarizers, the colored phase indicates liquid crystallinity, but it does not explain which liquid crystalline phase it could be. However, from the simulated phase diagram of nanoplates (figure 2) we can say it is a nematic phase. But the liquid crystal phase in samples 5, 6, 7, 8 and all the other samples in between them showed a different texture (emptier towards the walls and concentrated at the center and roughly showing some fibrous textures) than that in samples 2 through 5. A reason could be formation of chiral phase and it needed further characterization such as polarized optical microscopy and small angle x-ray scattering. Samples 10, 11 and 12 looked more non-transparent because of high viscosity which could be a different phase than nematic.

### *2.4.2 Polarized optical micrographs of suspensions*

The defects in liquid crystals can help identify the liquid crystal phase and hence capillaries with 0.2mm thickness, 2mm width and 50mm length were loaded with samples and kept vertical in gravity. Despite sealing the ends of capillaries, slow evaporation of solvent lead to slightly increased concentrations after months. Figure 4 summarizes the different textures observed in the suspensions. Figure 5(a) shows typical droplets of nematic phase exhibiting typical four brush defect with the singularity point at the center while the dark phase is isotropic thus indicating a I-N coexisting phase. Four brush defects in figure 5(b) indicate fully nematic liquid crystal phase. Figure 5(c) has defects which are not standard to any of the liquid crystalline phase. However, since this texture formed at a relatively higher volume fraction of nanoplates, i.e. at 4.8%, and after a few days of keeping the capillary vertical, a local I-N phase separation could have led to the formation of this texture. The dark lines indicating the isotropic phase and the bright domains indicating nematic. However, the dark spots in between are still to be well understood. Figure 5(d) indicates periodicity of the order of 1 micrometer. This is most likely due to the onset of the positionally ordered phase but since it did not show a focal conic defect, it is not clear if it is a smectic phase. From the small angle X-ray scattering data, more comments can be made.

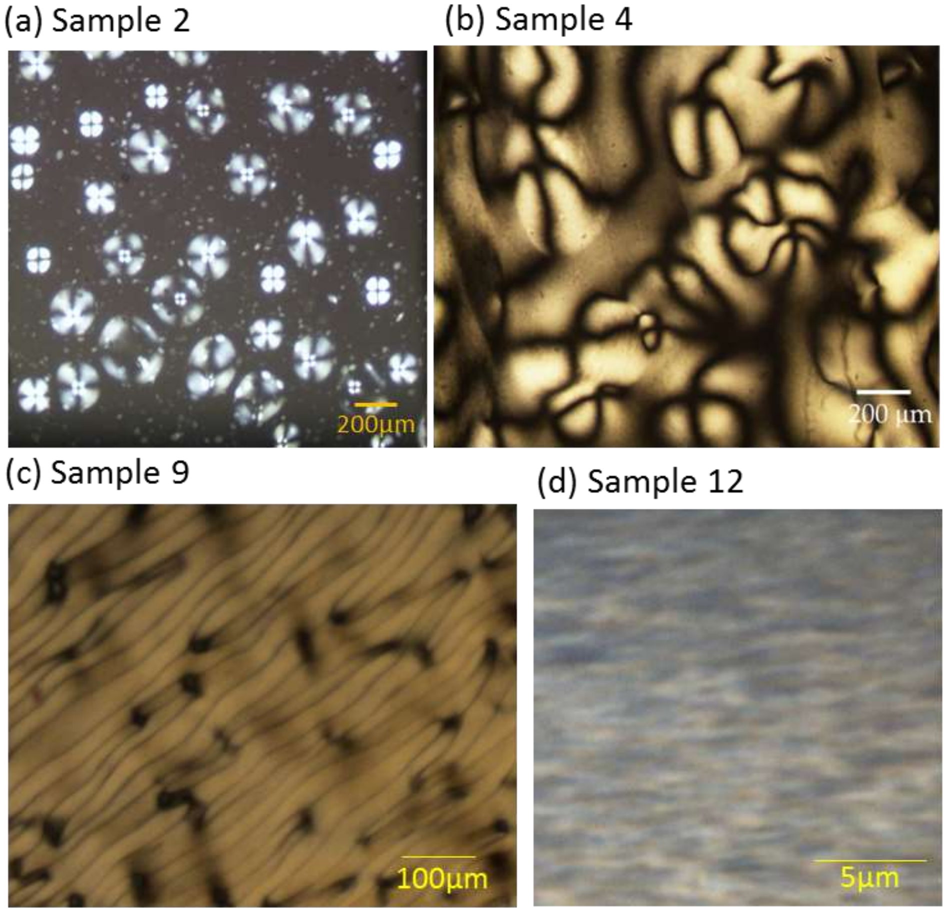

**Figure 6 POM images of ZrP suspension at different volume fractions. (a) nematic islands showing hedgehogs with m=+1 defects at isotropic-nematic phase coexistence samples at ϕ = 0.82% (b) full nematic phase showing continuous, smooth texture of nematic phase called schlieren texture at ϕ = 2.06% (c) Stripe pattern formed at ϕ = 4.8% and (d) Periodic structure with submicron scale period observed in sample in smectic phase, ϕ = 10.3% . The sample cell was 200μm thick capillary and the observations were made.**

### *2.4.3 Small angle X-ray Scattering*

To enhance the partial understanding of the liquid crystalline phase at higher ZrP volume fractions, samples were sent to European Synchrotron Radiation Facility (ESRF) for small angle X-ray scattering (SAXS). Figure 7(a) shows isotropic scattering (sphere in 2D image on the left) and no presence of peaks in 1D scattering profile. The scattering follows q-2 dependence which is typical of isolated platelets. Figure 7(b) shows anisotropic scattering indicating presence of optical anisotropy. Two broad peaks in intensity vs wave vector (q) curve (figure 7b) were observed. From the peak value at $q = 0.35$ nm-1, the d-spacing between platelets can be calculated as $d=2\pi/q$ = 17.9nm. Although nematic phase does not have positional order, the d-spacing gives distance between two plates and the broadness of the peak is indicative of no long range positional order which is characteristic of nematic. At higher ZrP monolayer concentrations, $\phi$=4.8%, anisotropic scattering (figure 7c, left) with three to four broad interference peaks (figure 7c, right) are observed which indicate platelet stacking with d-spacing decreased to 12.9nm. At $\phi$=10.3%, d-spacing further decreased to 5.3nm however the interference peaks were sharper which is due to relatively long range positional order. Since the d-spacing does not lie in the visible range, the iridescence was not observed in samples. So the periodicity of sample 12 as shown in (figure 6d) was not due to possible smectic layers as the layer spacing found via SAXS was much lesser than the period observed in POM (~0.5μm).

(a) Sample 1

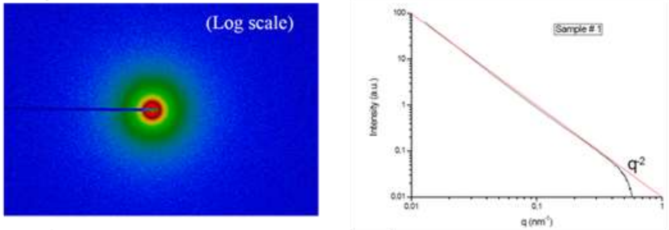

(b) Sample 4

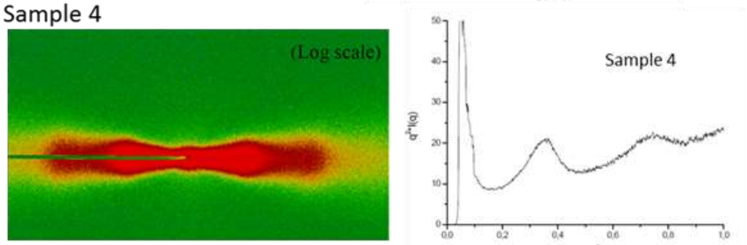

(c) Sample 9

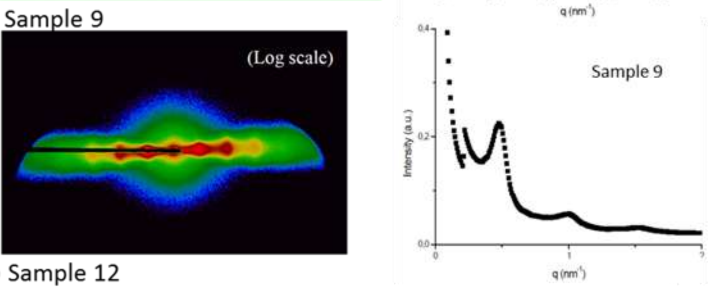

(d) Sample 12

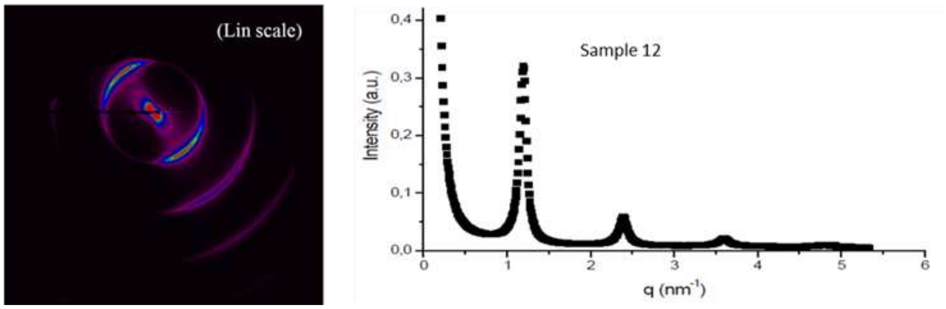

**Figure 7 Small Angle X-ray Scattering profiles, left column (2D) and right column (1D) of monolayer ZrP suspensions at (a) 0.41% (b) 0.82% (c) 2.06% (d) 4.8% and (e) 10.3% by vol.**

### *2.4.4 Circular dichroism measurements*

Due to differential absorption of left and right circular polarized light, circular dichroism helps characterizing the chiral liquid crystalline phases[44,45]. Figure 8 shows CD spectra of different volume fraction suspensions of ZrP monolayers. That the ellipticity defined as, $\theta = \tan^{-1}\left(\frac{\sqrt{I_R}-\sqrt{I_L}}{\sqrt{I_R}+\sqrt{I_L}}\right)$. Ellipticity should have a peak in between 200 to 700 nm for a sample to be chiral and the strongest peak was obtained for ϕ =1.81%. The samples within the concentration range ϕ = 1.38% and ϕ = 2.54% exhibit chiral interactions. Interestingly, in ZrP monolayers negative peaks were also observed which strengthens the argument that the chirality in achiral nanoplates could be because of electrostatic interactions which could lead the phase to be either left handed (negative peak) or right handed (positive peak).

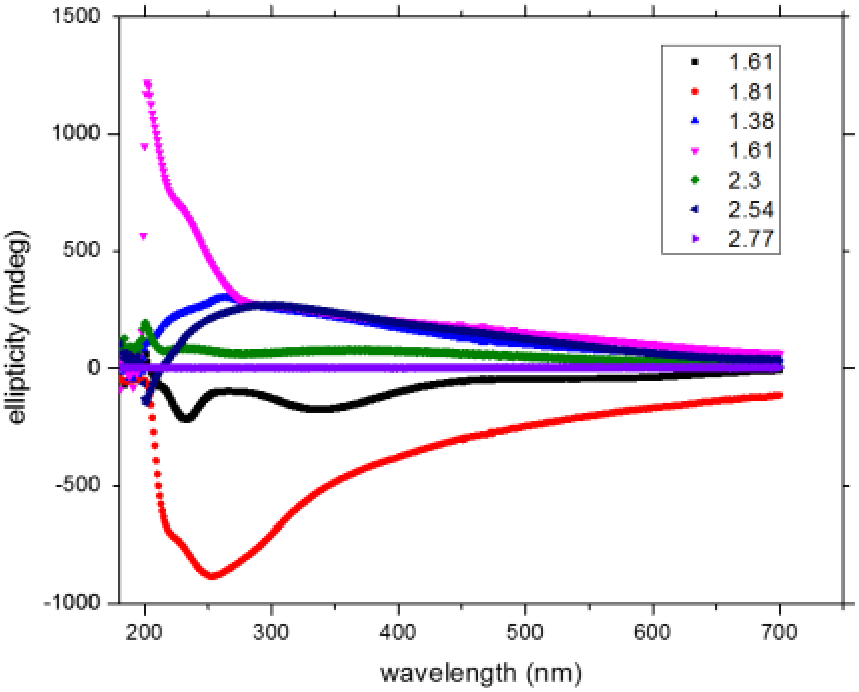

**Figure 8 Circular dichroism spectra of nanoplate suspensions at different concentrations 1.61 %, 1.81%, 1.38%, 1.61% (repeated measurement), 2.3%, 2.54% and 2.77%**

### *2.4.5 Phase diagram*

The phase diagram thus established from above experiments for the ZrP nanoplates can be shown follows:

**Figure 9 Phase diagram of ZrP nanoplates of size 1µm ± 0.15 µm**

The smectic phase yet needs to be fully understood and although the characteristic focal conic defects of smectic phase were not observed, SAXS experiments showed evidence of positional order and it is anticipated that when samples at such high concentration when they reach equilibrium will exhibit typical smectic defects. The smectic domain size required for the same is much larger and microgravity can help grow larger domains and equilibrium is hypothesized to achieve in relatively shorter times.

### *2.4.6 Gravity induced density gradient & phase coexistence*

Gravity creates a density gradient in a vertically placed tube containing nanoplate suspensions, which lead to multiple phases coexistence at a given sample volume fraction and changes with time. Figure 9(a) shows Lekkerkerker's sedimentation equilibrium model[46] for Isotropic, Nematic and Columnar phases, which we adapted to the ZrP-TBA system that showed I, N and S phase transitions as shown in Figure 9(b). Gravitational length, $l_g$, for the monolayers of ZrP of lateral size 1µm is ~0.3mm as calculated using expression $l_g = k_B T/m^* g$, where $m^*$ is buoyant mass of nanoplates.

When the sample height (H) is much larger than the gravitational length, gravity sedimentation overcomes thermal energy of colloidal nanoplates and the sedimentation induced density gradients were expected to increase the nanoplate concentration as one goes from the top to the bottom of the sample tube. The gravity induced phase coexistence shown in figure 9 (a) and (b) is theoretical and can be experimentally observed if enough time to reach the equilibrium is allowed and due to slow kinetics, colloidal nanoplates might take months to years for the equilibrium to reach. Figure 9(c) shows a sample of height 14 cm, with an initial volume fraction $\phi_0 = 0.02$ (nematic), in a cylindrical container with $H/l_g$ =466>>50. Picture was taken three years after the preparation of the sample which in the beginning was fully nematic. Four different textures were observed from the top of the sample to the bottom and were identified as isotropic (dark), nematic (bright with different color domains), nematic (transparent, homogeneous color showing a coarsened nematic) and smectic (bottom). The textures of I-N coexisting phases on the upper part of the sample were seen in the sample that was kept vertical in 1g for a few months. The phase in the bottom part of the sample might be smectic phase assuming the concentration reached more than 10% and following the SAXS measurement of independently prepared samples at that concentration.

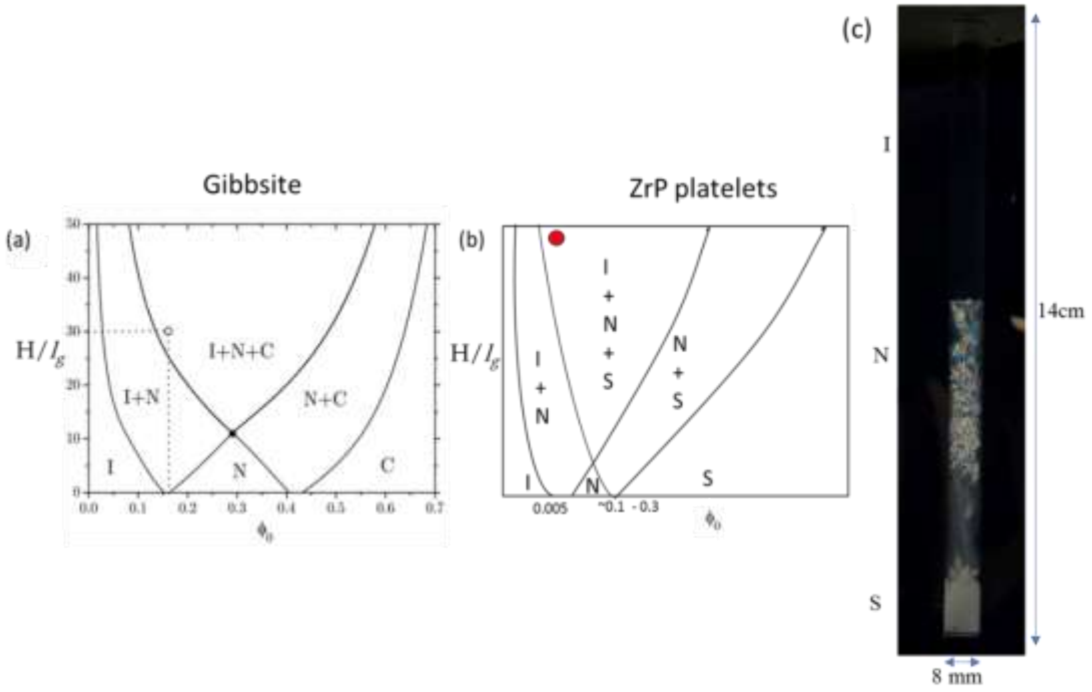

**Figure 10 Effect of gravity on nanoplate phases. (a) Phase coexistence based on sedimentation equilibrium model for platelets which show isotropic, nematic and columnar phases. Adapted from reference [47] reproduced with permission. (b) Extension of sedimentation equilibrium model to the system of ZrP monolayers showing I-N-S phase transition and phase coexistence depending on height of the sample tube. (c) Phase coexistence observed in a sample with $\phi_o = 0.02$ after keeping vertical for 3 years. (aspect ratio, $\xi = 0.0025 \pm 0.0004$). Sample picture taken by keeping the sample between crossed polarizers.**

### *2.4.7 Extremely large nematic monodomains in cylindrical confinements*

Nematic suspensions kept in cylindrical confinement were observed for the textural changes over relatively longer durations of time, up to a few months. A few hours after homogenization, differently oriented small nematic domains formed in a sample close to fully nematic $\phi$ ~ 7% as shown in figure 11(a). The I-N coexisting to full N transition $\phi$ in this case is higher because nanoplates of smaller lateral size, ~200 nm were used for relatively faster rotational and translational diffusion constants.[42] As the time elapsed, two things happened. One, the isotropic inclusions in the nematic phase slowly got released to the top and the height of the nematic in figure 11(b) decreased as can be compared from figure 11(a). When the polarizers were rotated by $45^{o}$, the inversion of bright and dark domains were observed as shown in figure 11 (c). A magnified image of the sample focusing on the defect is shown in figure 11 (d). From the argument on intensity of light coming out of crossed polarizer, $I \propto sin^{2}2\theta,$ where $\theta$ is the angle between incident polarization and nematic director $\vec{\boldsymbol{n}}$, the dark portion (figure 11a,c) near the curved wall of the cylinder has $sin^{2}2\theta = 0$ i.e. the nematic director near side wall is making $\theta$=$0^{o}$ or $\theta = 90^{o}$ angle with vertical. Similarly, the axis of symmetry of cylinder has either of the two orientations of the director. Since the walls were hydrophilic, hydrophilic ZrP nanoplates tend to wet the surface of the container and hence align with the nanoplate faces parallel to the wall thus making the directors horizontal which implied $\theta = 90^{o}$. Splay deformation leads to a slow escape of the director along the cylindrical axis as schematically shown in figure 11(e). The hedgehog defect (m=-1) is clearly visible in figure 11(d); it is not clear if the hedgehog (|m|=1) is already split into (|m|=1/2) defects. This spontaneously homeotropically anchored and nematic director escaped along the z-axis of the cylinder type of configuration has been observed for the first time in nanoplate liquid crystals. Due to slow rotational and translational diffusion of nanoplates, the dynamics of domain coarsening are rather extremely slow as it required about 8 months for the system to achieve equilibrium.

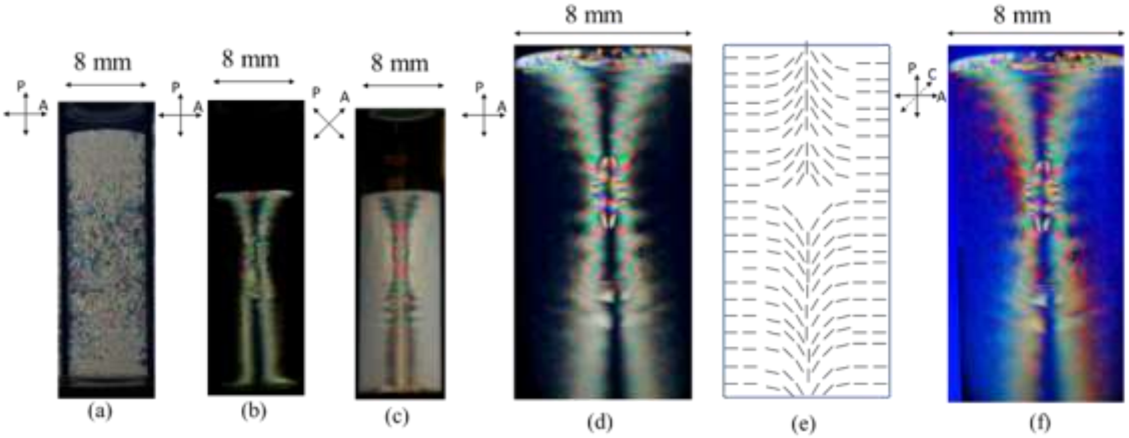

**Figure 11 Crossed polar images of a nematic suspension of smaller ZrP nanoplates (avg. size = 300nm) with $\phi$~7% kept in a cylindrical vial of diameter 8mm (a) one day after homogenization (b-f) 8 months after homogenization. Polarizer (P), Analyzer (A) and slow axis of full wave plate (C) directions are as shown with the arrow.**

## 2.5 Conclusion

Isotropic to nematic to smectic phase transition was observed in highly anisotropic zirconium phosphate nanoplates. Topological hedgehogs in nematics were observed between crossed polars and the giant monodomain nematic in cylindrical confinement formed after months of coalescence was indicative of slow dynamics of nanoplate liquid crystals. Although sharp peaks at higher concentration were indicative of smectic order, absence of typical focal conic defect of smectics was eluded perhaps due to smaller domains and extremely slow kinetics of nematic to smectic transition due to high viscosity and gravity stress. Observation of different textures in a single, long sample tube kept in gravity showed further evidence to the I-N-S phase transition in suspensions of nanoplates. Further studies including microgravity environment could help grow larger domains of smectic due to faster kinetics in micrograity.

# CHAPTER III

# KINETICS OF NUCLEATION AND GROWTH OF NEMATIC LIQUID CRYSTALS OF NANOPLATES

## 3.1 Abstract

Colloidal suspensions of anisometric nanoparticles have promising applications. From fundamental standpoint, the colloids are models for molecular systems and allow studying the molecular phenomena such as phase transitions on convenient length and time scales, micrometer and few seconds to few hours, respectively. We deployed light microscopy with crossed polars to study nucleation and growth speeds of nematic phase of nanoplates. The growing nematic nuclei, called tactoids, were tracked as a function of time to find linear relationship of their number in nucleation regime in accord, qualitatively with the predictions from classical nucleation theory. The nature of growth was found to be diffusion limited in early times and interface limited at longer times. Classical nucleation theory was adapted to colloidal platelets and the nucleation and growth rates were compared with experimentally measured values. Our findings on the dynamics of phase transitions in lyotropic liquid crystals based purely colloids are first of its kind and apply to a wide range of systems such as graphene (2D), cellulose nano crystal (1D) that have gained popularity in recent years for the design of advanced functional materials.

## 3.2 Introduction

Colloids are particles of one medium, in the size range of one nanometer to a micrometer, dispersed in another medium. They play an important role in different areas of science and technology. For example, ferrofluids[48], medical applications[49], photonic crystals [15,50] phases. More interestingly, colloids can act as models to experimentally probe for molecular systems as the interaction of colloids are tunable [51] and ability to synthesize required shape and sizes, it has become possible to study molecular scale physical phenomena on a much larger, microscopic length-scale. One of the very interesting physical phenomena is the melting phase transition of materials that can be studied using colloids as models. In the holy grail of colloidal science, it was studied in great details by using spherical colloids as models [52,53] that closely represent hard spheres with purely entropic interactions, and the kinetics of nucleation and growth speeds using light scattering techniques [54-56]. Although much attention was received to colloidal crystals, very less has been achieved to the colloidal liquid crystals. Liquid crystals are novel phases of matter that have molecular order in between that of disordered liquids and perfectly ordered crystals. Technologically, this phase is important for its application in modern electronic displays.

Lars Onsager [35] explained in his seminal work, the formation of liquid crystalline nematic phase in suspensions of anisotropic colloids such as rods and platelets. Above a critical number of colloids present in the suspension, the gain in positional entropy upon alignment with each other overcomes the loss in orientational entropy of random orientations. The first phase transition with increase of concentration of nanoplates is the isotropic to nematic phase transition. From theoretical [35] and experimental observations [37], the nature of this phase transition is first order. First order phase transitions could follow either nucleation growth kinetics or spinodal decomposition. Lekkerkerker [57] and others pointed that the kinetics of phase transition from metastable liquid to nematic liquid crystal in plate-like colloids follows nucleation and growth of nematic nuclei called tactoids. Although there are several reports on hard sphere crystallization [54-56], there is none for hard platelets. The tactoid nucleation and growth however was not studied before due to several challenges. First, inability of the temperature-melting of these colloidal crystals, one is forced to shear-melt the liquid crystals which is hard to achieve in micro-confinements. Second, the growing nematic phase is denser than the surrounding liquid phase and hence undergoes sedimentation, convection and gravity stress due to gravity.

Our initial experimentation showed that typical timescale of the nematic liquid crystallization in nanoplate suspensions is a few minutes to a few hours and that the isotropic-nematic phase separation under the influence of gravity showed that the kinetics was faster for platelets smaller in size [42]. The study did not include microscopic observations of the nucleation and growth event was lacking. We here found that the nematic nuclei nucleate from the metastable isotropic suspension and then grow to become nematic islands of a few tens of micrometers and later coalescence with one another. A big challenge in studying the kinetics was to deal with the gravity sedimentation. Since, the thickness of typical optical microscopy sample cell is a few micrometers, the nuclei of the growing nematic phase would sediment within few minutes and would go out of focus, thus eluding the observation of their growth process. This challenge was overcome by making the light path for microscopy perpendicular to the gravity sedimentation direction of the nematic nuclei by modification of the conventional optical microscopy setup. Assuming the influx and out flux of sedimenting nuclei through the field of view was the same, sedimentation and convection effects were neglected. The polarized optical microscopy observations of nuclei in two dimensions was assumed to well represent the three-dimensional nucleation and growth process.

### *3.2.1 Adaptation of classical nucleation theory to platelet colloids*

Formation of nematic liquid crystals involves breaking of symmetry of random orientations of molecules by aligning with one another. In this process, molecules undergo translational and rotational diffusion. Frenkel (1946) first conceptualized the basic theory of nucleation [58] in which the total free energy of a crystallite that forms in a supersaturated solution is given by : $\Delta G = \frac{4}{3}\pi R^3 \rho_S \Delta\mu + 4\pi R^2 \gamma$, where $\rho_S$ is the number density of the solid, $\Delta\mu$ is the chemical potential difference between the solid and the liquid and $\gamma$ is the solid-liquid interfacial free energy. First term accounts for the difference between the chemical potential of the new phase and the current phase. The second term considers the energy associated with the newly created surface between the two phases. Since the two terms are competing, the free energy functional reaches a maxima at $R_{crit} = \frac{2\gamma}{\rho_s|\Delta\mu|}$, which results into the nucleation rate as, $N = \kappa\, exp\left(-\frac{16\pi}{3}\frac{\gamma^3}{(\rho_s|\Delta\mu|)^2}\right)$. Successful adaptation of this theory for colloidal disorder-order transition was progressively achieved by Cape, Russel as follows [59]:

$$\frac{\Delta G}{Nk_BT} = 1.1\phi^{-2}\left(\frac{\pi_{iso}(\phi)}{\pi_{I-N}}\right)^{-8/5}\left[ln\left(\frac{\pi_{iso}(\phi)}{\pi_{I-N}}\right)\right]^{-2}$$

$$N = \frac{1}{k_BT}\frac{D_s}{\sigma^5}\phi^{\frac{5}{3}}exp\left(-\frac{\Delta G}{k_BT}\right)$$

The growth of the nuclei by addition of individual colloidal particles to the nematic liquid crystal tactoids can be given by the Wilson-Frenkel law of crystal growth. The interface velocity is thus:

$$u = \frac{\alpha D_s}{\sigma}\left(1 - e^{-\frac{\Delta\mu}{k_BT}}\right)$$

In this work, we directly applied above framework to the isotropic-nematic phase transition in colloidal platelets. Models for thermodynamic variables such as osmotic pressure and the chemical potential in the isotropic and isotropic-nematic coexisting phases are obtained from the generic equation of state of colloidal platelets proposed by Wu and coworkers [60]. The osmotic pressure of the isotropic phase is given by:

$$\frac{\pi_{iso}(\phi)V_p}{k_BT} = \phi + K\frac{4\phi^2 - 2\phi^3}{8(1-\phi)^3}$$

$$K \equiv K(L,a) = \left[\frac{\pi}{4}\left(\frac{2a}{L} + \frac{8L}{\pi a} + \frac{7}{2}\right) + \frac{52}{15} + \frac{16}{3\pi}\right]$$

$a$ is platelet diameter and L is the platelet thickness

$$\frac{\mu_{iso}(\phi)}{k_BT} = \frac{\mu_o}{k_BT} + ln\phi + K\frac{3\phi^3 - 9\phi^2 + 8\phi}{8(1-\phi)^3}$$

$$\Delta\mu = \mu_{I-N} - \mu_{iso}(\phi) = \mu_{iso}(\phi_i) - \mu_{iso}(\phi)$$

The self-diffusion coefficient of colloids ($D_s$)[59],

$$D_s = D_o\left(1 - \frac{\phi}{3.7}\right)\left(1 - \frac{\phi}{0.64}\right)$$

where $D_o$ is the diffusion coefficient of an individual platelet which is obtained from [43]

$$D_o = \frac{k_B T}{3\pi\mu L}\frac{\tan^{-1}\sqrt{\xi^{-2} - 1}}{\sqrt{\xi^{-2} - 1}}$$

where $\xi$ is the aspect ratio defined as thickness (L) to diameter ($a$) of the platelet and $\mu$ is the viscosity of the platelet suspension. Nucleation and growth rates are then expressed purely as functions of initial concentration of platelets in metastable states and compared with the experimental observation.

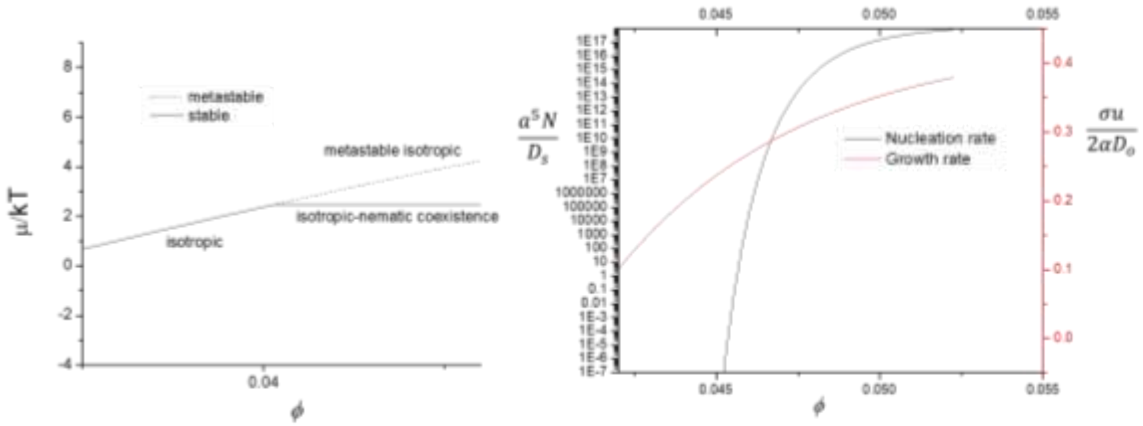

**Figure 12 Chemical potential, nucleation and growth rate of the platelet system simulated for aspect ratio 0.0134 (a) Chemical potential in dotted line corresponds to the metastable isotropic phase that is higher than that for a isotropic-nematic coexistence phase for $\phi > \phi_i = 0.0405$ and hence the system tries to form nematic phase upon going through nucleation and growth of nematic phase. (b) Normalized nucleation (black solid curve) and growth rates (red solid curve) as a function of platelet concentration higher than $\phi_i$.**

## 3.3 Experimental setup

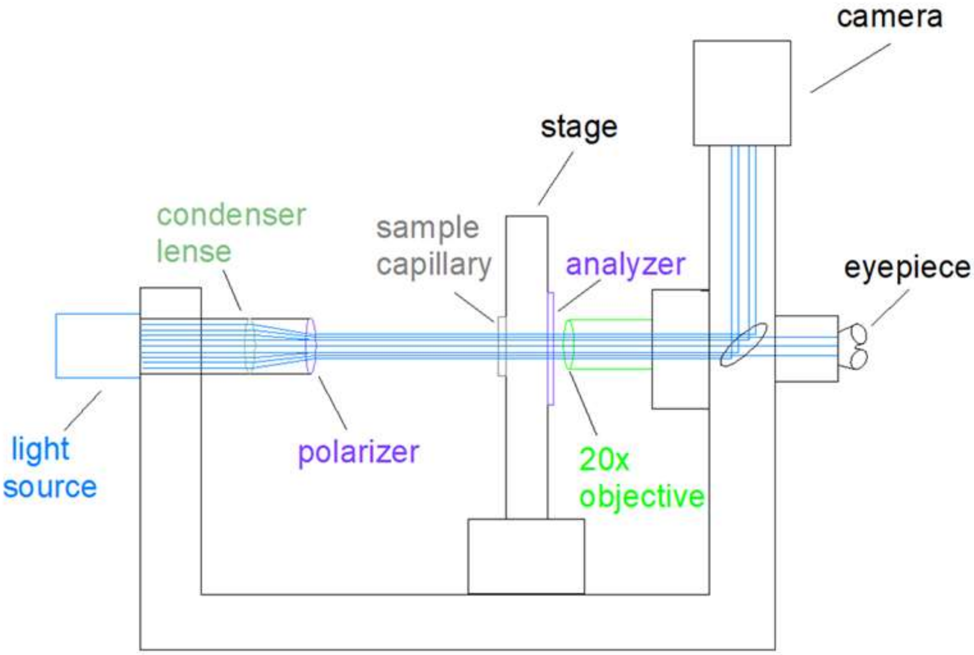

**Figure 13 polarized optical microscopy setup with a modification that allows imaging of a vertically kept sample**

## 3.4 Sample preparation

For this study samples of nanoplates in the I-N coexistence regime of the phase diagram were required. Platelets are synthesized using a reflux method of pristine ZrP synthesis followed by exfoliation using tetra-n-butyl ammonium hydroxide [31]. Sample with different volume fraction of ZrP nanoplates were prepared, homogenized and kept in vertical tubes. Figure 14(a) shows a picture of samples kept between crossed polarizers 10 hours after homogenization. A clear interface between isotropic (appearing dark) and nematic (appearing bright) phase established indicating complete separation of the two phases. The ratio of nematic height to the sample height, $f_N$, was plotted for each sample as a function of initial volume fraction of nanoplates in the corresponding sample as shown in Figure 14(b). Logistic function, $f_N = A_2 + (A_1 - A_2)/(1 + (x/x_0)\text{\^{}}p)$, well represents the data points. The transition of phases upon increasing volume fraction from isotropic (I) to isotropic-nematic (I-N) coexistence takes place at $\phi_\mathrm{i} = 0.0383$ and from I-N coexistence to full nematic (N) at $\phi_\mathrm{N} = 0.0786$. Theoretical calculations for monodisperse, hard platelets of the same thickness and diameter gave $\phi_\mathrm{i} = 0.0405$ and $\phi_\mathrm{N} = 0.0525$. As proven before, dipression of $\phi_\mathrm{i}$ and elevation of $\phi_\mathrm{N}$ as compared to theoretically predicted values [33] was due to polydispersity of the sample which was close to 20%.

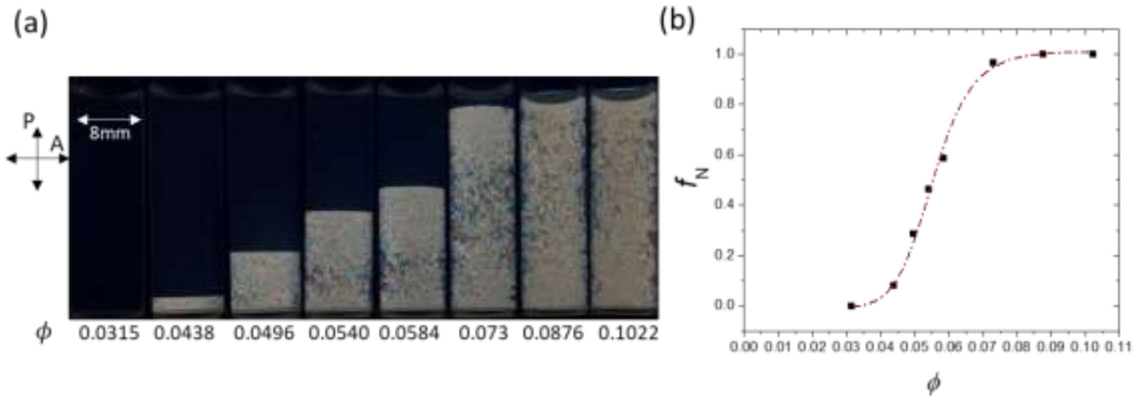

**Figure 14 Phase diagram of aqueous suspensions of ZrP nanoplates. (a) Image of sample tubes kept between crossed polarizers obtained after 10 hours from homogenization of samples. From left to right, the initial volume fraction of nanoplates in tubes increases as 0.0315, 0.0438, 0.0496, 0.0540, 0.073, 0.0876 and 0.1022. The bright part of the tube is nematic and dark is isotropic. Width of tubes is 8mm. (b) Ratio $f_N$ of height of nematic phase to total sample height in each sample tube plotted against the total volume fraction of nanoplates. The data points are fit with logistic function represented in red color**

As reasoned earlier the optics for the experiments needed to have light path in the direction perpendicular to the sedimenting nuclei i.e. along the thickness of the microchannel. Hence the optical microscope was tilted by $90^{o}$ and a capillary channel (50mm x 2mm x 0.2mm) open on both ends was mounted on the stage vertically. A 25X magnification objective lens was used to be able to focus on very small nematic nuclei. The polarizers were crossed and made $\pm 45^{o}$ angles with the vertical direction. The imaging was started at one frame per five seconds upon loading the empty capillaries onto the vertical stage. Suspension of nanoplates were well homogenized using vortex and a small amount was taken out using a micropipette and filled into the capillary. The two ends of the capillary were then sealed using epoxy glue and cured with UV light.

## 3.5 Results and discussion

### *3.5.1 Measurement of nucleation and growth speeds for a single sample*

We first discuss the results in the case of suspension with $\phi = 4.2\%$ which was just above the onset of I-N transition. Polarized optical micrograph obtained at different times are shown in figure 15. The time when the homogenized suspension comes in the field of view is marked as the beginning figure 15(a) at which it appeared nearly dark. Subsequently, tiny bright spots appeared as shown in figure 15 (b). The bright spots are nematic nuclei, also known as called tactoids, surrounded by isotropic phase that appears dark. The tactoids grew larger as more nanoplates from metastable suspension diffused towards the tactoids figure 15 (c-h). Figure 15 (i) shows nematic liquid crystallites at the onset of transition from uniform director distribution which is evident from a tactoid that has dark brushes as identified in dashed yellow box. Lekkerkerker and coworkers studied the shape of small nematic nuclei which changes as the size of the liquid crystallite increases [57]. Figure 15 (j) shows a nearly spherical tactoid, with a defect at the center, in which the director distribution is radial. Small tactoids showed homogenous distribution of nanoplates. At that size, the anchoring energy of the isotropic-nematic interface dominated ($wR^2$) over the splay elastic energy ($K_1R^3$) of the nematic liquid crystal, where w is the anchoring strength and $K_1$ is the splay elastic constant of the nematic phase. But as above $R=K_1/w$, the distribution of nanoplates within the tactoids became non-homogeneous and point defects called hedgehog appeared.

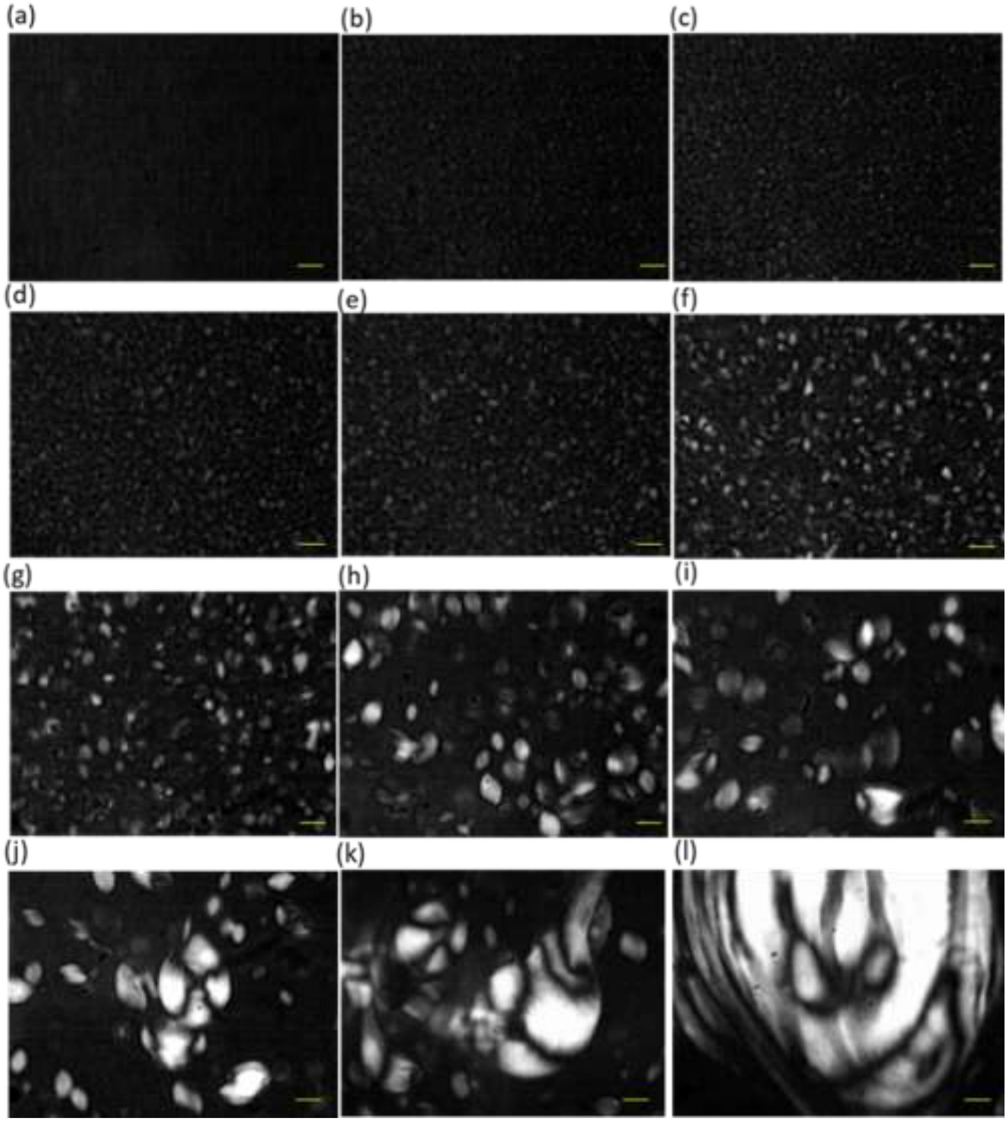

**Figure 15 Polarized optical micrographs (a) initial state shear melt nuclei. A few nematic nuclei known as tactoids observed as tiny bright islands, (b) t=20 s. Subsequently, more tactoids nucleate and grew larger (c) 45 s (d) 340 s (e) 600 s. Further growth of tactoids happened via coarsening observed at (f) 19 min 32s (g) 43 m 4s (h) 1hr16min12s (i) 1hr31min25s (j) 1hr 41min 40s (k) 1hr 53min 10s and (l) 2hr 46min 55s. Scalebar: 25μm**

It is to be noted that with the increase of size, tactoids became brighter as the light rays traversed through a larger path in the liquid crystalline media of tactoids. The intensity of the light coming out of the crossed polarizers is given by, $I = I_o sin^2\left(\frac{\pi\Delta n}{\lambda}x\right)sin^2(2\theta)$, where $I_o$ is the intensity of incoming light, $\Delta n$ is the birefringence of the nematic liquid crystal, $x$ is the length of birefringent medium which in this case is size of tactoids in the direction of light propagation, $\lambda$ is the wavelength of light and $\theta$ is the angle between nematic director and incident polarization. Some of the tactoids that have the director (n) aligned along the polarizer or analyzer i.e. $\theta$=0 appear dark.

To follow the nucleation and growth rate from polarized optical images, pixel analysis was useful. Nematic nuclei could be identified as their intensity was higher than the background which was isotropic. The program for the execution of this technique was developed in software package called Interactive Data Language (IDL 6.0) [61]. For analysis we only considered regime in which the distribution of tactoids was homogeneous as a tactoid with dark brushes was difficult to be identified as one. As shown in figure 16(a), number of nuclei (n) are plotted as a function of time (t). The increase in the number of tactoids up to 400s indicated nucleation regime. Since the time exponent of the fitting function is 1, the nucleation process can be said to qualitatively follow the predictions of classical nucleation theory. After 400s, the number of nuclei remained relatively constant indicating pure growth until about 3300s after which the number decreased due to the coarsening one or more tactoids which was recently studied [62]. The shape of nuclei when they are small as represented by figure 16 (h) is lens shaped. This is analogous to previous studies on tactoids in rod-like and plate-like colloids [57,63]. The ratio of long axis of the ellipsoid to its short axis can be ω = 1.3 [57].

Thus the total area of tactoids identified through pixel analysis can written as, $A = \sum_{i=1}^{n} \pi \left(\frac{L_{tactoid}{}^{2}}{4\omega}\right)$, where the $L_{tactoid}$ represents the average size of tactoids at given time and is equal to the long axis of the oblate ellipsoid. $L_{tactoid}$ continually increased as shown in figure 16(b) and different regimes identified from tactoid count analysis influenced the growth rate. The smallest average tactoid size was ~ 1 µm. The critical size of nucleus predicted by classical nucleation theory is $n_{crit} = 10^3$ (see supplementary information) which means the cluster of about 10000 platelets forming nematic phase would survive and grow continually without melting back into the isotropic phase. This number corresponds to a volume of critical nucleus as, $V_{crit,tactoid} = \frac{n_{crit} V_{platelet}}{\phi_N} = \frac{\pi}{6} \omega^2 L_{tactoid}^3$ , which gives $L_{tactoid}$ ~ 9 µm. Thus, the size of the critical nucleus predicted by classical nucleation theory was at least about one order of magnitude higher than the experimentally observed. In the nucleation regime, tactoids grew with the different time exponents of the growth parameter keeping in mind that some of the nuclei were smaller than the average size of the in the distribution identified from image analysis.

The growth exponent of the tactoids are indicative of nature of the growth of liquid crystallites. If the size of tactoids is proportional to the square root of time, then the growth is diffusion limited and if the growth exponent is 1 then, it is interface limited [54,55]. Tactoids of platelets are found to follow the relation, $L_{tactoid}\ \alpha\ t^{0.44}$ as can be observed from figure 16(b) and thus the growth was diffusion limited as the exponent is close to 0.5. The growth exponent is close to 1 in the coarsening stage which indicates the growth was interface limited. At moderate times (400s-3300s), the growth exponent was 0.36. Such crossover exponents were reported in models for pure atomic systems after the nucleation stage [64] and from classical nucleation theory for cases when the system has low thermal diffusivities [65].

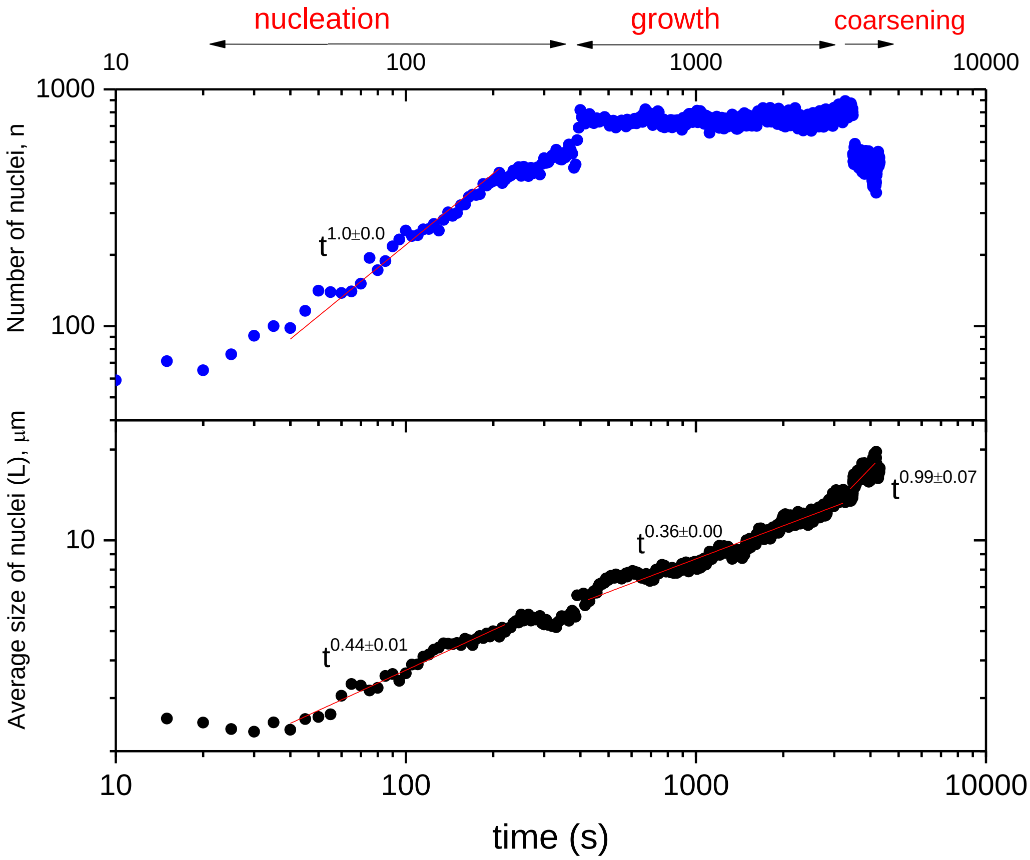

**Figure 16 Nucleation and growth kinetics for $\phi$=0.042 (a) Number of nuclei (n) increase up to 400s in the nucleation regime during which the nuclei also grow. The fit in red line shows $n \alpha t$ which is qualitatively in agreement with the prediction classical nucleation theory. Starting from 400s, the number of nuclei remain constant until about 3300s, after which the number of nuclei decreased due to coarsening with one another. (b) Average size of nematic nuclei (L) increases continually first via a mechanism in which the platelets from isotropic phase become part of the nematic clusters thus increasing the cluster size and later via coarsening mechanism in which two or more nuclei stay together.**

Since the hard platelets considered in this work are purely entropic the heat effects on phase behavior and kinetics are negligible. Besides, colloids are present in very low numbers in a typical sample as compared to atomic systems undergoing phase transition and hence the exchange of energy between colloids and solvent molecules does not have any heat effects. So analogous to low thermal diffusivity (ratio of heat conducted to the heat stored) would be a platelet system with stronger excluded volume interactions. Notably, the growth exponents at longer times ($L_{tactoid}$ α $t^{1}$) in the kinetic process is contrasting to the hard sphere crystal growth ($L_{cryt}$ α $t^{0.1}$ ) in microgravity [56].

### *3.5.2 Effect of nanoplate concentration on the nucleation and growth kinetics*

Similar studies on measurement of kinetics was done on two more samples $\phi$=4.6% and $\phi$=4.8%. The nucleation and growth rates for different concentrations are obtained from slopes of number of nuclei vs time and average size of liquid crystallites vs time respectively. The rates are normalized and compared with the theoretical curves obtained from the theory discussed earlier in this paper. As shown in figure 17, there is a mismatch between theory and experimental data. Absolute predictions using Monte-Carlo simulations on platelets need to be done in future, as were done for spherical colloids [58].

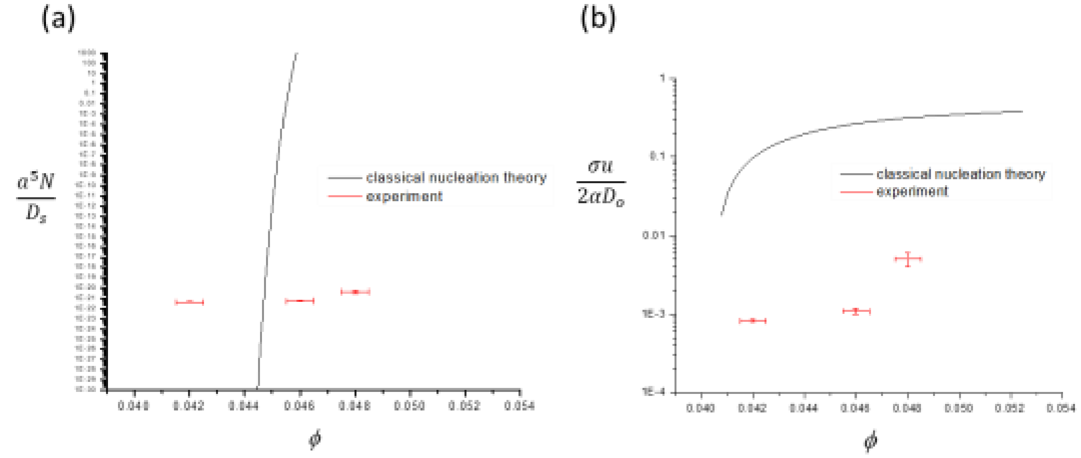

**Figure 17 Comparison of nucleation and growth rates from classical nucleation theory and experiments (a) nucleation speed normalized with platelet size $a$ and diffusion coefficient Ds. The rate of nucleation predicted by theory is several orders of magnitude different than experimentally measured (b) speed of growth of tactoids normalized by diffusion coefficient, effective distance required to travel to become part of nematic cluster (nuclei) from isotropic phase, σ and α is a pre-factor close to unity. Measured growth rate is two-three order of magnitude smaller than that predicted by the theory.**

### *3.5.3 Effect of nanoplate size on I-N separation kinetics in gravity*

It is well established from Onsager's theory of entropic interactions of anisotropic colloids that the smaller the aspect ratio (thickness/diameter) of the particles, the more is the excluded volume of random orientation and the lesser is the concentration required for transition from isotropic to nematic phase[35]. The theory was inspired by the experimental results on behavior of tobacco mosaic virus nanorods and subsequent experiments undoubtedly agreed with the theory[33]. In the general context of colloidal crystallization, the effect of shape and size of anisotropic colloids on the kinetics is intriguing topic to investigate. The kinetics of liquid crystal growth is governed by the diffusion of colloids to the growing interface as shown in the previous section of this chapter. Owing to slower translational diffusion rates, nanoplates with with very low aspect ratio, the kinetics can be very slow. Through a series of macroscopic observations of colloidal samples undergoing isotopic nematic phase transition in gravity, the effect of aspect ratio of nanoplates on the kinetics of phase transition was studied. Figure 18 shows a sample container containing nanoplates of aspect ratio 0.0059 (average nanoplate size of 454 nm) at volume fraction, $\phi$ = 2.8%. Initially (i.e., t = 0), the suspension was homogenized by gentle hand shaking and turning the vial upside down while making sure that no air bubble is trapped inside the suspension. Tactoids (nematic liquid crystal droplets surrounded by isotropic phase) nucleated, grew larger with time and sedimented subsequently as outlined with different boxes in figure 8. After the nematic tactoids settled to the bottom of the container, a clear interface between the isotropic and nematic phase was established. The time elapsed between homogenization of the sample and the establishment of a clear interface between I and N phase, is defined as the time required for I-N separation (t*). Upon monitoring t* for nanoplate samples with different aspect ratios but having the same amount of nematic fraction at equilibrium, effect of nanoplate shape anisotropy on the speed of I-N phase transition kinetics was studied.

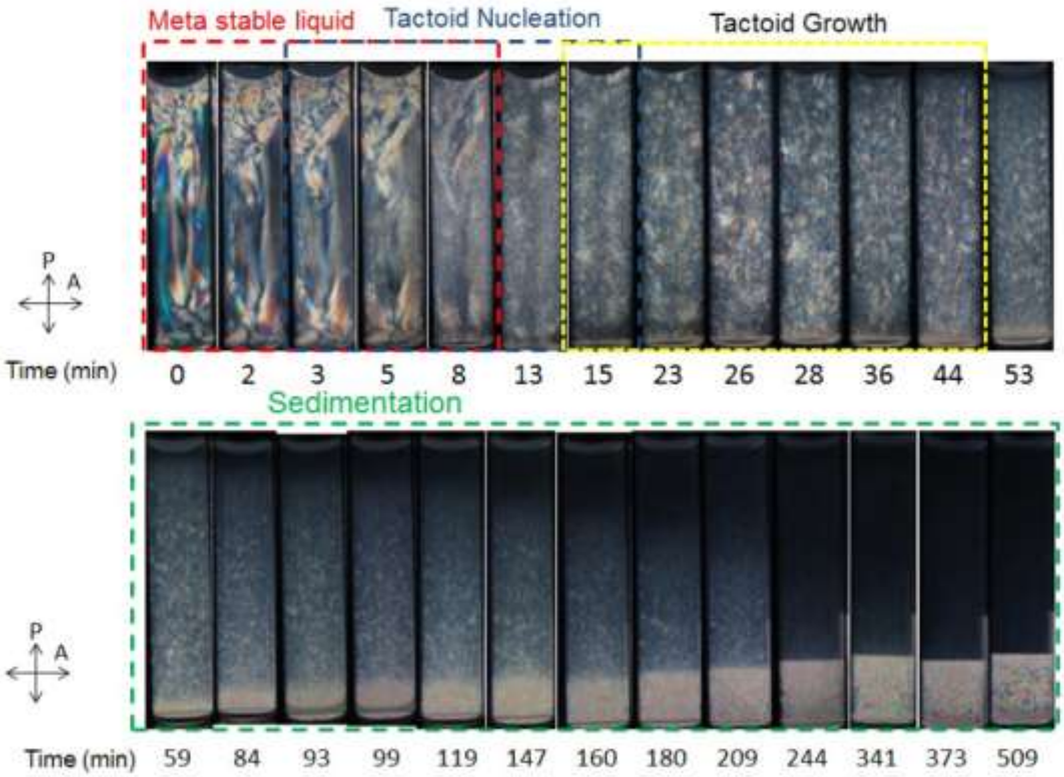

**Figure 18 Snapshots of a group 1 nanoplate suspension (ξ = 0.0059) between crossed polarizers with a ZrP platelet volume fraction, ϕ = 1.75%, taken as a function of time. In the beginning, the suspension was in a metastable liquid state and then underwent the nucleation and growth of tactoids, followed by tactoid sedimentation, which was completed at time, t*, when a clear interface between isotropic and nematic phases had established. This figure was adapted from reference [42] with permission.**

Grayscale values of all pixels in the image were obtained using IDL 6.2 image analysis software. The ratio of intensity (I) of the light transmitted through sample and crossed polarizers to the intensity ($I_0$) of light input to the polarizer was measured by standard charge-coupled device (CCD) relation, $\frac{I}{I_o} = \left(\frac{GrayScaleValue}{255}\right)^{2.4}$. The transmittance values along a vertical line at the center of vials shown in figure 18 were analyzed from bottom to the top as a function of time, as shown in figure 19(a). A sharp decrease in transmittance profile at time 341min and 509 min was indicative of the formation of interface between isotropic and nematic phase. The area under this transmission curve for values of height above the I-N interface height represented the amount of unsettled tactoids, which decreased first (trend 1) and remains relatively constant (trend 2) at a value close to zero as shown in figure 19(b). The value of t* is determined by the intersection of the two trends as demonstrated. Similar analyses were done for suspensions of nanoplates having different aspect ratios of nanoplates. The suspensions with an average platelet size of 454 nm (aspect ratio 0.0059) took less than 10 hours to complete I-N separation. As the platelet size increased, the required time for I-N separation also increased. Suspensions of nanoplates with an average platelet size of 1356 nm (aspect ratio of 0.0029), it took about 100 hours. The dependence of t* on aspect ratio is plotted in figure 19(c). The details of the polarized optical images of other samples can be found in the published article based on this subsection of this dissertation [42].

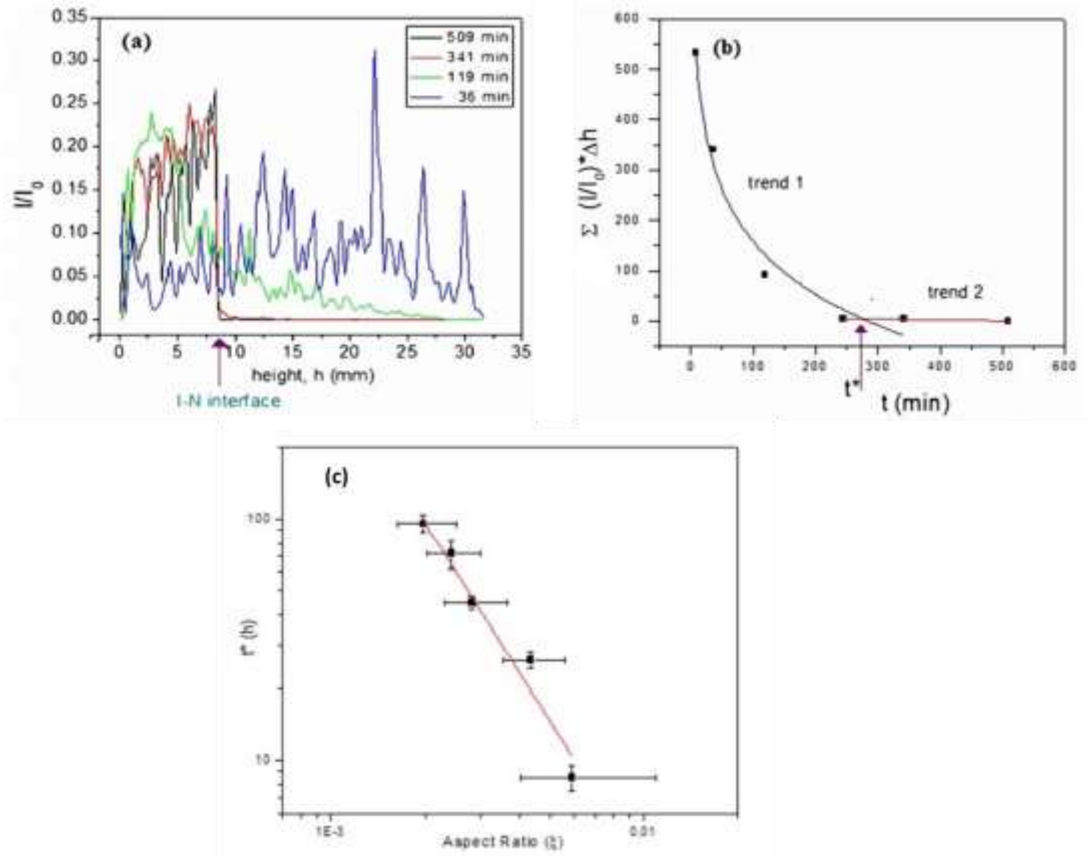

**Figure 19 (a) Transmittance profiles along vertical line in group 1 suspension with I/Io plotted at different times. Position of I-N interface is pointed with an arrow. The transmittance profile shows a sudden jump at 341 min, indicating the establishment of I-N interface. (b) Area under the transmittance curve in (a) for the region above the I-N interface was plotted as a function of time. Time t* corresponds to the point where area becomes zero (c) Dependence of equilibrium time (t*) on the aspect ratio of nanoplates. This figure was adapted from reference [42] with permission.**

From figure 19(c) the equilibrium time required for formation of nematic phase varied with the aspect ratio as $t* = \alpha <\xi>^n$, where $\alpha$ = 0.97 ± 1.30 s and $n = -2.1 \pm 0.2$. The I-N phase separation time was affected by nucleation rate of tactoids, as well as by the sedimentation speed of the tactoids. It was fair to assume that the tactoid sedimentation rates were nearly the same as it depended only on the size of tactoids and the tactoid volume fraction based on previous studies on colloidal sedimentation[66]. By choosing samples of different size of nanoplates with same nematic fraction, the sedimentation can be assumed to be taking the same amount of time in the kinetic process of isotropic-nematic interface formation in all the suspensions of four different nanoplate sizes. Thus, the nucleation and growth time of the tactoids remains critical for the determination of t*. It is argued here that the nucleation rate of smaller size nanoplates (larger aspect ratio) was much faster and hence their I-N separation time was smaller compared to that of larger nanoplates (smaller aspect ratio) owing to their faster diffusion coefficient $D \sim \frac{3k_BT}{8\eta L}\xi^2$, where L is the thickness of nanoplates (same for all four aspect ratios used in this experiment) and $\xi$ is the aspect ratio. It is to be noted that the effect of volume fraction of nanoplates on their diffusion can be considered as not very significant as the volume fractions of nanoplates are as low as 3%.

## 3.6 Conclusion

Kinetics of isotropic to nematic phase transition in colloidal platelets qualitatively follows classical nucleation theory and the growth is diffusion limited in nucleation stage and interface limited at longer times. The rates of nucleation are several orders of magnitude smaller than those predicted from theory. The nanoplate size is found to affect the time required (t*) to form the I-N interface under gravity, as $t^* = a < \xi >^n$, where $a$ = 0.97±1.0 and n = -2.1±0.2.

# CHAPTER IV

# ELECTRIC FIELD CONTROL ON LIQUID CRYSTAL PHASES OF NANOPLATES

## 4.1 Abstract

Control of nanoparticle orientations using external stimuli is important for the design of electrooptic functional materials. From fundamental standpoint, novel assemblies of nanoscale mesogens can be obtained by external field. Nanoplate guest in liquid host type of systems show liquid crystalline nematic phase however a neat topologically clear understanding of these new generation 2D nanosuspensions was missing because their surface anchoring cannot be controlled. We used external electric field to control nanoplate orientations and obtained a hybrid aligned liquid crystal cell of nanoplates with homeotropic anchoring at the surface thanks to wetting of nanoplates and planar alignment in the bulk due to e-field. In this so-called hybrid alignment, cores of point defects were much smaller and the nematic brushes were sharper than unaligned state. A very interesting rotation of brushes around the defect cores with equal probability of clockwise and counterclockwise was indicative of chiral symmetry breaking. Subsequently, integral topological defects (±1) split into semi-integral (±1/2) defects minimized the frank free energy of elastic deformations. Negative inter defects which have a combination of splay and bend split before the positive ones which had pure splay indicating higher stability of splay elastic deformations in nanoplate liquid crystals. Semi-integral defects with opposite charge showed annihilation following the classical model. Final structure of the LC was periodic, like the one observed in hybrid

aligned molecular liquid crystals. Very interesting formation of spikes on the nematic brushes were formed due to flowing free ions in electric field.

## 4.2 Introduction

The electric polarizability of the nanoplate is different in plane of nanoplate and in the direction perpendicular to the plane of nanoplate and the difference between the two is called the anisotropy of polarizability, $\Delta\alpha = \alpha_{\|} - \alpha_{\perp} < 0$ (see figure 20(a)). Thus the nanoplate normals, ***n***, align perpendicular to an external electric field to minimize the free energy as per eq. (). This configuration has degeneracy such that ***n*** can be along any of the directions in the plane perpendicular to **E**. Figure 20(b) shows the phase diagram of systems with $\Delta\alpha < 0$ in presence of external field [70].

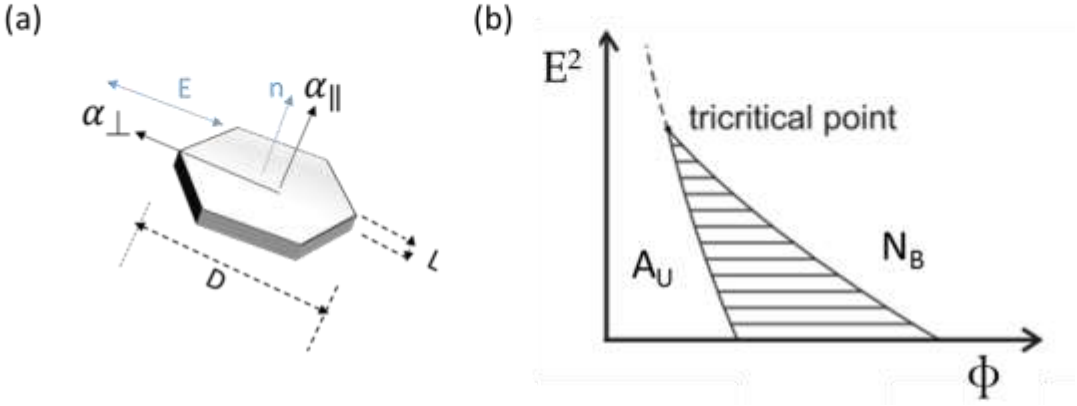

**Figure 20 External field effect on phases of negative dielectric anisotropy and (a) Nanoplate normal, n, aligns perpendicular to E due to negative Δα (b) Upon application of electric field, at low volume fraction of nanoplates, $\phi$, uniaxial anti-nematic phase ($A_U$) was predicted and had been experimentally proven[67,68] whereas at high concentration, biaxial nematic phase ($N_B$) is predicted[69] but has not yet been proven experimentally. Part (b) was adapted from reference [70] with permission.**

It was thus exciting to investigate the effect of external electric field on phase diagram of nanoplates- especially verify the hypothesis if the cylindrical symmetry of the uniaxial nematic phase of nanoplates can be broken by electric field to form a biaxial nematic phase. Biaxial nematic phase is spontaneously formed in board-like colloidal particles[71] that have a specific ratio of their length to width to thickness ratio.

## 4.3 Results and discussion

### *4.3.1 Isotropic to antinematic phase transition induced by E-field*

Isotropic suspensions in presence of external electric field form a birefringent phase, also known as the anti-nematic phase[72]. Figure 21(a) shows the isotropic sample of ZrP nanoplates kept in a Kerr cell that consisted of two copper electrodes separated by 2mm and had an optical path length (perpendicular to the plane of this page) of 10mm. Applying a high frequency AC field, sample became birefringent as shown in figure 21(b). The normals of the nanoplate aligned perpendicular to the direction of the electric field. Small bubbles were formed at low frequency (<1kHz) and hence high frequency ~ 500kHz was chosen to avoid bubble formation. Dominating mechanism for the response of nanoplates to external electric field is the Maxwell-Wagner-O’Konski induced polarization.[14]

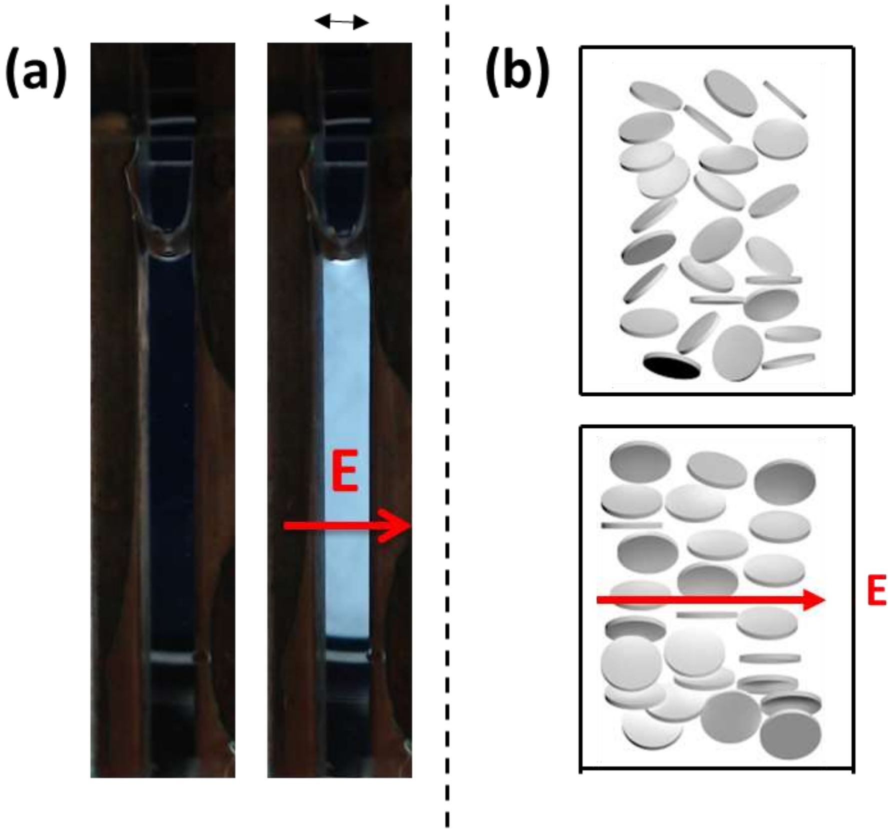

**Figure 21 (a) isotropic phase (left) turns birefringent upon application of E field. (b) Schematic of nanoplate orientations in isotropic phase (top) which in presence of external e-field becomes antinematic (bottom) phase. It is coined anti because the director n is perpendicular to the field.**

### *4.3.2 Uniaxial nematic to biaxial nematic phase transition induced by E-field*

Varga et. al.[69] in year 2000, claimed that for particles with negative anisotropy of dielectric polarizability $\Delta\alpha < 0$, electric field induces biaxiality if the number density of the particles is more than 2.5 i.e. for $c = \left(\frac{\pi}{4}\right)^2 \frac{a^3 N}{V} = \frac{\pi}{4}\frac{a}{L}\phi > 2.5$, for $a$ =300nm and L= 2.68nm, it becomes $\phi = 2.8\%$. When electric field was applied to a nematic sample using two ITO coated glass substrates, the textures under crossed polarized optical microscope were observed as shown in figure 22. A full nematic sample was loaded in the liquid crystal cell. After 65 minutes of tactoids nucleation and growth, the texture showed four brushed defects within tactoids figure 22(a). The area surrounding the tactoids was dark and indicated presence of metastable liquid. Upon application of electric field, a well-aligned nematic phase was observed in which nanoplates aligned with their planes perpendicular to the glass substrates within a minute- figure 22(b)**.** As a result, sharp ±1 defect appeared at the center of tactoids and the metastable region also showed nucleation and growth resulting into nematic texture with more number of defects as can be seen at the bottom of figure 22(b-c). Interestingly, with the passage of time, rotation of the four brushes around their defect centers and simultaneous displacement of ±1 defect position was observed as shown in figure 22(d). Four brush defects further split into two brush defects- as the blue box can be followed in figure 22(d-e)**.** All the four brush defects (outlined with white dotted square) in figure 22(e) subsequently split into two brush defects as shown in figure 22(f). Such splitting of ±1 defects into ±1/2 defects is actually a characteristic of biaxial nematic phase according to several reports.[73] When the electric-field was turned off, the two brush defects became sharper (figure 22(g)) and later disappeared via annihilation process of the type +1/2-1/2=0. After a few hours, completely dark texture was observed due to alignment of nanoplates shown in figure 22(h) when nanoplates aligned with faces parallel to substrate thus making optical axis along the direction of light giving no birefringence.

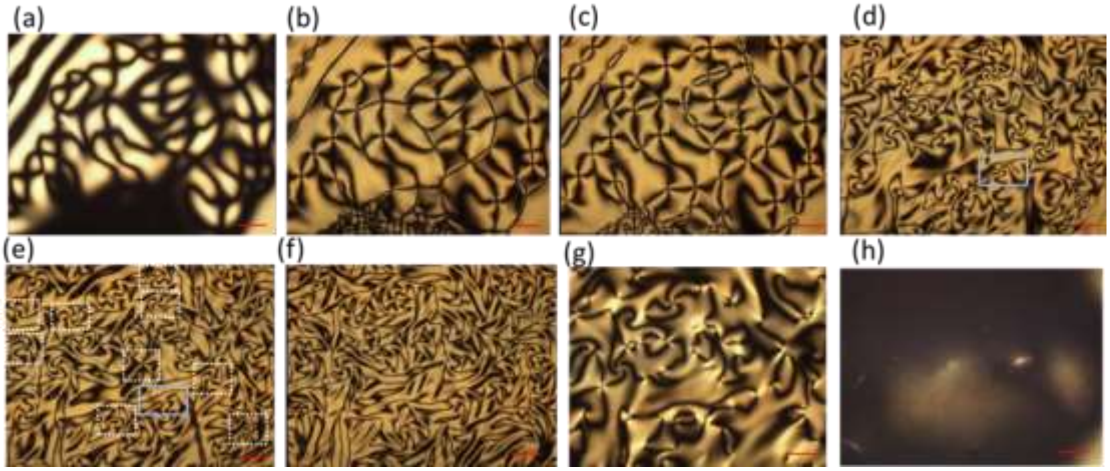

**Figure 22 POM images of ϕ~4% (nematic, ξ ~0.01) sample sandwiched between ITO glass plates with separation of 120μm without E-field (a) and with E-field (100V/mm, 500kHz) after 1 min (b), 4min (c), 40min (d), 68 min (e), 218 min (f); Images (g) 45 min and (h) 18h after turning off the E-field. The scale bar indicates 200μm. E-field points in the direction out of the image plane.**

The topological defects in the nanoplate suspensions and their dynamics under the application of electric field needed mapping of the director field (***n***). LC Polscope was used for this purpose which makes use of the birefringence of the sample to map the director field. The director field of the sample without electric field (figure 23(a)) is shown studied using PolScope as shown in figure 23(c). Topological defects in liquid crystals had no optical birefringence and hence appeared dark. If the director field around point defect was radial, as discussed in figure 2(a), the charge of the topological defect was be identified as "+1", and if it was hyperbolic as shown in figure 2(b), the charge was "-1". The charges of the defects thus identified were labelled on the polarized optical micrographs (figure 23(a)) with the help of LC PolScope studies. As shown in the schematic in figure 23(b), the nanoplate orientations around the core of the defect were radial in three dimensions. The defect core is shown to be isotropic with random orientations of nanoplates. The sample was in I-N coexisting region and hence the some part of the sample that appeared dark in figure 23(a,c) were isotropic. Upon applying the electric field, defect cores became really small figure 23(d,f). The orientations of nanoplates in the field aligned state are shown schematically in figure 23(e).

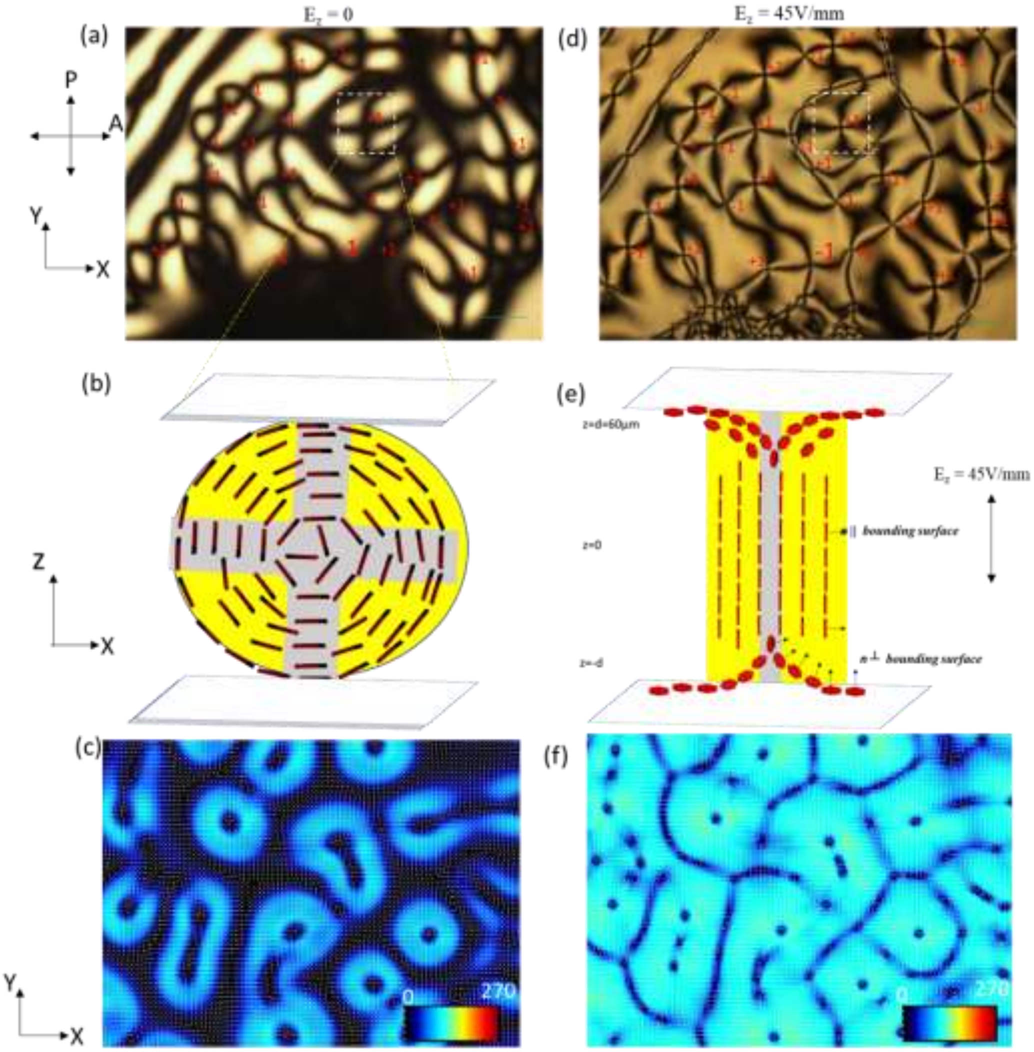

**Figure 23 (a) A nematic phase of nanoplates at ϕ=5.5% with hedgehogs of strength +1 were found at the center of nematic domains that formed via nucleation and growth and hedgehogs of strength -1 at the boundary of the two nematic domains (b) Sketch of nanoplates in the nematic domain outlined with white dotted square in part (a) as observed from the side (XZ) plane (c) Polscope image showing retardance of the sample on a scale of 0 to 240. Isotropic part of the sample, prepared separately, appears dark. The cores of defects are about 40µm in size. (d) POM of the quasi-planar structure formed upon applying E-field in Z direction. (e)nanoplate orientation in hybrid alignment: homeotropic at the walls and planar in bulk (f)Birefringence of the sample increased due to field induced alignment and nematic phase nucleated in dark isotropic regions; the core shrank to about 10µm. Scalebar shows 200µm.**

### *4.3.3 Dynamics of defect annihilation*

The director field under the presence of electric field was tracked using LC PolScope and topological defect annihilation in nematic suspensions of nanoplates was studied. Figure 24 shows snapshots of the defect annihilation process obtained using LC PolScope.

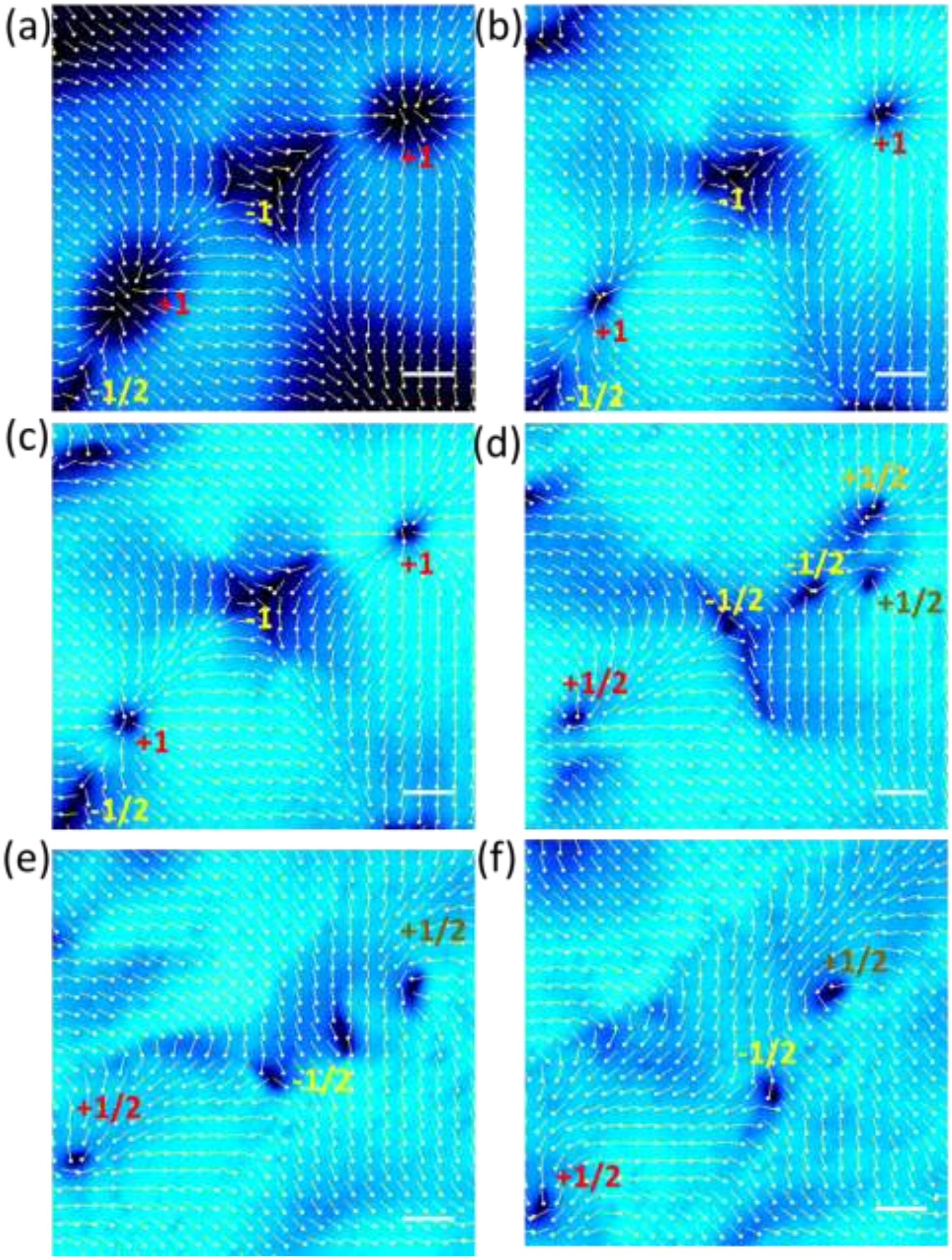

**Figure 24 Director field mapping using Polscope imaging of the nematic phase under e-field showing m = +1 defects split into m = +½ and m=-1 defects split into two -1/2s. (a) 0 min only integer defects are observed (b)1min after application of e-field the defect cores get smaller as nanoplates were aligned with by the field and only integer defects were still observed (c) 3min after a -1/ 2 defect was seen indicating the -1 defect had started to split but +1 defects remained (d) 5min after e-field application where only ± ½ defects are observed; pairwise annihilation subsequently shown in (e) 7min and (f) 9min.**

The number of +1/2 and -1/2 defects were measured as a function of time and plotted on log-log scale as shown in figure 25. Using the scaling laws[74], the LC domain size (ς) is proportional to the inverse square root of the topological defect density (ρ) given by $\varsigma \ \alpha \ \rho^{-1/2}$. From the fit shown in figure 25, it can be concluded that the nematic domain size (ς) has a time exponent of 0.58±0.07 which is close to 0.5 indicating the diffusion-controlled growth. The time exponent also indicated that the defect annihilation took place via formation of pairs of oppositely charged defects called dipoles. In other systems such as patterns of polymer films, the defect annihilation showed a time exponent of 0.25 indicating formation of quadrupoles which is formation of two pairs of oppositely charged defects[74].

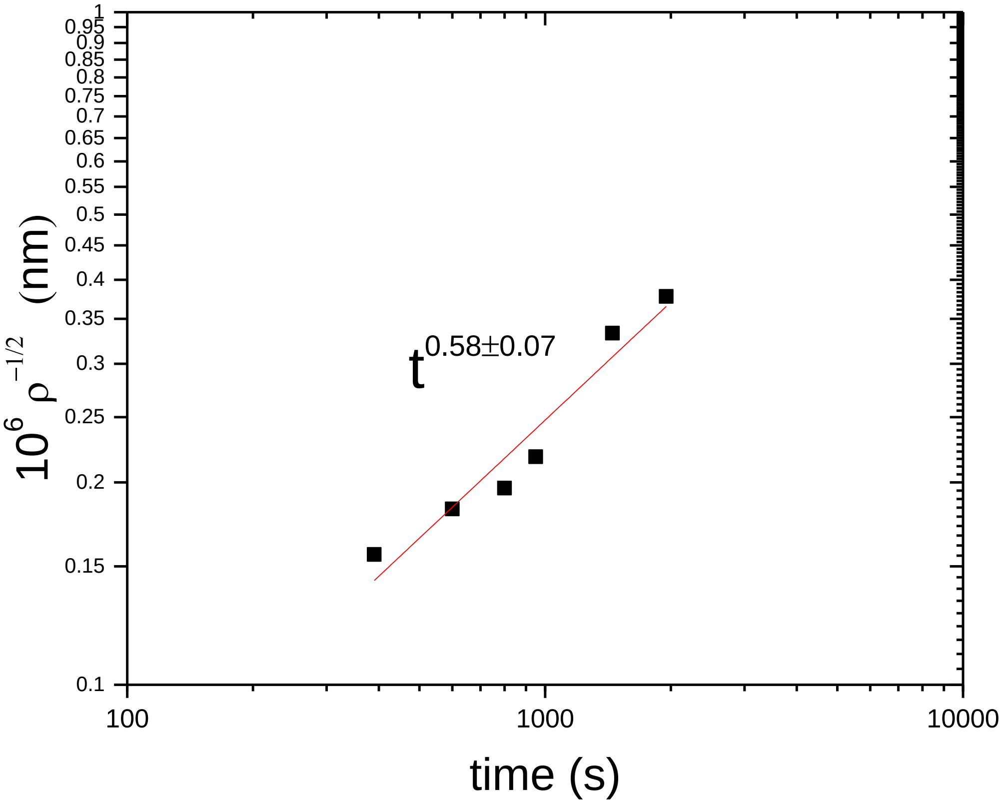

**Figure 25 Time exponent 0.58 is close to 0.5 indicating diffusion limited kinetics of defect annihilation in which dipoles of oppositely charged half defects are formed**

## 4.4 Conclusion

A positive evidence for electric field stabilized biaxial nematic phase was found in nematic suspensions of nanoplates through the splitting of ±1 defect into ±1/2. Dipoles of ±1/2 defects formed during annihilation process.

# CHAPTER V

# THERMOPHORETICALLY CONTROLLED FORMATION OF NEMATIC LIQUID CRYSTALS OF NANOPLATES

## 5.1 Abstract

Dynamically controlled self-assembly of colloidal nanoparticles by using external stimuli has been an active field of research owing to their fundamental significance as well as their emerging applications in advanced functional materials. Among other methods, thermophoresis of nano-colloids is important, and it has been proven to be useful in plethora of applications including sensors, reactors, particle-separators. Of the many studies, those involving non-spherical anisotropic nanoparticles, such as plate-like or rod-like geometries that exhibit different phase behavior from spheres, have never been explored. We studied thermophoretic effects in aqueous suspensions of highly anisotropic colloidal disks also known as nanoplates. Thermophoresis of nanoplates, over a timescale of a few hours, resulted in an isotropic to liquid crystalline nematic phase transition. Soret coefficient ($S_T$) of nanoplates was measured thanks to the ability of nanoplates to form birefringent nematic liquid crystalline phase. The interface between isotropic and nematic phases was linear with a small angle of inclination decided by gravity sedimentation and thermophoretic fluxes. To the best of our knowledge, this is the very first report of thermophoretically controlled growth of soft continuous structures - nematic liquid crystal in this case. Our

findings can be useful for applications where nanoplates can serve as efficient, thermos-selective cargos for transport of biomolecules.

## 5.2 Introduction

Colloids are particles of one substance suspended throughout another substance. Novel methods to dynamically control self-assembly of nanoscale colloids can be realized by using external fields [75], which could find promising applications in diverse areas such as controlled growth of crystals [50], fabrication of electronic displays [76] and tuning of structural colors [15,77]. In this context, finding ways to control the density of colloids that determines their phase behaviors and the growth of one phase from another is important. A thermal gradient can selectively drive nano-colloids to create such density gradients. Fundamentally, applied temperature gradient leads to a colloidal density gradient due to Soret effect or thermodiffusion [78], which in early times was studied for isotope separation [79], nuclear fusion in ionized gas [80]. When the solute undergoing a drift due to temperature gradient is a macromolecule, its motion is usually referred as thermophoresis. Thermophoresis has found many applications in colloidal dispersions such as separation techniques [81-84], optothermal trapping [85] and controlled growth of single crystals[50]. While other techniques such as dielectrophoresis and electrophoresis are limited by electrode polarization and joule heating, respectively, temperature gradient can prove to be advantageous in directing colloids selectively toward the warm or the cold and thus controlling their self-assemblies.

Thermophoresis is a nonequilibrium cross-flow effect between mass and heat transport. When a colloidal suspension is placed in a temperature gradient, the dispersed particles experience a net flux given by [86], $J = -\rho c(1-c)D_T\nabla T + \rho D\nabla c \quad \dots(1)$, where $\rho$ is the density of fluid, c is the particle concentration in weight fraction, $D_T$ is the thermophoretic mobility and T is the temperature. Thermal inhomogeneities inside the thin layer of fluid in contact with solid particle is responsible for thermophoresis in one of the widely accepted mechanism proposed by Ruckenstein [87]. The gradient of the solid-liquid interfacial tension parallel to $\nabla T$ creates an anisotropic pressure tensor near the particle's surface due to which the particle is pulled towards the direction of lower surface tension free energies [88]. Thermal response of the electrolyte plays a major role in the transport of charged colloids such that a change in the salt concentration could cause inversion of thermophoretic mobility ($D_T$) of charged colloids [89] because the difference in thermophoretic mobilities of positive and negatively charged ions in solvent could lead to separation of charges in presence of thermal gradient and the resultant thermoelectric potential could have an added effect on the charged colloidal particles' motion and depending on the sign of charge on colloids, they drift to the cold or to the warm [90]. The thermophoretic mobilities of individual ions in an electrolyte are determined by their solvation forces and concentration [91].

Physico-chemical properties of charged colloids affect their Soret coefficient- for example, in charged micelles, Soret coefficient decreased with the increase of solution ionic strength and scaled as the square of Debye-Huckel length [92]. The sign of Soret coefficient was found to be negative in macromolecular systems such as polypeptides [93], proteins in aqueous media. As will be shown in this paper, in the temperature range of 30°C to 40°C, colloidal nanoplates of Zirconium Phosphates, show negative Soret coefficient. Since the solvation forces are dependent on temperature, many colloidal and biological systems show negative Soret coefficient at low temperatures typically referred to as a critical temperature T* that is highly dependent on the system. In polystyrene latex spheres, T* was near about 4°C whereas in micellar solutions of non-ionic surfactant dodecyl maltoside (DM), it was close to 43°C [93]. Thermophoretic mobility ($D_T$) of colloids was measured for polystyrene spheres and was found to be independent of the size of colloids [94] whereas the Soret coefficient was found to be proportional to particle surface area [95].

Thermophoretic studies in colloidal suspensions have been so far limited to spherical colloids. The increased surface to volume ratio in anisotropic nanoparticles poses plenty of advantages such as higher loading of the cargo for a given volume of colloids. From a fundamental standpoint, one of the novelties of non-spherical nanoparticles is their ability to form unique soft continuous structures such as nematic, smectic liquid crystals at higher concentrations [5,37,42,96]. It is therefore possible to thermophoretically control the growth of novel soft continuous phases of platelets, rods and board-like particles. Due to the slow, nearly epitaxial growth, topological defect structures of external field-driven phases can be significantly different from those formed spontaneously at different regime of the phase diagram. Herein, we demonstrate thermophoretic control on the nanoplate concentration by applying a linear temperature gradient to a nanoplate suspension in isotropic phase which in few hours leads to formation of nematic phase via crowding of nanoplates at the warm end. We thus establish a control on growth of soft continuous structures, in this case, a nematic liquid crystal, using external temperature gradient. Nematic liquid crystal is a well-defined soft matter system with a rich variety of supramolecular structures [7]. An increasing fraction of nematic liquid crystals towards the warmer region was indicative of positive density gradient towards the warm region. Based on the optical birefringence, the density profile was measured and Soret coefficient ($S_T$) of plate-like nano-colloids was measured for first time. Our study paves a way for 2D materials based microfluidic applications such as thermos-selective nanoscale transporters as well as for the design of functional materials.

## 5.3 Experimental setup of temperature gradient

Experimental methods to study thermophoresis of colloids in aqueous and non-aqueous suspensions are quite diverse. Thermal field flow fractionation (ThFFF) [81,82], beam deflection [79,80,83], holographic scattering [79,86,95], thermal lensing [87], and optical heating in microfluidics [88,89] are some of the common methods. A flow system was not desired in this study as the nucleation and growth of phase was to happen slowly and the sample confined between boundaries was to always remain the same. Besides, thermal gradient over a relatively large distance (few centimeters) was desired to facilitate the study of growing soft continuous structure and a slow enough thermophoretic flux could lead to epitaxial growth in absence of convection.

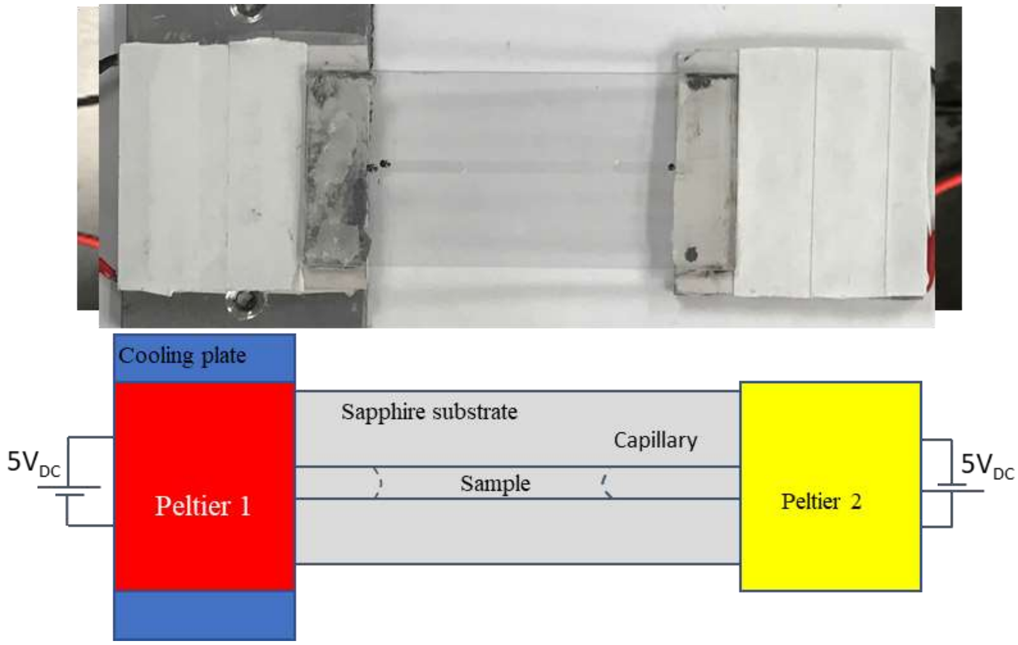

**Figure 26 Sapphire crystal kept in touch with Peltier thermoelectric devices to create a thermal gradient across the sapphire substrate (top) and the schematic of the same (bottom)**

The thermal gradient was created using the setup shown in figure 26. The polarized optical imaging setup to study the thermophoresis in colloidal nanoplate suspensions consisted of a LED light source, a polarizer, a transparent temperature gradient substrate holding the sample capillary, a second polarizer (perpendicularly oriented to the first one) called analyzer and a USB camera which is not shown in the figure. To provide temperature gradient over a relatively longer distance (few centimeters) a heat conductive material could serve as a substrate and for polarized optical microscopy, it needed to be transparent. A sapphire single crystal plate (Miller Optics, USA) having thermal conductivity of 23 W/mK was a suitable option. The two ends of the substrate were kept in touch with thermoelectric Peltier heating/cooling devices. Suspensions of ZrP was filled in flat rectangular capillary (Vitrocomm, NJ, USA) having dimensions 50mm x 2mm x 0.2mm and its two ends were sealed using UV-curing glue. Thermal paste was used to hold the capillary on the Sapphire plate thus making good thermal contact.

A Peltier device has two surfaces of which one got heated and the other one cooled when connected to a voltage source. By reversing the polarity of the external voltage, the behavior of hot and cold surfaces can be interchanged. If an appropriate heat sink is not provided to the hot surface, the device stops functioning. In this experimental setup, thermoelectric device on the left had its hot surface touching the Sapphire plate which conducted to the other end and worked as a heat sink. The thermoelectric device on the right (named as Peltier cooler in the block diagram), had its cold surface touching the Sapphire plate and the hence the heated surface needed an external heat sink. It was kept in touch with an 8mm thick metallic plate which was maintained at ~5$^{O}$C using a cooling fan. The temperature variation of the sapphire substrate is shown in figure 27.

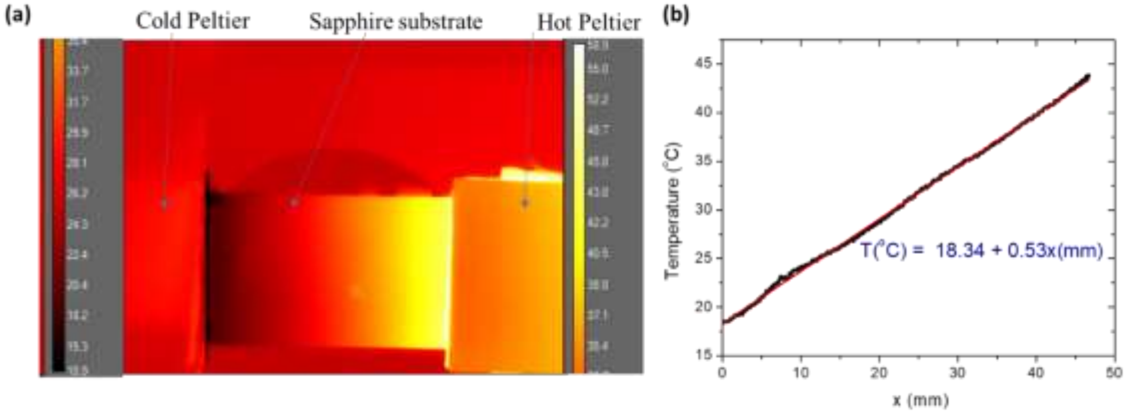

**Figure 27 (a) Temperature gradient across the sapphire plate (substrate) captured using FLIR Camera. The sample capillary is mounted horizontally on the substrate. (b) Linear variation of temperature of sapphire substrate with the distance from the cool end, given by T($^{o}$C)=18.34+ 0.53 x(mm)**

## 5.4 Sample preparation

Zirconium phosphate nanoplates at concentration ($\phi_o$ = 3.19%), which was less than the isotropic to isotropic-nematic coexisting region transition volume fraction ($\phi_I$ = 3.5%), was used in this experiment. Aqueous suspensions of highly anisotropic plate-like nanoparticles, also known as nanoplates, of zirconium phosphate (ZrP) were synthesized (please see materials section). Figure 28(a) shows TEM image of ZrP nanoplate. The size distribution of ZrP nanoplates was measured via dynamic light scattering (DLS) as shown in figure 28(b). The mean size and polydispersity of nanoplates were 262nm and 18% respectively. With the increase of volume fraction of ZrP nanoplates, the aqueous suspensions showed phase transition from isotropic liquid to nematic liquid crystal as shown in figure 28(c). Due to the inability to change the polarization direction of incident polarized light, isotropic liquid samples appear dark between crossed polars. Whereas nematic liquid crystalline phase due to the orientational order of nanoplates, could change the polarization state and thus appeared bright. The ratio of the height of the nematic phase to the total sample height gives the ratio of nematic phase to the sum of isotropic and nematic phases. Based on the equilibrium time reported earlier for the phase separation [42], the phase diagram was set as shown in figure 28(d).

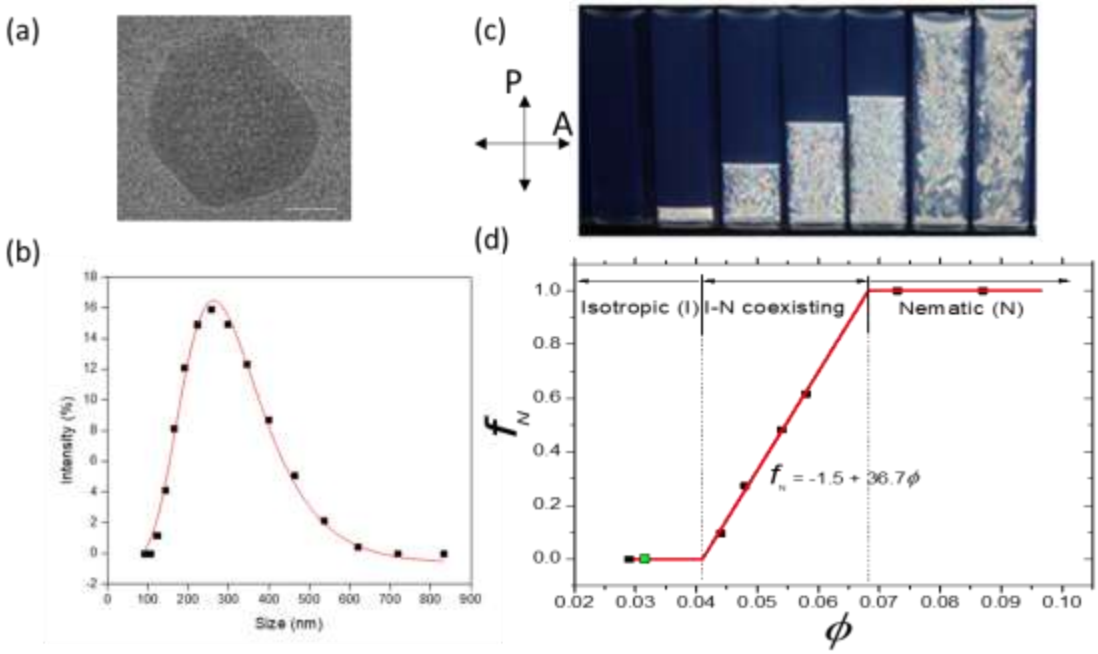

**Figure 28 (a) TEM image of ZrP nanoplates (b) Size distribution of nanoplates obtained through DLS followed by conversion of hydrodynamic diameter to the platelet diameter (c) Images of aqueous suspensions of ZrP nanoplates kept between crossed polarizers. Volume fraction of nanoplates from left to right is 0.029, 0.044, 0.048, 0.054, 0.058, 0.073 and 0.087. The nematic liquid crystal appeared bright and had settled down due to gravity after 6 hours. The cylindrical vials were 8mm in diameter. (d) Phase diagram of isotropic-nematic phase transition in ZrP nanoplates showing the ratio of nematic phase to the sum of isotropic and nematic phases plotted against the volume fraction of nanoplates. The transition from isotropic to coexisting phase happened at $\phi_{ZrP} = 0.035\pm0.002$ and from coexisting to full nematic phase at $\phi_{ZrP} = 0.075\pm0.002$ at which the percentages of nematic phase in the sample were 1% and 99% respectively. Green dot represents the concentration of the isotropic sample used in this study.**

## 5.5 Results and discussion

A uniform suspension of colloids kept in a thermal gradient thus only shows thermophoretic flux in the beginning and later mass diffusion flux develops to counter the thermophoresis. At steady state, concentration gradient develops profile which is given by, $\nabla c = S_T\big(c.(1-c)\big)^{-1}\nabla T \ldots (2)$, where $S_T = D_T/D$, is the Soret coefficient. Depending on the sign of $S_T$, the direction of thermophoretic drift velocity $v_T = -DS_T\nabla T$ changes and particles accumulate either to the cold or the warm. The magnitude of the force on particles [97] can be given by $F_{th} = -Al\gamma'(T)\nabla T$ where A is dimensionless constant, $l$ is the characteristic length scale of the internal region, $\gamma'(T)$ is the rate of change of fluid-particle interfacial tension with temperature. This force is balanced by frictional force offered by the surrounding fluid; as a result, there is only a net flux of particles either along or opposite to the direction of thermal gradient given by $j_{th}$. It is important to note that due to flat shape, 2D nano-colloids can have a larger component of the interfacial tension force as compared to spherical counterpart. Of course, the nanoplates will have to have their planes parallel to the thermal gradient direction for the enhanced thermodiffusion.

The ZrP nanoplates showed thermophilic behavior as they drifted to the warm and underwent a phase transition from isotropic to nematic phase as can be followed in figure 29. At time, t=0, the suspension appeared completely dark as it was isotropic. The left and right meniscus appeared bright due to reflection and/or scattering of light at the liquid-air interface. With the passage of time, as nanoplates thermophoretically drifted to the warm region, a small amount of nematic liquid crystalline phase formed within few minutes as shown in figure 29(c) after 80 min of thermophoresis. The local volume fraction of nanoplates at the bottom side of the hot end was thus 7% according to the room phase diagram shown in figure 28(d). Subsequent growth of the nematic liquid crystal can be observed at 200 min, 400 min, 800 min, 1200 min and 1400 min is shown in figure 29(c-i).

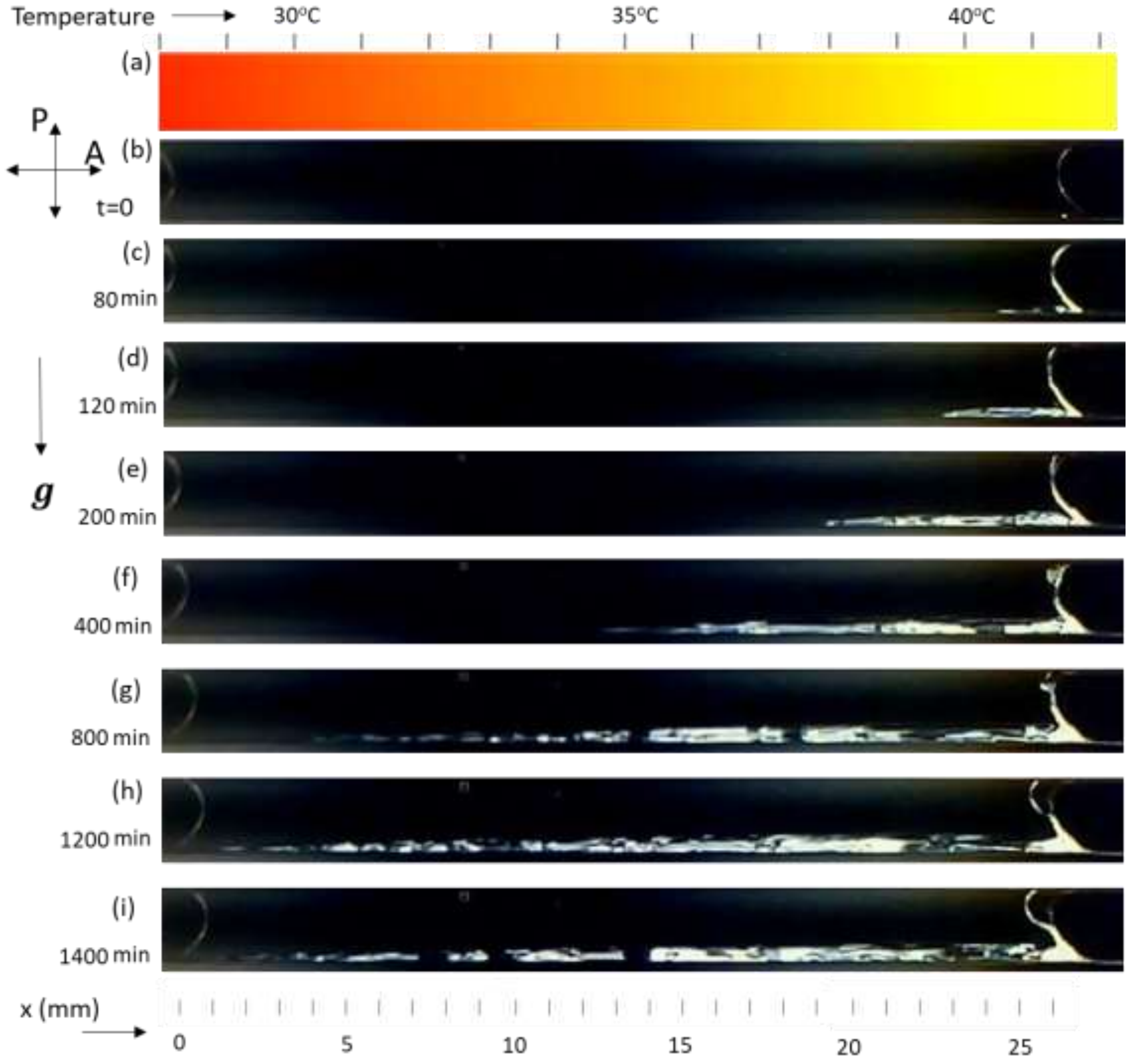

**Figure 29 Time dependent images of a 2mm high, 26mm long capillary containing isotropic sample. (a) Temperature gradient distribution along the length of capillary as measured by the infrared thermal imaging camera. (b-g) Polarized optical images of the sample capillary. At time, t=0, (b) the suspension appeared completely dark indicating the suspension was purely isotropic. With the passage of time, as nanoplates were thermophoretically diffused to the hot region, a small amount of nematic liquid crystalline phase formed as shown in (c) 80 min. Subsequent growth of the nematic liquid crystal can be observed at (d) 120 min, (e) 200 min, (f) 400 min, (g) 800 min, and reaches steady state at (h) 1200 min and the amount of birefringent nematic remains the same as shown in (i) 1400 min.**

Localized nematic phase called nematic tactoids are formed in warmer regions of the capillary are not visible in Figure 29 due to low magnification. But the many tactoids upon coalescence formed birefringent (appearing bright between crossed polars) phase as can be observed in the image after 80min of thermophoresis. Birefringent nematic nuclei moving to warm regions hit the liquid-air meniscus and bottom edge of the warm end of the sample column in the microcapillary. The phase transition to nematic from isotropic corresponds to increase of local concentration of nanoplates from 4% to 7% as shown in the phase diagram in figure 28(d). For a similar increase of concentration from ~50% to ~55%, the spherical nanoparticles required more than two weeks[50] whereas nanoplates in this experiment required only an hour. This indicated that the thermodiffusion of 2D nano-colloids is much faster as compared to spherical nano-colloids. The growth of the nematic phase at later times can be followed from time dependent images shown in Figure 29.

Flux of nanoplates either along or opposite to the direction of thermal gradient given by $j_{\mathrm{th}} = -\phi(1-\phi)D_T\nabla T + D\nabla\phi$, where $\phi$ is the volume fraction of nanoplates. The nanoplates showed thermophilic behavior by moving to warmer regions and undergoing phase transition from isotropic to nematic phase. The gravity sedimentation flux was vertically downward with the magnitude $j_{\mathrm{g}} = \phi \mathrm{v}_t$, where $\mathrm{v}_t$ is the sedimentation velocity of nanoplates. Since the first liquid crystal was found at the extreme of the warm region (Figure 3b), the sedimentation flux of ZrP nanoplates was understood to be smaller than the thermophoretic flux. The net flux experienced by nanoplates made a very small angle, $\phi$, with horizontal. Tactoids, being in micrometer size, however, have much larger sedimentation speeds than nanoplates. The isotropic liquid- nematic liquid crystal interface made an angle $\theta$ with the horizontal direction at steady state, figure 30(a). Magnitude of angle $\theta$ was found to be 0.6° as calculated from image analysis in imageJ. Angle $\theta$ seems related to $\phi$ as both are very small however since nanoplates motion is not visible under the microscope a clear measurement of $\theta$ was not possible.

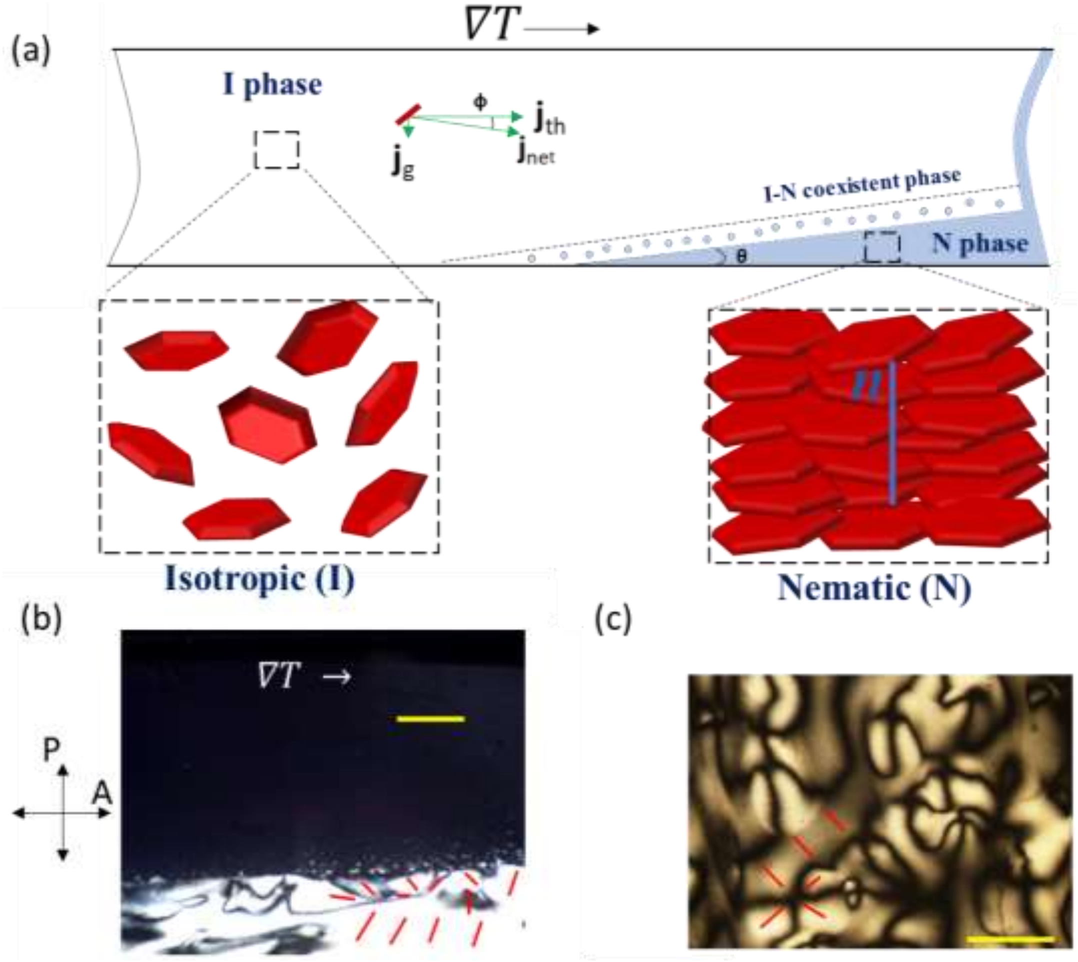

**Figure 30 (a) Demonstration of growth process of nematic liquid crystal. thermophoretic flux ($j_{th}$) of nanoplates was towards hot end in horizontal direction while gravity sedimentation ($j_g$) vertically downwards. The net flux ($j_{net}$) was dominated by thermal flux as the LC nematic nuclei were formed at the meniscus at the hot end. Local evaporation was in negligible amount. Inscribed in squares underneath are nanoplates in isotropic phase having random orientations (left) and in the nematic phase (director, n) (b) Polarized optical microscope image of thermophoretically formed nematic phase. Red lines indicated the local nematic directors. The topological structure was dominated with semi integer (±1/2) type declination (c) Polarized optical micrograph of nematic phase formed spontaneously at higher volume fraction of nanoplates ($\phi$=7%) without the temperature gradient in which the majority of topological defects were of the integer (±1) type. The elastic splay deformation of director field was higher as compared to that in the thermophoretically formed nematic phase. Scalebar: 400µm.**

The growth of nematic liquid crystal nucleated at the hot end was observed in a setup with a higher magnification (4X) lens focused at the hot end. Red lines in figure 30(b) and (c) indicate the local directions of nematic ordering called directors (***n***), as defined in the schematic of nematic phase of nanoplates in figure 30(a). Thermophoretically formed nematic phase, shown in figure 30(b), did not have integeral (±1) defects which were predominant in spontaneously formed nematic phase at initial concentration of nanoplates above $\phi_{\text{I-N}}$ as shown in figure 30(c). Moreover, the region with homogeneous nematic director was larger in thermophoretically controlled nematic phase. Both the observations indicate that the splay deformation of the director field in thermophoretically limited growth is lesser than the nematic formed spontaneously. We argue that due to slow growth over timescale of few hours, the coalescence of small nematic nuclei, having homogenous director distribution, takes place slow enough to obtain topologically more stable structures. It is well known that the energetically less expensive, m=±1/2 strength defects are favored to m=±1 defects [98]. The topological sturdiness of thermophoretically controlled nematic phase can be attributed to its slow, controlled growth achieved via external temperature gradient. The dynamic response of topological defects in nematics in presence of temperature gradient can be followed from supplementary movie 1 and it is being studied separately. Recently edge dislocations in smectic film were found to undergo displacement in presence of temperature gradient [99].

Hard spheres liquid suspensions under temperature gradient showed intriguing results in which single crystals nucleated at the cold region [50]. It was argued that at mechanical equilibrium, the osmotic pressure was constant throughout the long cell as the crystal and the fluid phase coexisted. Osmotic pressure of a colloidal suspension is given by $\Pi = nk_B TZ(\phi)$ where n is the number of particles, $k_B$ is the Boltzmann constant, T is the absolute temperature and Z($\phi$) is the compressibility factor of the corresponding phase. The osmotic balance could explain the accumulation of hard spheres (higher number of colloids, n) at cold end (lower T) and thus the formation of crystals at cold end [50]. Roughly, the osmotic balance leads to accumulation of particles at cold end after establishment of the mechanical equilibrium. However, Piazza [97] argued that the colloids can diffuse to either hot end or cold end depending on the particle/solvent interaction and there have been experimental evidences for the same [100].

The rate of growth of liquid crystal can be related to the net flux of particles as per the equation $(\phi_N - \phi_I)\frac{1}{A}\frac{\partial V_N}{\partial t} = j = -D\nabla\phi + \phi(1-\phi)D_T\nabla T$ where $V_N$ is the volume occupied by of nematic phase, $\phi$ The rate of nucleation of nematic nuclei and their sedimentation is assumed to happen faster than thermophoretic flux so that the growth of nematic liquid crystal is limited by the thermos-diffusive flux given by the right-hand side of the above equation. By processing the images of the growth process shown in figure 29 as a function of time, the nematic LC growth rate was obtained as $\frac{\partial V_N}{\partial t} = 0.0142 \pm 0.0025\, mm^3/min$ calculated via image processing tool− IDL 6.0 by identifying isotropic and nematic interface and calculating the area under the I-N curves as shown in figure 31(a,b). Thus, the liquid crystal growth rate becomes, $\frac{\partial L_{LC}}{\partial t} \sim (5.92 \pm 1.04) \times 10^{-7} m/s$, which comparable in order of magnitude with that of spherical colloids (~2 x $10^{-7}$ m/s). Although the value reported for spherical colloids was two order magnitude higher than that can be calculated for the shown growth of 1mm crystal in about two-week period.

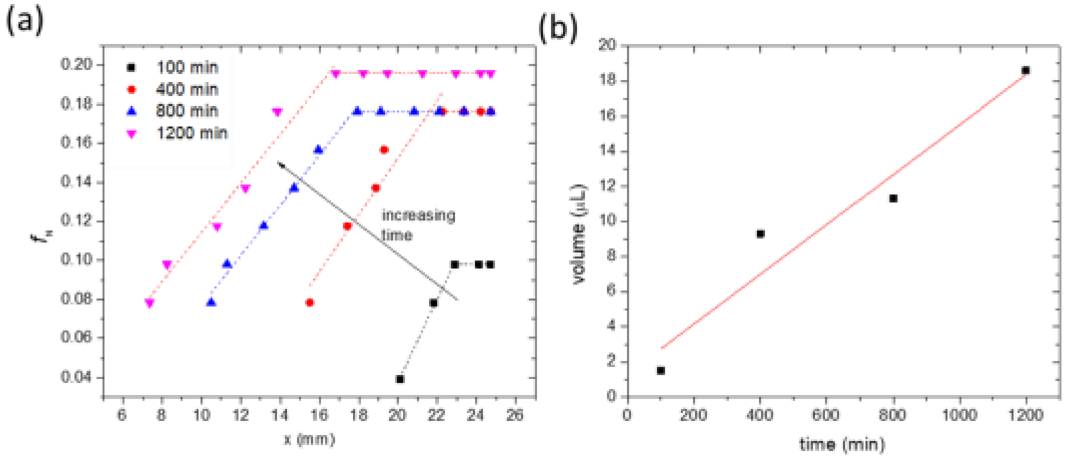

**Figure 31 (a) Nematic height fraction in the capillary tube with distance along temperature gradient at different time. The fitting of each nematic height profile at each time is done with two lines, with the one near the hot end becoming flat due to meniscus effect. (b) The volume of nematic phase formed as a result of thermophoresis of nanoplate colloids as a function of time. Value at each time is obtained as area under the curves in part a.**

A steady state of thermophoresis should ideally be achieved in the suspension at which the thermophoretic flux becomes zero. The growth of liquid crystal stopped after about 20 hours at which the amount of liquid crystal did not change as can be seen in figure 29(h,i). The concentration distribution of nanoplates at steady state gives an estimation of the Soret coefficient ($S_T$). The height of the nematic phase increases with volume fraction as demonstrated in figure (b). The nematic fraction ($f_N$) at steady state was measured using ImageJ and the variation with distance along thermal gradient is shown in figure 32 (a). As argued before, the I-N interface was found to be linear excluding the portions near the meniscus where the distribution was disturbed due to surface tension. The slope of the linear region is indicative of the ratio of thermal force to gravitational force which was found out to be 0.0109±0.0005. The volume fraction of nanoplates was obtained from nematic fraction, following the relationship, $f_N = a_1 + a_1\phi$ . The profile of volume fraction ($\phi$) plotted against thermophoretic distance (x) followed linear relation as shown in figure 32(b). This result is similar to that of polystyrene particles under a radial temperature gradient [95]. The steady state concentration profile led to calculation of Soret coefficient following the relationship: $S_T = -\frac{1}{\phi}\frac{\frac{d\phi}{dx}}{\frac{dT}{dx}}$ . The collective effects reduced the Soret effect at higher volume fraction of nanoplates as shown in figure 32(c). The fitting function $S_T \sim S_{T0}\,(1 - B\phi)$ was used to describe the effect of volume fraction which was previously described as $S_T \sim S_{T0}\,/(1 + B\phi)$ by Piazza [101]. The fitting function results the value of Soret coefficient at infinitely dilute nanoplate suspension, $S_{T0}$, as -0.0241±0.0001K$^{-1}$. The rate of decrease of Soret coefficient with volume fraction (B) was found to be 10.4±0.1 K$^{-1}$.

In the limit of extreme dilution, the interactions between colloids can also be neglected; however in concentrated colloidal suspensions, thermophoresis can be understood as the sum of single particle and collective effects[88]. Colloids with repulsive interactions were found to be more effective in accumulating in warm regions as compared to the solvent molecules [102]. The colloidal suspensions studied in this experiment to show significant collective effects. Collective effects in SDS micellar solutions have shown a decrease in Soret coefficient at moderate concentrations [92].

The decrease in the magnitude of Soret coefficient with the volume fraction was indicative of the collective effects. Interactions between colloids at higher volume fraction has previously been reported to decrease the Soret effect [92].

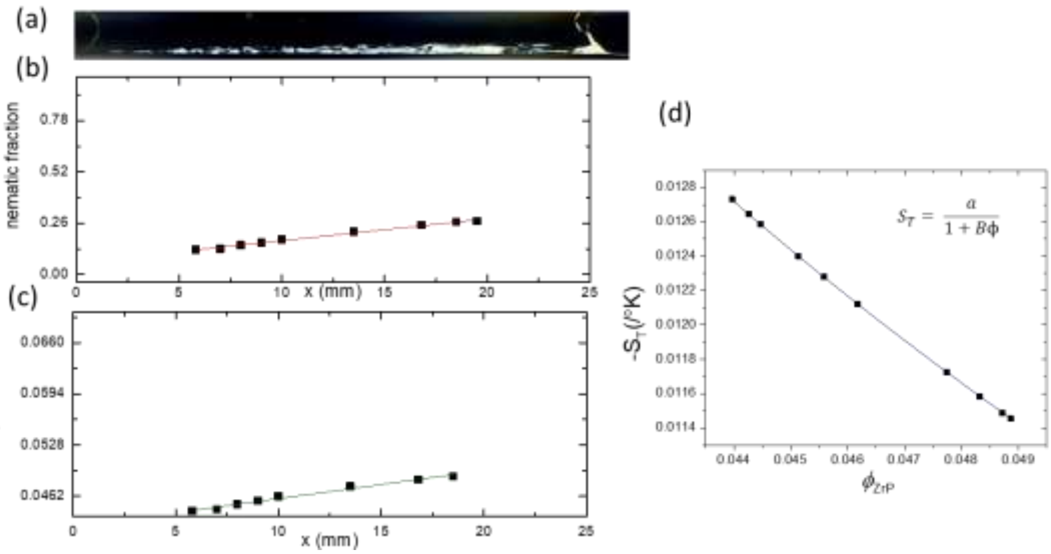

**Figure 32 (a) Image of sample kept in temperature gradient at steady state ~20 hours after the beginning of the process (b) Nematic fraction, $f_N$, showed linear increase with distance along direction of increasing temperature, x. (c) Nanoplate volume fraction at steady state as a function of x. (d) Magnitude of Soret coefficient plotted against nanoplate volume fraction fit to $S_T = a/(1+B\phi)$. Lower magnitude of $S_T$ at high concentrations indicated collective effects of nanoplate interactions on thermophoresis**

The translational diffusion coefficient (D) for nanoplates of size 260nm and thickness 2.68nm is 8.1x$10^{-5}$ $m^2$/s following the relationships between translational diffusivity of platelets given in reference[103]. Due to the size polydispersity of the nanoplates, the value can vary between 3x$10^{-5}$ and 1.3x$10^{-4}$. Thermophoretic diffusivity ($D_T$) can be then calculated as, $D_T = -DS_T$ ~ (−9.72±6.3) x $10^{-7}$ $m^2$/s/K. Our value is higher than the thermal diffusivity range for macromolecules which is $10^{-8}$ and $10^{-7}$

$cm^2/s/K$ as mentioned in reference [88] mostly due its anisotropic shape. Although the thermophoretic mobility, $D_T$, is universally in the range of $10^{-8}$ and $10^{-7}$ $cm^2s^{-1}$ $K^{-1}$, its actual value is very specific to the system and it cannot simply be related to bulk or surface properties [104].

## 5.6 Conclusion

In summary, we demonstrated the thermophoretic effects in aqueous suspensions of highly anisotropic zirconium phosphate colloidal nanoplates. It was found that thermophoresis of nanoplates, over a timescale of a few hours, resulted in an isotropic to liquid crystalline nematic phase transition. An increasing fraction of nematic liquid crystals towards the warmer region was indicative of positive density gradient towards the warm region. Based on the optical birefringence, the density profile was measured and Soret coefficient ($S_T$) of colloidal nanoplates was measured for first time. The interface between isotropic and nematic phases was found to be linear with a small angle of inclination decided by gravity sedimentation and thermophoretic fluxes. The results disclosed herein indicate that thermophoresis could play a significant role in dynamically control over the self-assembly and robust growth of 2D colloidal building blocks into soft continuous nanostructures, which not only helps to uncover the mystery world of soft condensed matter, but also paves an avenue for their emerging applications in advanced functional materials and beyond.

# CHAPTER VI

# EXPERIMENTAL MEASUREMENT OF THERMODYNAMIC EQUATION OF STATE NEMATIC PHASES

## 6.1 Abstract

Colloid phase transitions occur at constant volume rather than constant pressure. During the phase transition, the osmotic pressure and chemical potential of the system continually changes. The relationship between the thermodynamic variables osmotic pressure ($\Pi$) and colloid volume fraction ($\phi$) is known as equation of state and has been studied at length using Onsager theory and its improvements. Yet their experimental validation is missing. The measurement of volume fraction profile in an equilibrium sediment is a well-established method to measure colloidal osmotic pressure. Through birefringence ($\Delta n$) measurement of rainbow-like color bands obtained in a magnetic field aligned nematic sediment, we measured the volume fraction profile and hence the osmotic pressure of the nematic phase which was found to agree with the theoretical equation of state of the nematic phase of hard nanoplates, with a positive deviation at higher volume fractions. Due to absence of birefringence in isotropic phase, x-ray absorption technique was deployed for the measurement of volume fraction profile of platelets in an equilibrium isotropic sediment.

## 6.2 Theoretical equations of isotropic and nematic states

Onsager [35] in his seminal work, wrote a free energy functional for isotropic-nematic phase transition of anisotropic particles. Onsager's free energy functional considered expansion of free energies of isotropic and anisotropic states only up to second virial coefficient. It could not accurately explain the isotropic-nematic phase transition in hard platelets of moderate aspect ratio, as the higher body interactions between such platelets are dominant. The Parsons-Lee approximation considered obtaining the higher order virial coefficients for hard platelets by scaling the virial coefficients for the hard sphere systems[105,106]. Considering Parsons-Lee approximation, Wu [60] recently derived a generic equation of state for hard platelets that best explains the isotropic-nematic transition and the osmotic pressure($\Pi$) and chemical potential ($\mu$) in isotropic (iso) and nematic (nem) phases are given as follows:

$$\frac{\Pi_{nem}V_p}{k_BT} = \phi\left(1+\frac{4\phi-2\phi^2}{4(1-\phi)^3}+\left(\tilde{B}_3^{iso}-\frac{10}{4}\right)\phi^2+\tilde{a}\,\frac{\phi^3-\phi^4/2}{(1+\phi)^3}\right)B_2^{nem} \quad \ldots \text{eq. (6.1)}$$

$$\frac{\mu_{nem}}{k_BT} = \frac{\mu_o}{kT}+ln\phi+ln\alpha-1+G'(\phi)B_2^{nem} \quad \ldots \text{eq. (6.2)}$$

$$\frac{\Pi_{iso}V_p}{k_BT} = \phi\left(1+\frac{4\phi-2\phi^2}{4(1-\phi)^3}+\left(\tilde{B}_3^{iso}-\frac{10}{4}\right)\phi^2+\tilde{a}\,\frac{\phi^3-\phi^4/2}{(1+\phi)^3}\right)B_2^{iso} \quad \ldots \text{eq. (6.3)}$$

$$\frac{\mu_{iso}}{k_BT} = \frac{\mu_o}{kT}+ln\phi+2G'(\phi)B_2^{iso} \quad \ldots \text{eq. (6.4)}$$

where $\Pi_{nem}$and $\Pi_{nem}$ are the osmotic pressures in nematic and isotropic phase, $V_p$ the particle volume, $k_B$ the Boltzmann constant, $T$ the absolute temperature, $\phi$ the volume fraction of the platelets, $\xi$ the aspect ratio defined as the ratio of thickness to diameter of platelets and constants that are functions of the platelet aspect ratio are, $B_2^{iso}V_p = 0.6189 +$

$2.34326\xi$ and $B_2^{nem} = C_o^* + C_1^*\sqrt{\pi}\left(\frac{1}{\sqrt{\alpha}} - \frac{15}{16\sqrt[3]{\alpha}}\right) + \frac{4}{\alpha}C_2^*$, where the nematic order parameter $\alpha(\phi,\xi)$ is obtained by minimizing the free energy and it is given by, $\alpha(\phi,\xi) = 9\max_j\left[\frac{-128\times 8}{45\sqrt{\pi}}\left(\frac{2}{\xi}+\frac{8\xi}{\pi}\right) - 2\left\{\left(\frac{-128\times 8}{45\sqrt{\pi}}\left(\frac{2}{\xi}+\frac{8\xi}{\pi}\right)\right)^2 + \frac{48}{45}\right\}^{\frac{1}{2}} cos\left(\frac{1}{3}\cos^{-1}\left(-\frac{27}{2}g(\phi,\xi) + \frac{2j\pi}{3}\right)\right)\right]^{-2}$ where

$g(\phi,\xi) = \frac{\frac{32}{45}\left(\left(\frac{2}{\xi}+\frac{8\xi}{\pi}\right)\sqrt{\pi}\frac{4\phi-2\phi^2}{8(1-\phi)^2}\right)^{-1} + \frac{1}{3}\frac{16p}{45}+\frac{2}{27}p^3}{2p^2-\frac{32}{15}}$ wherein $p = -\frac{128}{45\sqrt{\pi}}\frac{\left(\frac{3\pi}{4}+\frac{8}{\pi}-7\right)}{\left(\frac{2}{\xi}+\frac{8\xi}{\pi}\right)}$. The other particle shape dependent constants are: $B_3^{iso} = \frac{0.15+1.67\xi+3.29\xi^2}{\frac{\pi}{4}\xi-\frac{\pi}{12}\xi^3}$, $\tilde{a} = \frac{-2+7\xi}{\frac{\pi}{4}\xi-\frac{\pi}{12}\xi^3}$ and $C_1^* = \left(\frac{2}{\xi}+\frac{8\xi}{\pi}\right)$, Constant $C_o^* = 8$ and $C_2^* = \left(\frac{3\pi}{4}+\frac{8}{\pi}-7\right)$.

$$G'(\phi) = \frac{1}{2}\left\{\frac{8\phi - 9\phi^2 + 3\phi^3}{4(1-\phi)^3} + \frac{3}{2}\left(\tilde{B}_3^{iso} - \frac{10}{4}\right)\phi^2 \right.$$
$$\left. + \tilde{a}\left[\frac{-10\phi + 25\phi^2 + 13\phi^3 + 4\phi^4}{4(1+\phi)^3} + \frac{5}{2}\ln(1+\phi)\right]\right\}$$

As stated before, the isotropic – nematic phase transition in hard platelets is a function of platelet volume fraction. The transition points are functions of platelet aspect ratio that is the thickness (L) to diameter (a) ratio. Thus, for a given aspect ratio, transition points $\phi_i$ and $\phi_N$ are obtained by solving establishing the phe phase coexistence between isotropic and nematic states ensuring the equality of pressure and chemical potential in both phases as $\Pi_{iso} = \Pi_{nem}$ and $\mu_{nem} = \mu_{iso}$.

## 6.3 Experimental measurement of the equation of state

In an equilibrium sediment of colloids, Osmotic pressure balances the effective weight of the colloids in an equilibrium colloidal sediment [107] and hence the integration of the volume fraction profile over the sample height gave the osmotic pressure (Π) as per the following relation:

$$\frac{d\Pi}{dz} = \Delta\rho\phi(z)g = (\rho_p - \rho_s)\phi(z)gdz$$

Osmotic pressure at the top of the sample is zero as there are no colloids above the top and hence

$$\Pi(z) = \int_0^z (\rho_p - \rho_s)\phi(z)gdz \quad \ldots \text{ eq. (6.5)}$$

In a coexisting isotropic-nematic sample kept in gravity, upon reaching equilibrium,

$$\Pi_{nem}(z) = \Pi_{I-N} + \left(\rho_p - \rho_s\right)g \int_z^{z_{I-N}} \phi(\tau)\,\mathrm{d}\tau\,, \quad \ldots \text{ eq. (6.6)}$$

where the subscript I-N indicates the isotropic (I)–nematic (N) interface, and $\rho_p$ and $\rho_s$ are the densities of the particle and solvent, respectively. In an experiment to measure the volume fraction profile of an equilibrium nematic sediment, a isotropic-nematic coexisting phase sample was kept in a vertical tube for over two weeks. The density gradient was developed due to sedimentation and near equilibrium state was established. Then using magnetic field of strength 2T, the platelets in the nematic phase were aligned to result different interference color bands at different heights of the sample. Each color band had a concentration related to its color as per the Michel-Levy chart[108]. The volume fraction profile of nanoplates in the nematic phase were obtained as shown in figure 33(a) where seven data points were obtained from seven different interference color bands and the volume fraction varied with the sample height as $\phi = 0.080 - 0.380z/H + 0.138(z/H)^2$, where the total sample height was $H$. A similar trend of the volume fraction profile was recently reported through computer simulation of sedimenting platelets [109].

Based on the density profile we obtained above, the osmotic pressure profile was obtained following equation for $\Pi_{nem}(z)$. The normalized osmotic pressure estimated from nanoplate volume fraction profile was plotted with green-shaded curve in figure 33(b). The repulsive interactions between the charged nanoplates were screened by the addition of tetrabutyl ammonium chloride (TBACl) salt; hence, the measured equation of state could be compared with that of the hard nanoplates. Unlike the hard spheres, the equation of state of hard nanoplates is very sensitive to aspect ratio ($\xi$); therefore, an appropriate aspect ratio of hard nanoplates was needed to be chosen for comparison with our experiment. A fair degree of faithfulness between the measured osmotic pressure and the equation of state proposed by Wu [60], described in the previous section, was found as indicated by figure 33(b). We chose nanoplates with aspect ratio ($\xi$) 0.0105±0.0005 to plot the theoretical equation of state. The chosen value of aspect ratio corresponded to the closest match between experimental measurement and theoretically predicted EOS. Since the average lateral size of nanoplates was 191±34 nm as measured by DLS, the corresponding thickness of nanoplates was calculated as 2.02±0.09 nm. Considering that the thickness of the core ZrP nanoplate was 0.68nm reported from ZrP crystal structure studied using X-ray [110], the tetrabutyl ammonium counterion layer thickness on each side of the nanoplate turned out to be 0.67 ± 0.05 nm. In an infinitely dilute state, the counterion thickness for ZrP colloid was reported close to 1 nm [29]. The compression of the stern layer by ~0.23± 0.05 nm was thus indicated by our experiment. In order to explain the possible deviation from theoretical EOS at high volume fraction $\phi$, it is important to acknowledge that the measurement from our experiment rather corresponded to a quasi-equilibrium, because the sedimentation equilibrium needs much longer to establish according to recent computer simulations[109]. After initial isotropic-nematic phase separation that takes place in few hours, the volume fraction profile changes slowly [109]. The current measurement was performed after two weeks of sedimentation and hence the system was in a quasi-equilibrium state. As a result, the measured osmotic pressure (green curve) was higher than theoretical calculations for monodisperse platelets of same aspect ratio (black curve) in high concentration range, $\phi$>0.065, as can be seen in figure 33(b). As the system reaches sedimentation equilibrium with the passage of time, the measured osmotic pressure curve (green) is expected to move closer to the one obtained from theoretical calculations (black). Such positive deviation from theoretically predicted equation of state was previously observed in hard sphere crystal phase and was attributed to polycrystalline nature of the sample[111]. Since we used magnetic field to form monodomains, this possibility can be neglected. The sample polydispersity could also be responsible for the deviation, since the platelet equation of state is very sensitive to the aspect ratio.

We now consider a simplified form of the equation of state of hard platelets, similar to the virial expansion of the EOS of the hard sphere crystal phase [112].

## 6.4 Proposing a simpler EOS of nematic in the low aspect ratio limit and experimental validation

The functional form of the hard platelet equation of state (EOS) involves sinusoidal as well as non-integer power functions of volume fraction and the aspect ratio. Hard sphere EOS on the other hand is quite simpler and represented in polynomial over polynomial form of volume fraction.[112] We found that in the limit of highly anisotropic platelets (aspect ratio, ξ → 0), the equation of state of the nematic phase proposed by Wu[60] can be presented in polynomial over polynomial form.

$$\lim_{\xi \to 0} \frac{\Pi_{nem} V_p}{k_B T} = \lim_{\xi \to 0} \phi \left(1 + \frac{4\phi - 2\phi^2}{4(1-\phi)^3} + \left(\widetilde{B}_3^{iso} - \frac{10}{4}\right)\phi^2 + \tilde{a}\,\frac{\phi^3 - \phi^4/2}{(1+\phi)^3}\right) B_2^{nem} = \lim_{\xi \to 0} \phi\,(1 + f_1(\phi,\xi) f_2(\phi,\xi))$$

where $f_1(\phi,\xi)$ is a function of both the volume fraction ($\phi$) and the aspect ratio (ξ) but for the limit of highly anisotropic platelets as in our case $\xi = 0.01 \rightarrow 0$, it can be represented as, $f_1(\phi,\xi) = \frac{a' + b'\phi + c'\phi^2 + d'\phi^3 + e'\phi^4 + f'\phi^5 + g'\phi^6 + h'\phi^7}{(1-\phi^2)^3}$ where coefficients *a'* through *h'* are functions of aspect ratio, $\xi$ ; $f_2(\phi,\xi)$ can be reduced to the following format for the limit when the aspect ratio is close to zero, as the case for ZrP nanoplates (ξ~0.01); $g(\phi,\xi) = \frac{1-2\phi+\phi^2}{-2\phi+\phi^2} c_1(\xi) + c_2(\xi)$ and with a similar approach for the functional dependence of $\alpha(\phi,\xi)$ for the nanoplates of a certain aspect-ratio ($\xi$=t/D), the equation of state is purely a function of nanoplate volume fraction. Finally, the nematic equation of state can be represented using polynomial function of volume fraction as the follows:

$$\frac{\Pi_{nem} V_p}{k_B T} = \frac{\sum_{i=0}^{11} a_i \phi^i}{\phi^2 (2-\phi)^2 (1-\phi^2)^3} \ldots \text{Eq. (6.7)}$$

Each coefficient in the numerator, $a_i$, is a function of nanoplate aspect ratio, ξ. For he values of parameters *a* through *n* are obtained by fitting the above equation to the experimentally obtained osmotic pressure data and the fit is shown in figure 33(b). The parameter values are shown in the following table:

**Table 2 Parameters of proposed EOS, having a polynomial over polynomial form for low aspect ratio limit, fit to the experimental and theoretical data of osmotic pressures**

| Parameters | Value of parameters in equation (6.7) fit to experimentally measured osmotic pressure | Value of parameters in equation (6.7) fit to theoretical EOS due to Wu [60] |
|---|---|---|
| $a_0$ | $(6.60 \pm 0.03)\ 10^{-4}$ | $(6.65 \pm 0.08)\ 10^{-4}$ |
| $a_1$ | $(7.1 \pm 1.2)\ 10^{-2}$ | $(-4.3 \pm 0.1)\ 10^{-2}$ |
| $a_2$ | $(3.4 \pm 0.8)\ 10^{0}$ | $(1.3 \pm 0.0)\ 10^{0}$ |
| $a_3$ | $(-5.54 \pm 0.04)\ 10^{1}$ | $(-1.18 \pm 0.04)\ 10^{1}$ |
| $a_4$ | $(3.98 \pm 0.06)\ 10^{2}$ | $(4.00 \pm 0.05)\ 10^{2}$ |
| $a_5$ | $(8 \pm 37)\ 10^{4}$ | $(-2.83 \pm 0.04)\ 10^{3}$ |
| $a_6$ | $(-5.2 \pm 52.6)\ 10^{5}$ | $(1.07 \pm 0.02)\ 10^{4}$ |
| $a_7$ | $(-1.2 \pm 4.6)\ 10^{6}$ | $(-2.54 \pm 0.07)\ 10^{4}$ |
| $a_8$ | $(7.9 \pm 39.7)\ 10^{7}$ | $(4.38 \pm 0.14)\ 10^{4}$ |

**Table 2 continued**

| Parameters | Value of parameters in equation (6.7) fit to experimentally measured osmotic pressure | Value of parameters in equation (6.7) fit to theoretical EOS due to Wu[60] |
|---|---|---|
| $a_9$ | $(1.95 \pm 4.09)\ 10^8$ | $(-5.5 \pm 0.2)\ 10^4$ |
| $a_{10}$ | $(-2.61 \pm 2.34)\ 10^9$ | $(4.29 \pm 0.17)\ 10^4$ |
| $a_{11}$ | $(9.21 \pm 5.48)\ 10^9$ | $(-1.5 \pm 0.1)\ 10^4$ |

Onsager's original theory considered virial coefficient up to the second order [35]; but higher order terms that represent many body interactions are required to accurately explain the phase transitions in platelet suspensions [60]. It was argued that the virial coefficients of order more than two contribute negatively to the osmotic pressure, and terms up to fifteen in the virial expansion were required to explain the molecular dynamics simulation-based data [113,114]. The equation of state proposed in this work followed a similar format with each coefficient $a_i$ representing the virial coefficient of order $i$. The relative contribution of various terms in the equation of state can be found in figure 33(c). The red and black points represent the contribution of various terms obtained upon fitting equation (6.7) to the experimental data and to the data obtained by following Wu[60], respectively. As expected, the overall contribution from terms of order greater than 2 was negative (see figure 33(c)) and terms of order up to six were significant indicating the presence of many body interactions among colloidal nanoplates. This result reinstates the need to consider the higher order virial coefficients than were not considered in Onsager's theory.

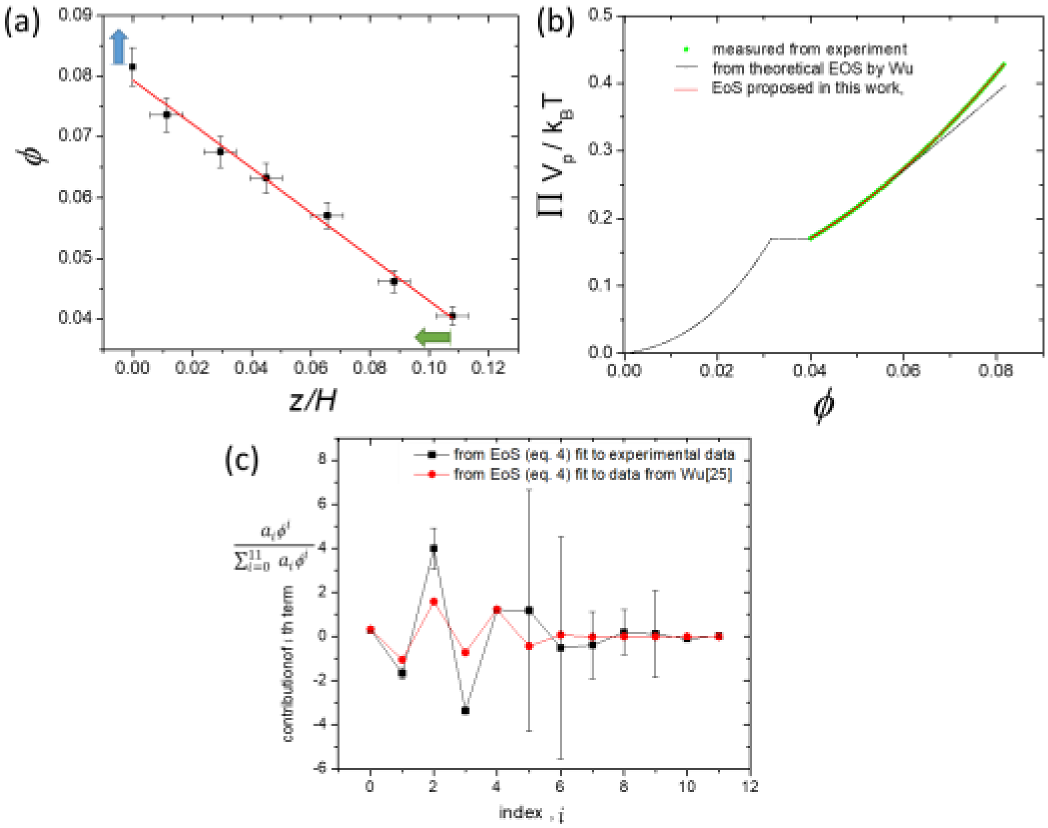

**Figure 33 Measurement of the equation of state of nematic phase and comparison with theoretical EOS and with a simplified, algebraic form of EOS for ξ → 0 (a) Nanoplate volume fraction ($\phi$) as a function of normalized sample height (*z/H*). Due to sedimentation, the volume fraction of nanoplates at the bottom of the sample slowly increases with time (blue arrow) and the I-N interface height decreases (green arrow). The kinetics to reach equilibrium sedimentation profile is very slow and can take much longer to achieve. (b) Normalized osmotic pressure in the nematic phase (green curve), EOS functional fit (red curve) as proposed, and theoretically predicted EOS for hard nanoplates with aspect ratio, <ξ>= 0.0105, (black curve). A good match between the measured osmotic pressure values (green curve) with the theoretical EOS (black) was observed in the low volume fraction range (0.04 < $\phi$<0.065). The higher values of osmotic pressure for $\phi$ > 0.065 indicated that sample had not yet reached the equilibrium. (c) Contribution of various terms in the polynomial of the proposed equation of state evaluated at $\phi$ = 0.05**

## 6.5 Measurement of EOS of isotropic phase

Since there is no optical birefringence in the isotropic phase, a different technique was required to measure the volume fraction profile ($\phi$ (z)) of platelets in isotropic sediment at equilibrium. We used X-ray attenuation technique schematically shown in figure 34 for the measurement of volume fraction profile. The sample was kept in gravity for six months.

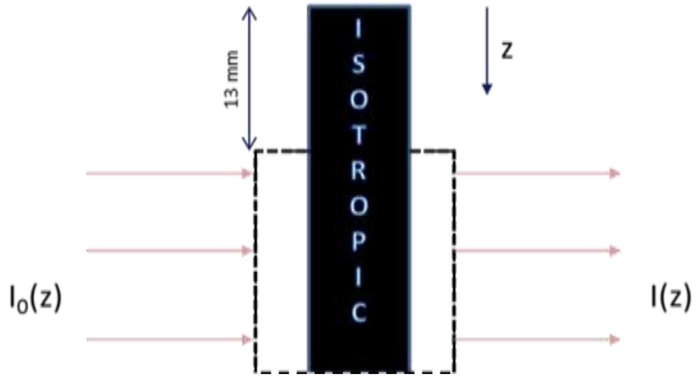

**Figure 34 Schematic of X-ray attenuation experiment. The sample shown here is top isotropic part of I-N coexisting phase that was sitting in gravity for about six months.**

Following procedure was used to find the volume fraction profile of the equilibrium:

$$log\frac{I_0}{I} = \varepsilon(z) \qquad \ldots (6.8)$$

$$\chi(z) = \frac{\varepsilon(z)_{sedimented\ sample} - \varepsilon(z)_{disperant}}{\varepsilon(z)_{uniform\ sample} - \varepsilon(z)_{disperant}} \qquad \ldots (6.9)$$

$$\phi(z) = c\chi(z) \qquad \ldots\ (6.10)$$

From the volume fraction profile obtained using above method in long time (about six months) sedimented sample of isotropic phase. Following equation is used to obtain osmotic pressure as a function of height from the volume fraction profile.

$$\Pi_{iso}(z) = \left(\rho_p - \rho_s\right) g \int_0^z \phi(\tau)\, \mathrm{d}\tau\,, \qquad \dots \text{ eq. } (6.11)$$

Red data points in figure 35 are obtained from experimentally measured volume fraction and equation 6.11. The black extrapolation is due to the missing data on the top of the sample due to limited window of x-rays. Upon comparing with the theoretical EOS, it turned out that the experimental data does not fit well with the theoretical EOS[60]. The osmotic pressure values were much higher than the theoretical EOS of the same aspect ratio of platelets (thickness = 2.68nm, size=1μm). For the same volume fraction, $\phi$, osmotic pressure of platelets with higher aspect ratio is higher than that of lower aspect ratio. So it can be understood that the charged platelets behave as hard platelets with much higher effective thickness as previously found in Gibbsite platelets [115].

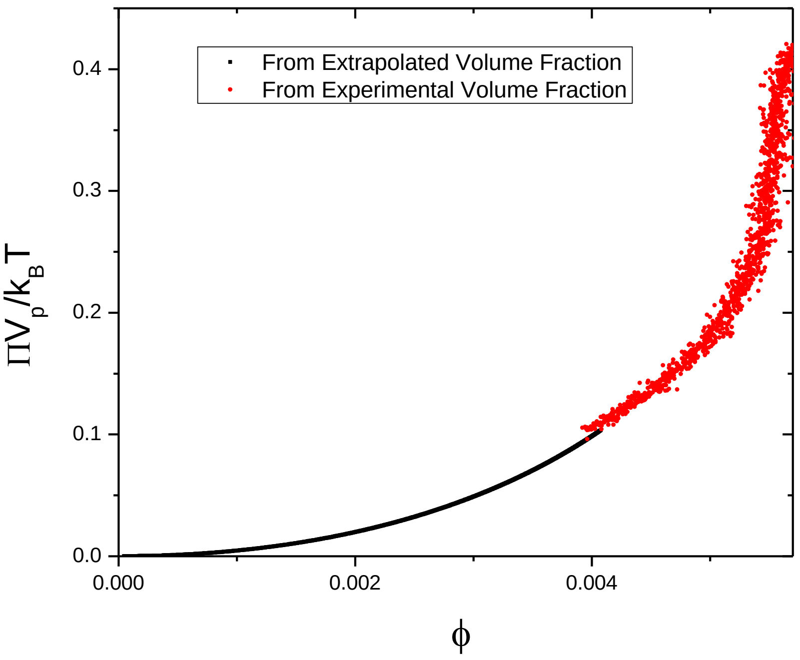

**Figure 35 Experimentally measured osmotic pressure (red curve) is equilibrium isotropic sediment and extrapolation (black curve)**

The slope of experimentally obtained EOS was also steeper than that theoretical EOS of scaled platelets with higher effective thickness. Since the sample used for experiment was polydisperse, size fractionation was possible. We chose a few points from the experimental EOS from figure 35. The chosen points are as shown in figure 36(a). Theoretical EOS of isotropic phase of different aspect ratio that pass through the experimental osmotic pressure values were found out. The theoretical EOS were obtained following reference [116]. The aspect ratios passing through the data points at a given z position of the sample corresponded to the nanoplate size at that z position as shown in figure 36(b). The sizes were obtained by considering that the nanoplates used in the study had uniform thickness of 2.68nm.

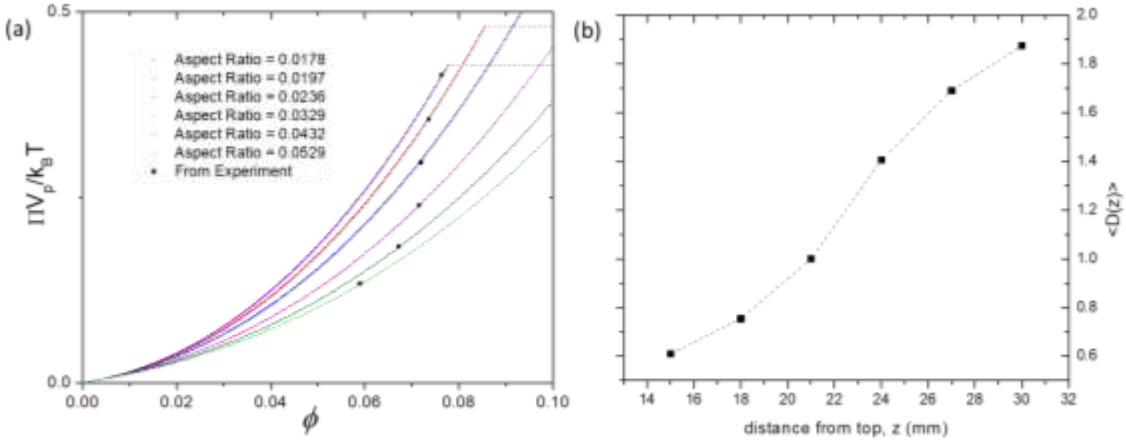

**Figure 36 (a) Few data points (shown in black solid squares) from the experimental osmotic pressure in equilibrium sediment that corresponded to EOS of platelets with different aspect ratio. (b) Average size of platelets obtained from corresponding aspect ratios at different heights**

We experimentally validated the size fractionation in long time sedimented samples of polydisperse platelets as shown in figure 37. Dynamic light scattering (DLS) was performed on samples at different heights.

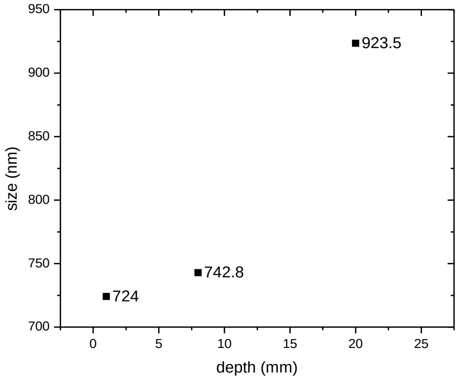

**Figure 37 Average size of samples carefully collected from different heights of isotropic sample sedimented for 6 months measured using dynamic light scattering.**

## 6.6 Conclusion

The osmotic pressure ($\Pi$) as a function of nanoplate volume fraction ($\phi$) was measured for the first time for the nematic phase of platelets. It was found to agree with the theoretical EOS, with a positive deviation at higher volume fractions. The deviations were because the colloidal platelet sediment may not be in the absolute equilibrium rather a near equilibrium situation might have been achieved. Among other factors, sample polydispersity and charges on colloids are responsible for the deviation. In isotropic suspension, the platelet effective thickness was higher than that in nematic phase. Size fractionation was prevalent in the suspension of polydisperse platelets. The results disclosed herein are expected to provide more insights on the understanding of 2D colloids such as graphene and graphene oxide[117], MXene [25], and beyond [118].

# CHAPTER VII

# CONCLUSION AND FUTURE WORK

Overall presentation of this dissertation makes it evident that the highly anisotropic ZrP nanoplates are model systems for the study of discotic liquid crystals. Chapter 2 emphasized on the investigation of the phase transitions in ZrP monolayer suspensions. Isotropic to nematic to smectic phase transition was found and the exact point where the N-S transition takes place still needs to be found. Suspensions of platelets need further attention at much higher concentrations (above 30-40%) where jamming of the suspensions due to high viscosity and gravity stress can take place. One advantage of the ZrP platelets is that their suspensions do not undergo gelation even at high concentrations. Search for characteristic defects of the smectic phase in platelet suspensions still remains active. of the reports of smectic phase in nanoplate suspensions, the smectic phase was characterized only based on the x-ray scattering; however a clear evidence of long range positional order is a focal conic defect typically found in molecular smectic liquid crystals yet remains to be found. Microgravity experiments that are planned at International Space Station under the NASA award Liquid Crystals of Nanoplates NNX13AQ60G are hopeful in this regard. Moreover, although columbic interactions between platelets can break chiral symmetry, a concrete model and experimental evidence of chiral phases are far from realization. Surface modification of the platelets to tune chiral interactions can be thought of.

Chapter 3 described the kinetics of nucleation and growth of nematic liquid crystals of nanoplates. A proportionality between number of nuclei and time showed agreement with the classical nucleation theory predictions. One of the important findings was that the nature of the growth was diffusion controlled at early times. Polarized optical microscopy was successfully deployed for the kinetics study.

The experimental realization of the theoretically predicted phase transitions in nanplates with negative anisotropy of electric polarizability was presented in Chapter 4. A positive evidence for the exotic biaxial nematic phase was presented and further proofs are required for confirming the biaxial nematic phase. Polarized optical microscopy of the samples kept in cylindrical capillary shall first show the escape of the nematic director along the axis of the cylinder and the dark line in optical microscope upon application of the e-field along the axis of the cylinder is expected to split into two dark lines upon uniaxial to biaxial phase transition. The exact location of the tri-critical point, in the $E^2$ vs. $\phi$ phase diagram, above which continuous isotropic-nematic phase transition takes place (see figure 20b). Volume fraction and electric field strength will need to be systematically varied.

Chapter 5 discussed the effect of external temperature gradient. The out of equilibrium state when a suspension of nanoplates in nematic phase is introduced to a temperature gradient can be studied in future. The dynamics of topological defects observed in the experiments presented in chapter 5 were not emphasized and need more attention in future. Figure 38 shows a capillary containing isotropic-nematic coexistent sample and the bright appearing phase is nematic. Point defects of strength half (red circle) and disclination loops (yellow boxes) in the nematic phase are shown. In presence of temperature gradient, the defects were observed to move to the hot end.

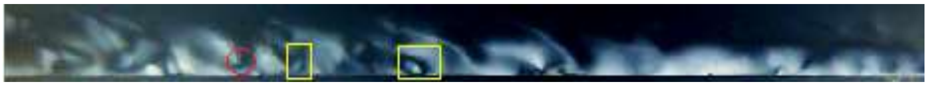

**Figure 38 Topological defects in nematic phase such as disclination loop (yellow box) and point defects (red circle). In presence of temperature gradient, defects move to hot end and disclination loops vanished along its way. From left to right, the temperature of the capillary decreases linearly.**

Chapter 6 emphasized the measurement of equation of state as a function of time to the measurement can to be done in future to establish true equilibrium. Osmotic pressure as a function of the sample height should be done using X-ray attenuation technique that provides higher resolution.

# REFERENCES

1 Jeong, J. *et al.* Chiral structures from achiral liquid crystals in cylindrical capillaries. *Proceedings of the National Academy of Sciences*, 201423220 (2015).

2 Zocher, H. On independent structure formation in brine. *Zeitschrift Fur Anorganische Und Allgemeine Chemie* **147**, 91-U15, doi:10.1002/zaac.19251470111 (1925).

3 Oldenbourg, R., Wen, X., Meyer, R. B. & Caspar, D. L. D. Orientational distribution function in nematic tobacco-mosaic-virus liquid-crystals measured by x-ray-diffraction. *Physical Review Letters* **61**, 1851-1854, doi:10.1103/PhysRevLett.61.1851 (1988).

4 van der Kooij, F. M. & Lekkerkerker, H. N. Formation of nematic liquid crystals in suspensions of hard colloidal platelets. *The Journal of Physical Chemistry B* **102**, 7829-7832 (1998).

5 Sun, D. Z., Sue, H. J., Cheng, Z. D., Martinez-Raton, Y. & Velasco, E. Stable smectic phase in suspensions of polydisperse colloidal platelets with identical thickness. *Physical Review E* **80**, doi:Artn 041704 10.1103/Physreve.80.041704 (2009).

6 Blinov, L. M. *Structure and properties of liquid crystals*. Vol. 123 (Springer Science & Business Media, 2010).

7 Kleman, M. & Lavrentovich, O. D. Topological point defects in nematic liquid crystals. *Philosophical Magazine* **86**, 4117-4137, doi:10.1080/14786430600593016 (2006).

8 Pieranski, P., Copar, S., Godinho, M. H. & Dazza, M. Hedgehogs in the dowser state. *European Physical Journal E* **39**, doi:ARTN 121 10.1140/epje/i2016-16121-7 (2016).

9 Frank, F. C. I. Liquid crystals. On the theory of liquid crystals. *Discussions of the Faraday Society* **25**, 19-28 (1958).

10 Nakato, T. *et al.* Electrooptic response of colloidal liquid crystals of inorganic oxide nanosheets prepared by exfoliation of a layered niobate. *The Journal of Physical Chemistry C* **115**, 8934-8939 (2011).

11 Verhoeff, A. A., Brand, R. P. & Lekkerkerker, H. N. W. Tuning the birefringence of the nematic phase in suspensions of colloidal gibbsite platelets. *Molecular Physics* **109**, 1363-1371, doi:10.1080/00268976.2011.559006 (2011).

12 Duboisvi.E, Degennes, P. G. & Parodi, O. Hydrodynamic Instabilities of Nematic Liquid Crystals Underac Electric Fields. *Journal De Physique* **32**, 305-+, doi:DOI 10.1051/jphys:01971003204030500 (1971).

13 Kawamoto, H. The History of Liquid-Crystal Display and Its Industry. *2012 Third Ieee History of Electro-Technology Conference (Histelcon)* (2012).

14 Shen, T. Z., Hong, S. H. & Song, J. K. Electro-optical switching of graphene oxide liquid crystals with an extremely large Kerr coefficient. *Nature Materials* **13**, 394-399, doi:10.1038/NMAT3888 (2014).

15 Sano, K. *et al.* Photonic water dynamically responsive to external stimuli. *Nature Communications* **7**, doi:ARTN 12559 10.1038/ncomms12559 (2016).

16 Wong, M. *et al.* Large-scale self-assembled zirconium phosphate smectic layers via a simple spray-coating process. *Nature Communications* **5**, 3589, doi:10.1038/ncomms4589 (2014).

17 Genkin, M. M., Sokolov, A., Lavrentovich, O. D. & Aranson, I. S. Topological Defects in a Living Nematic Ensnare Swimming Bacteria. *Physical Review X* **7**, doi:ARTN 011029
10.1103/PhysRevX.7.011029 (2017).

18 Peng, C., Turiv, T., Guo, Y., Wei, Q.-H. & Lavrentovich, O. D. Command of active matter by topological defects and patterns. *Science* **354**, 882-885 (2016).

19 Díaz, A. *et al.* Zirconium phosphate nano-platelets: a novel platform for drug delivery in cancer therapy. *Chemical Communications* **48**, 1754-1756 (2012).

20 Díaz, A. *et al.* Self-Assembled Monolayers Based Upon a Zirconium Phosphate Platform. *Chemistry of Materials* **25**, 723-728, doi:10.1021/cm303610v (2013).

21 Paineau, E. *et al.* Aqueous Suspensions of Natural Swelling Clay Minerals. 1. Structure and Electrostatic Interactions. *Langmuir* **27**, 5562-5573, doi:10.1021/la2001255 (2011).

22 Mullins, O. C. *et al.* Advances in Asphaltene Science and the Yen-Mullins Model. *Energy & Fuels* **26**, 3986-4003, doi:10.1021/ef300185p (2012).

23 Kim, J., Cote, L. J. & Huang, J. Two Dimensional Soft Material: New Faces of Graphene Oxide. *Accounts of Chemical Research* **45**, 1356-1364, doi:10.1021/ar300047s (2012).

24 Xu, Z. & Gao, C. Graphene chiral liquid crystals and macroscopic assembled fibres. *Nature Communications* **2**, 571, doi:10.1038/ncomms1583 (2011).

25 Anasori, B., Lukatskaya, M. R. & Gogotsi, Y. 2D metal carbides and nitrides (MXenes) for energy storage. *Nature Reviews Materials* **2**, 16098, doi:10.1038/natrevmats.2016.98 (2017).

26 Coleman, J. N. *et al.* Two-Dimensional Nanosheets Produced by Liquid Exfoliation of Layered Materials. *Science* **331**, 568-571, doi:10.1126/science.1194975 (2011).

27 Veerman, J. A. C. & Frenkel, D. Phase-Behavior of Disk-Like Hard-Core Mesogens. *Physical Review A* **45**, 5632-5648 (1992).

28 Marechal, M., Cuetos, A., Martinez-Haya, B. & Dijkstra, M. Phase behavior of hard colloidal platelets using free energy calculations. *Journal of Chemical Physics* **134**, 094501, doi:Artn 094501 Doi 10.1063/1.3552951 (2011).

29 Kim, H.-N., Keller, S. W., Mallouk, T. E., Schmitt, J. & Decher, G. Characterization of Zirconium Phosphate/Polycation Thin Films Grown by Sequential Adsorption Reactions. *Chemistry of Materials* **9**, 1414-1421, doi:10.1021/cm970027q (1997).

30 Shuai, M., Mejia, A. F., Chang, Y.-W. & Cheng, Z. Hydrothermal synthesis of layered a-zirconium phosphate disks: control of aspect ratio and polydispersity

for nano-architecture. *Cryst. Eng. Comm.* **15**, 1970-1977, doi:10.1039/c2ce26402a (2013).

31 Yu, Y.-H., Wang, X., Shinde, A. & Cheng, Z. Synthesis and Exfoliation of Discotic Zirconium Phosphates to Obtain Colloidal Liquid Crystals. e53511, doi:doi:10.3791/53511 (2016).

32 Sun, D. Z., Sue, H. J., Cheng, Z. D., Martinez-Raton, Y. & Velasco, E. Stable smectic phase in suspensions of polydisperse colloidal platelets with identical thickness. *Physical Review E* **80**, 041704, doi:Artn 041704 Doi 10.1103/Physreve.80.041704 (2009).

33 Mejia, A. F. *et al.* Aspect ratio and polydispersity dependence of isotropic-nematic transition in discotic suspensions. *Physical Review E* **85**, 061708, doi:10.1103/PhysRevE.85.061708 (2012).

34 Langmuir, I. The role of attractive and repulsive forces in the formation of tactoids, thixotropic gels, protein crystals and coacervates. *Journal of Chemical Physics* **6**, 873-896, doi:10.1063/1.1750183 (1938).

35 Onsager, L. The Effects of Shape on the Interaction of Colloidal Particles. *Annals of the New York Academy of Sciences* **51**, 627-659, doi:DOI 10.1111/j.1749-6632.1949.tb27296.x (1949).

36 Frenkel, D. & Eppenga, R. Monte-Carlo Study of the Isotropic-Nematic Transition in a Fluid of Thin Hard Disks. *Physical Review Letters* **49**, 1089-1092, doi:DOI 10.1103/PhysRevLett.49.1089 (1982).

37 van der Kooij, F. M., Kassapidou, K. & Lekkerkerker, H. N. Liquid crystal phase transitions in suspensions of polydisperse plate-like particles. *Nature* **406**, 868-871 (2000).

38 Sun, D., Sue, H.-J., Cheng, Z., Martínez-Ratón, Y. & Velasco, E. Stable smectic phase in suspensions of polydisperse colloidal platelets with identical thickness. *Physical Review E* **80**, 041704 (2009).

39 Kleshchanok, D., Holmqvist, P., Meijer, J. M. & Lekkerkerker, H. N. W. Lyotropic Smectic B Phase Formed in Suspensions of Charged Colloidal Platelets. *Journal of the American Chemical Society* **134**, 5985-5990, doi:10.1021/ja300527w (2012).

40 Vis, M., Wensink, H. H., Lekkerkerker, H. N. W. & Kleshchanok, D. Nematic and lamellar liquid-crystalline phases in suspensions of charged silica-coated gibbsite platelets. *Molecular Physics* **113**, 1053-1060, doi:10.1080/00268976.2014.985276 (2015).

41 Shuai, M. *et al.* Spontaneous liquid crystal and ferromagnetic ordering of colloidal magnetic nanoplates. *Nature Communications* **7**, doi:Artn 10394 10.1038/Ncomms10394 (2016).

42 Shinde, A., Wang, X. & Cheng, Z. Aspect Ratio Dependence of Isotropic-Nematic Phase Separation of Nanoplates in Gravity. *Gravitational and Space Research* **4** (2016).

43 He, P. *et al.* Hindrance function for sedimentation and creaming of colloidal disks. *Physical Review E* **81**, 026310 (2010).

44 Saeva, F. D. & Wysocki, J. J. Induced circular dichroism in cholesteric liquid crystals. *Journal of the American Chemical Society* **93**, 5928-5929, doi:10.1021/ja00751a075 (1971).

45 Saeva, F. D., Sharpe, P. E. & Olin, G. R. Cholesteric liquid crystal induced circular dichroism (LCICD). V. Mechanistic aspects of LCICD. *Journal of the American Chemical Society* **95**, 7656-7659, doi:10.1021/ja00804a019 (1973).

46 Wensink, H. H. & Lekkerkerker, H. N. W. Sedimentation and multi-phase equilibria in mixtures of platelets and ideal polymer. *Europhysics Letters* **66**, 125-131, doi:DOI 10.1209/epl/i2003-10140-1 (2004).

47 van der Beek, D., Schilling, T. & Lekkerkerker, H. N. W. Gravity-induced liquid crystal phase transitions of colloidal platelets. *Journal of Chemical Physics* **121**, 5423-5426, doi:10.1063/1.1783231 (2004).

48 Sahoo, Y. *et al.* Aqueous ferrofluid of magnetite nanoparticles: fluorescence labeling and magnetophoretic control. *The Journal of Physical Chemistry B* **109**, 3879-3885 (2005).

49 Matijevic, E. *Medical applications of colloids*. (Springer, 2008).

50 Cheng, Z. D., Russell, W. B. & Chaikin, P. M. Controlled growth of hard-sphere colloidal crystals. *Nature* **401**, 893-895 (1999).

51 Yethiraj, A. & van Blaaderen, A. A colloidal model system with an interaction tunable from hard sphere to soft and dipolar. *Nature* **421**, 513 (2003).

52 Phan, S. E. *et al.* Phase transition, equation of state, and limiting shear viscosities of hard sphere dispersions. *Physical Review E* **54**, 6633-6645, doi:10.1103/PhysRevE.54.6633 (1996).

53 Pusey, P. N. & Van Megen, W. Phase behaviour of concentrated suspensions of nearly hard colloidal spheres. *Nature* **320**, 340 (1986).

54 Ackerson, B. J. & Schätzel, K. Classical growth of hard-sphere colloidal crystals. *Physical Review E* **52**, 6448-6460, doi:10.1103/PhysRevE.52.6448 (1995).

55 He, Y., Ackerson, B. J., van Megen, W., Underwood, S. M. & Schätzel, K. Dynamics of crystallization in hard-sphere suspensions. *Physical Review E* **54**, 5286 (1996).

56 Cheng, Z. D., Zhu, J. X., Russel, W. B., Meyer, W. V. & Chaikin, P. M. Colloidal hard-sphere crystallization kinetics in microgravity and normal gravity. *Applied Optics* **40**, 4146-4151, doi:Doi 10.1364/Ao.40.004146 (2001).

57 Verhoeff, A. A., Bakelaar, I. A., Otten, R. H. J., van der Schoot, P. & Lekkerkerker, H. N. W. Tactoids of Plate-Like Particles: Size, Shape, and Director Field. *Langmuir* **27**, 116-125, doi:10.1021/la104128m (2011).

58 Auer, S. & Frenkel, D. Prediction of absolute crystal-nucleation rate in hard-sphere colloids. *Nature* **409**, 1020-1023, doi:Doi 10.1038/35059035 (2001).

59 Russel, W. B. On the Dynamics of the Disorder Order Transition. *Phase Transitions* **21**, 127-137, doi:Doi 10.1080/01411599008206886 (1990).

60 Wu, L., Wensink, H. H., Jackson, G. & Müller, E. A. A generic equation of state for liquid crystalline phases of hard-oblate particles. *Molecular Physics* **110**, 1269-1288, doi:10.1080/00268976.2011.649794 (2012).

61 Landsman, W. in *Astronomical Data Analysis Software and Systems II.* 246.

62 Zhang, C., Acharya, A., Walkington, N. J. & Lavrentovich, O. D. Computational modelling of tactoid dynamics in chromonic liquid crystals. *Liquid Crystals* **45**, 1084-1100, doi:10.1080/02678292.2017.1410240 (2018).

63 Jamali, V. *et al.* Experimental realization of crossover in shape and director field of nematic tactoids. *Physical Review E* **91**, doi:ARTN 042507 10.1103/PhysRevE.91.042507 (2015).

64 Tokuyama, M. & Enomoto, Y. Dynamics of crossover phenomenon in phase-separating systems. *Physical Review Letters* **69**, 312-315, doi:10.1103/PhysRevLett.69.312 (1992).

65 Löwen, H., Bechhoefer, J. & Tuckerman, L. S. Crystal growth at long times: Critical behavior at the crossover from diffusion to kinetics-limited regimes. *Physical Review A* **45**, 2399-2415, doi:10.1103/PhysRevA.45.2399 (1992).

66 in *Colloidal Dispersions Cambridge Monographs on Mechanics* (eds D. A. Saville, W. B. Russel, & W. R. Schowalter) 394-428 (Cambridge University Press, 1989).

67 van der Beek, D., Davidson, P., Wensink, H. H., Vroege, G. J. & Lekkerkerker, H. N. W. Influence of a magnetic field on the nematic phase of hard colloidal platelets. *Physical Review E* **77**, doi:ARTN 031708

10.1103/PhysRevE.77.031708 (2008).

68 Dozov, I. *et al.* Electric-Field-Induced Perfect Anti-Nematic Order in Isotropic Aqueous Suspensions of a Natural Beidellite Clay. *Journal of Physical Chemistry B* **115**, 7751-7765, doi:10.1021/jp201201x (2011).

69 Varga, S., Kronome, G. & Szalai, I. External field induced tricritical phenomenon in the isotropic-nematic phase transition of hard non-spherical particle systems. *Molecular Physics* **98**, 911-915, doi:Doi 10.1080/00268970050032765 (2000).

70 van der Beek, D., Davidson, P., Wensink, H. H., Vroege, G. J. & Lekkerkerker, H. N. Influence of a magnetic field on the nematic phase of hard colloidal platelets. *Phys Rev E Stat Nonlin Soft Matter Phys* **77**, 031708, doi:10.1103/PhysRevE.77.031708 (2008).

71 Martinez-Raton, Y., Varga, S. & Velasco, E. Biaxial nematic phases in fluids of hard board-like particles. *Phys Chem Chem Phys* **13**, 13247-13254, doi:10.1039/c1cp20698b (2011).

72 Dozov, I. *et al.* Electric-field-induced perfect anti-nematic order in isotropic aqueous suspensions of a natural beidellite clay. *The Journal of Physical Chemistry B* **115**, 7751-7765 (2011).

73 Chiccoli, C. *et al.* Topological defects in schlieren textures of biaxial and uniaxial nematics. *Physical Review E* **66**, doi:ARTN 030701 10.1103/PhysRevE.66.030701 (2002).

74 Harrison, C. *et al.* Mechanisms of ordering in striped patterns. *Science* **290**, 1558-1560, doi:10.1126/science.290.5496.1558 (2000).

75 Sullivan, M. *et al.* Control of colloids with gravity, temperature gradients, and electric fields. *Journal of Physics: Condensed Matter* **15**, S11 (2002).

76 Li, B. X., Borshch, V., Shiyanovskii, S. V., Liu, S. B. & Lavrentovich, O. D. Electro-optic switching of dielectrically negative nematic through nanosecond electric modification of order parameter. *Applied Physics Letters* **104**, doi:Artn 201105 10.1063/1.4879018 (2014).

77 Frka-Petesic, B., Radavidson, H., Jean, B. & Heux, L. Dynamically Controlled Iridescence of Cholesteric Cellulose Nanocrystal Suspensions Using Electric Fields. *Advanced Materials* **29**, 9, doi:10.1002/adma.201606208 (2017).

78 De Groot, S. R. & Mazur, P. *Non-equilibrium thermodynamics*. (Courier Corporation, 2013).

79 Chapman, S. The characteristics of thermal diffusion. *Proc. R. Soc. Lond. A* **177**, 38-62 (1940).

80 Chapman, S. Thermal diffusion in ionized gases. *Proceedings of the Physical Society* **72**, 353 (1958).

81 Bringuier, E. & Bourdon, A. Kinetic theory of colloid thermodiffusion. *Physica a-Statistical Mechanics and Its Applications* **385**, 9-24, doi:10.1016/j.physa.2007.06.011 (2007).

82 Geelhoed, P., Lindken, R. & Westerweel, J. Thermophoretic separation in microfluidics. *Chemical Engineering Research and Design* **84**, 370-373 (2006).

83 Vigolo, D., Rusconi, R., Stone, H. A. & Piazza, R. Thermophoresis: microfluidics characterization and separation. *Soft Matter* **6**, 3489-3493 (2010).

84 Giddings, J. C. Field-flow fractionation: analysis of macromolecular, colloidal, and particulate materials. *Science* **260**, 1456-1465 (1993).

85 Duhr, S. & Braun, D. Optothermal molecule trapping by opposing fluid flow with thermophoretic drift. *Physical Review Letters* **97**, doi:ARTN 038103
10.1103/PhysRevLett.97.038103 (2006).

86 Wiegand, S. Thermal diffusion in liquid mixtures and polymer solutions. *Journal of Physics: Condensed Matter* **16**, R357 (2004).

87 Ruckenstein, E. Can phoretic motions be treated as interfacial tension gradient driven phenomena? *Journal of Colloid and Interface Science* **83**, 77-81, doi:https://doi.org/10.1016/0021-9797(81)90011-4 (1981).

88 Piazza, R. & Parola, A. Thermophoresis in colloidal suspensions. *Journal of Physics-Condensed Matter* **20**, doi:Artn 153102
10.1088/0953-8984/20/15/153102 (2008).

89 Putnam, S. A. & Cahill, D. G. Transport of Nanoscale Latex Spheres in a Temperature Gradient. *Langmuir* **21**, 5317-5323, doi:10.1021/la047056h (2005).

90 Würger, A. Transport in Charged Colloids Driven by Thermoelectricity. *Physical Review Letters* **101**, 108302, doi:10.1103/PhysRevLett.101.108302 (2008).

91 Helfand, E. & Kirkwood, J. G. Theory of the Heat of Transport of Electrolytic Solutions. *The Journal of Chemical Physics* **32**, 857-866, doi:10.1063/1.1730808 (1960).

92 Piazza, R. & Guarino, A. Soret Effect in Interacting Micellar Solutions. *Physical Review Letters* **88**, 208302, doi:10.1103/PhysRevLett.88.208302 (2002).

93 Iacopini, S., Rusconi, R. & Piazza, R. The “macromolecular tourist": Universal temperature dependence of thermal diffusion in aqueous colloidal suspensions. *The European Physical Journal E* **19**, 59-67 (2006).

94 Braibanti, M., Vigolo, D. & Piazza, R. Does thermophoretic mobility depend on particle size? *Physical review letters* **100**, 108303 (2008).

95 Duhr, S. & Braun, D. Thermophoretic depletion follows Boltzmann distribution. *Physical Review Letters* **96**, doi:ARTN 168301
10.1103/PhysRevLett.96.168301 (2006).

96 vanBruggen, M. P. B., vanderKooij, F. M. & Lekkerkerker, H. N. W. Liquid crystal phase transitions in dispersions of rod-like colloidal particles. *Journal of Physics-Condensed Matter* **8**, 9451-9456, doi:Doi 10.1088/0953-8984/8/47/044 (1996).

97 Piazza, R. 'Thermal forces': colloids in temperature gradients. *J Phys-Condens Mat* **16**, S4195-S4211, doi:Pii S0953-8984(04)78995-X
10.1088/0953-8984/16/38/032 (2004).

98 Kurik, M. V. e. & Lavrentovich, O. Defects in liquid crystals: homotopy theory and experimental studies. *Physics-Uspekhi* **31**, 196-224 (1988).

99 Kurita, R., Mitsui, S. & Tanaka, H. Response of Soft Continuous Structures and Topological Defects to a Temperature Gradient. *Physical Review Letters* **119**, 108003, doi:10.1103/PhysRevLett.119.108003 (2017).

100 Giglio, M. & Vendramini, A. Soret-type motion of macromolecules in solution. *Physical Review Letters* **38**, 26 (1977).

101 Piazza, R. Thermal diffusion in ionic micellar solutions. *Philosophical Magazine* **83**, 2067-2085, doi:10.1080/0141861031000107971 (2003).

102 Lusebrink, D. & Ripoll, M. Collective thermodiffusion of colloidal suspensions. *Journal of Chemical Physics* **137**, doi:Artn 194904
10.1063/1.4767398 (2012).

103 Odriozola, G., Romero-Bastida, M. & Guevara-Rodriguez, F. d. J. Brownian dynamics simulations of Laponite colloid suspensions. *Physical Review E* **70**, 021405 (2004).

104 Wurger, A. Thermophoresis in colloidal suspensions driven by Marangoni forces. *Physical Review Letters* **98**, doi:ARTN 138301
10.1103/PhysRevLett.98.138301 (2007).

105 Parsons, J. Nematic ordering in a system of rods. *Physical Review A* **19**, 1225 (1979).

106 Lee, S. D. The Onsager-type theory for nematic ordering of finite-length hard ellipsoids. *The Journal of Chemical Physics* **89**, 7036-7037 (1988).

107 Piazza, R., Bellini, T. & Degiorgio, V. Equilibrium sedimentation profiles of screened charged colloids: A test of the hard-sphere equation of state. *Physical Review Letters* **71**, 4267-4270 (1993).

108 Sorensen, B. E. A revised Michel-Levy interference colour chart based on first-principles calculations (vol 25, pg 5, 2013). *European Journal of Mineralogy* **25**, 1041-1041, doi:10.1127/0935-1221/2013/0025-2364 (2013).

109 Sui, J., Ding, Y. & Doi, M. Dynamics of liquid crystalline phase transition in sedimenting platelet-like particles. *Soft Matter* **14**, 3049-3056, doi:10.1039/C8SM00254A (2018).

110 Clearfield, A. & Stynes, J. The preparation of crystalline zirconium phosphate and some observations on its ion exchange behaviour. *Journal of Inorganic and Nuclear Chemistry* **26**, 117-129 (1964).

111 Rutgers, M. A., Dunsmuir, J. H., Xue, J. Z., Russel, W. B. & Chaikin, P. M. Measurement of the hard-sphere equation of state using screened charged polystyrene colloids. *Physical Review B* **53**, 5043-5046, doi:DOI 10.1103/PhysRevB.53.5043 (1996).

112 Hall, K. R. Another Hard-Sphere Equation of State. *Journal of Chemical Physics* **57**, 2252-&, doi:Doi 10.1063/1.1678576 (1972).

113 Kolafa, J. & Rottner, M. Simulation-based equation of state of the hard disk fluid and prediction of higher-order virial coefficients. *Mol Phys* **104**, 3435-3441, doi:10.1080/00268970600967963 (2006).

114 Duncan, P. D., Dennison, M., Masters, A. J. & Wilson, M. R. Theory and computer simulation for the cubatic phase of cut spheres. *Physical Review E* **79**, 031702 (2009).

115 van der Beek, D. & Lekkerkerker, H. N. W. Liquid crystal phases of charged colloidal platelets. *Langmuir* **20**, 8582-8586, doi:10.1021/la049455i (2004).

116 Wu, L., Wensink, H. H., Jackson, G. & Muller, E. A. A generic equation of state for liquid crystalline phases of hard-oblate particles. *Molecular Physics* **110**, 1269-1288, doi:10.1080/00268976.2011.649794 (2012).

117 Liu, Y., Xu, Z., Gao, W., Cheng, Z. & Gao, C. Graphene and Other 2D Colloids: Liquid Crystals and Macroscopic Fibers. *Advanced Materials* **29**, 1606794-n/a, doi:10.1002/adma.201606794 (2017).

118 Chen, F. *et al.* Polydispersity reduction of colloidal plates via size fractionation of the isotropic-nematic phase transition. *Soft Matter* **13**, 3789-3793, doi:10.1039/C7SM00476A (2017).